Interior dynamics of tidally locked super-Earths

Inauguraldissertation
der Philosophisch-naturwissenschaftlichen Fakultät
der Universität Bern

vorgelegt von

Tobias Gabriel, Meier

von Luzern LU

Leiterin / Leiter / LeiterInnen der Arbeit:
Dr. Dan J. Bower
Prof. Dr. Kevin Heng
Center for Space and Habitability
Universität Bern

Interior dynamics of tidally locked super-Earths

Inauguraldissertation
der Philosophisch-naturwissenschaftlichen Fakultät
der Universität Bern

vorgelegt von

Tobias Gabriel, Meier

von Luzern LU

Leiterin/Leiter/LeiterInnen der Arbeit:
Dr. Dan J. Bower
Prof. Dr. Kevin Heng
Center for Space and Habitability
Universität Bern

Von der Philosophisch-naturwissenschaftlichen Fakultät angenommen.

Bern, 9. September 2022

Der Dekan/Die Dekanin
Prof. Dr. Marco Herwegh

Abstract

Within the last few years, a large number of rocky exoplanets with masses larger than Earth have been detected. These so-called super-Earths do not exist in our Solar System and their tectonic regimes could be substantially different than Earth's. Current and near-future astronomical observations are capable of measuring the masses, radii and sometimes even the surface temperature of these planets with unprecedented precision, and we can now use these measurements to probe their interior dynamics. To achieve this, we run geodynamic simulations of the interior mantle flow using the mantle convection code StagYY in the two-dimensional spherical annulus geometry. We constrain the longitudinal surface temperature dependence using the results from thermal phase curve observations and general circulation models. Many super-Earths are on very short orbits and are therefore most likely tidally locked. This means that the same hemisphere always faces the host star, which can lead to a strong temperature contrast between the dayside and nightside.

In Chapter 1, I present our results on the interior dynamics of super-Earth LHS 3844b. The thermal phase curve of this planet suggests that this planet lacks a substantial atmosphere. The dayside temperature is around 1040 K and the nightside temperature is consistent with zero K. Our numerical simulations suggest that this planet could exhibit hemispheric tectonics if it has a strong lithosphere. In such a regime, a cold and viscous downwelling is located predominantly on one hemisphere and hot upwellings are getting flushed around the core-mantle-boundary (CMB) towards the other hemisphere, where they rise towards the surface. Such a regime is currently absent in our Solar System and this work is the first observationally constrained indication that such a regime could operate on exoplanets.

In Chapter 2, we investigate the case of super-Earth GJ 486b that is very similar to LHS 3844b in terms of size. For this planet, it is not (yet) known whether it was

able to retain its atmosphere. However, it is a suitable target for future follow-up observations that aim to characterise its atmosphere and we therefore investigate in this study what tectonic regimes could operate on this planet for different surface temperature contrasts that are derived from different types of atmospheres. This study provided also an opportunity to investigate further what causes hemispheric tectonics and if it could operate on planets with smaller temperature contrasts between dayside and nightside. As with LHS 3844b, we find that hemispheric tectonics is favoured for planets with strong lithospheres. However, a strong temperature contrast between dayside and nightside and overall higher (dayside) surface temperatures are needed in order for the downwelling to be pinned to one hemisphere.

In Chapter 3, we study the case of lava world 55 Cancri e. This is the first rocky exoplanet for which a thermal phase has been observed. This planet's dayside temperature is around 2700 K and the nightside is roughly 1380 K. Therefore, the dayside most likely harbours a magma ocean which could potentially even extend towards the nightside. In this study, we investigate the impact of such a global magma ocean on the interior mantle dynamics. We parametrise heat transport inside the magma ocean through a very high eddy diffusivity. We find that if both hemispheres are molten, the magma ocean will tend to equilibrate the temperatures at the interface between the magma ocean and the underlying solid mantle and dichotomous mantle convection is therefore less likely. If only the dayside is molten, we find that a massive plume forms on the dayside of the planet which rises from the CMB towards the magma ocean.

In conclusion, we find that rocky super-Earths that are on very short orbits around their host star could exhibit tectonic regimes that are unlike anything we currently observe in our Solar System. A planet's tectonic regime is inherently related to its atmosphere through long-term cycling of volatiles through outgassing. Our work has therefore important consequences for current and upcoming space missions, such as CHEOPS, JWST, ARIEL or PLATO that will target super-Earths and aim to characterise their atmospheres and surface composition. A spatially-variable release of volatiles might for example lead to secondary features in thermal phase curve observations.

What we know is a drop, what we don't know a (magma) ocean

Isaac Newton (adapted)

I would like to dedicate this thesis to my parents, Yvonne and Hansjörg, my brother Felix, and my sister Regula.

Contents

List of Figures

List of Tables

Chapter 1

Introduction

Ever since people started to gaze up at the night sky, they have wondered whether we are alone in the Universe or if there are other worlds like ours. More than 2000 years ago, the Greek astronomer and mathematician Aristarchus of Samos put forward the *heliocentric hypothesis*, where the Sun is in the centre and Earth revolves around it (Heath and Aristarchus, 1913). His work was however lost and it was not until the 16$^{\text{th}}$ century when Nicolaus Copernicus published his work *De revolutionibus orbium coelestium* which offered an alternative view to the then predominant geocentric model (Copernicus, 1543). This was also the start of the *Copernican Revolution*, during which Johannes Kepler advanced the heliocentric theory by postulating that planets revolve around the Sun on elliptical trajectories (rather than circular) (Kepler, 1609) and Galileo Galilei discovered Jupiter's four largest moons with a newly invented telescope (Galilei, 1610). The Copernican Revolution ended with Isaac Newton's law of universal gravitation published in *Philosophiae Naturalis Principia Mathematica*, that explained the elliptic orbits of the planets (Newton, 1687).

Moving forward to 1995, the first planet outside of our Solar System (a so-called exoplanet) revolving around a Sun-like star was discovered (Mayor and Queloz, 1995), and the hunt for a habitable Earth-twin officially began. In the Solar System, Earth is the only planet that is inhabited, and it is also the only planet that exhibits plate tectonics. Plate tectonics is the theory that Earth's outer rigid shell (the lithosphere) is broken into several plates that move with respect to each other (e.g., Morgan, 1968). Abraham Ortelius was the first to propose that Earth's continents

had once been connected before they started to drift away from each other (Ortelius, 1596). Much later, Alfred Wegener, known as the father of the *continental drift theory*, proposed that all continents were once part of a supercontinent called *Pangea*, which then broke up into several continents that subsequently drifted away from each other (Wegener, 1915). It was not until the late 1960s, however, that the theory of plate tectonics was developed (e.g., Schubert et al., 2001). The main force that drives the motion between the plates is believed to be gravitational pull from plates that sink into the mantle (slab pull) (Forsyth and Uyeda, 1975). The plates therefore form Earth's upper thermal boundary layer and mantle convection inside Earth is believed to be driven by cold descending slabs (e.g., Conrad and Lithgow-Bertelloni, 2002; McKenzie, 1969).

Plate tectonics is believed to play a crucial role in a planet's habitability, as it provides a mechanism to bury and recycle atmospheric greenhouse gases, thereby stabilising a planet's climate (e.g., Walker et al., 1981; Seager, 2013). A planet's atmosphere can also be protected through a magnetic field, which is generated by convective motions in Earth's outer liquid core (Buffett, 2000). This geodynamo is powered by cooling of the core, which in turn is governed by the energy that can be carried away through solid mantle convection (Jellinek and Jackson, 2015). It is, however, still an open question if a magnetic field actually provides protection against atmospheric escape (e.g., Gunell, Herbert et al., 2018; Ramstad and Barabash, 2021). Ultimately, all these different processes (climate, mantle convection, magnetic field) are therefore inherently linked with each other (Foley and Driscoll, 2016), and it is therefore vital to understand these processes in order to understand habitability of distant worlds. In this thesis, we focus on understanding the possible tectonic regimes that rocky exoplanets could exhibit. Some of these planets have no equivalent in our Solar System, and we will show that their tectonic regimes could be substantially different than Earth's.

1.1 (Exo)planets

The Solar System hosts 8 planets. Compositionally, they can be classified into 3 (or 4) different categories (Perryman, 2018):

- **Terrestrial**: The terrestrial planets are Mercury, Venus, Earth and Mars. They all have solid surfaces and are characterised by a silicate mantle and an iron core. During planet formation, the interior of these planets accumulated a large amount of heat which led to melting and chemical differentiation (e.g., Elkins-Tanton, 2012).

- **Gas giants**: Jupiter and Saturn are so-called gas giants and they are the two largest planets in the Solar System. They are dominated by hydrogen and helium and their elemental composition is close to that of the Sun.

- **Ice giants**: These are planets that consist mainly of elements heavier than hydrogen and helium. Thus, Uranus and Neptune are ice giants. Approximately $10 - 20\%$ of their mass is hydrogen and helium, while the biggest fraction is ices. In planetary science, volatiles with a melting point between 100–300 K such as H_2O, CH_4, CO, CO_2, are usually called ices.

This list can get expanded if one also considers dwarf planets:

- **Rocky and icy bodies**: These bodies consist mostly of rock and ice, such as the dwarf planet Pluto. Their masses are usually quite low and they have not accreted a substantial hydrogen/helium envelope. One can also place the **icy moons** inside this category. These are satellites that have an icy surface with a silicate interior and some (e.g., Europa) could potentially harbour a liquid ocean underneath the icy crust (Carr et al., 1998). Examples of icy moons are Jupiter's satellites Europa and Ganymede or Saturn's satellites Enceladus and Titan.

Planets that are outside of our Solar System are called exoplanets. More than 5100 exoplanets have been detected since the first detection of an exoplanet around a Sun-like star in 1995 (Mayor and Queloz, 1995). This exoplanet was detected through the *radial velocity method*. When a star is orbited by a planet, the star will move around the common barycenter as a result of the planet's gravitational attraction. This motion can be measured through precise Doppler measurements, and will provide information about the planet's period, distance from the star, eccentricity as well as its mass (Wright and Gaudi, 2012). Another very successful detection method is

transit photometry. If a planet passes in front of its parent star, the flux received from the star will decrease. Since this decrease in flux depends on the relative size between the planet and the star, transit observations can be used to determine an exoplanet's radius (Wright and Gaudi, 2012). The first planet that was detected through this method was HD 209458 (Charbonneau et al., 2000). *Direct imaging* of an exoplanet is possible if the planet has a large radius and a wide orbit around its host star. In this case, light from the host star that is reflected by the exoplanet can be directly observed (e.g., Currie et al., 2022). The first detection of an exoplanet through direct imaging was reported in 2005 (Chauvin et al., 2005). Exoplanets on wide orbits can potentially also be detected through the *microlensing technique* (Alcock et al., 1997). In this case, a foreground star (the 'lens') will magnify the light of the background star producing a so-called *Einstein ring* (Einstein, 1936). If the lens star is orbited by an exoplanet, the Einstein ring can be perturbed and enhanced because the planet acts as an additional lens (e.g., Bond, 2012). Since two stars have to align perfectly, this is a very challenging and unpredictable method to detect exoplanets, and follow-up observations are in most cases not possible.

Figure 1.1 shows an overview of detected exoplanets and with which observational technique they have been detected. On this figure, one can see that there is a large number of exoplanets, which have no equivalent in our Solar System: There are so-called *super-Earths* with masses between 1 and 10 Earth masses and some of them are on very short period orbits around their host star. Planets that have orbital periods of less than a day are called *ultra-short period planets (USPs)* (e.g., Winn et al., 2018). There are also (gas) giant planets with masses similar or bigger than Jupiter's on very short orbits. These are called *(ultra-)hot Jupiters*. Because of their large mass and short orbits, these exoplanets are the easiest to detect through the radial velocity and transit method. In fact, the first detection of an exoplanet around a Sun-like star was the hot Jupiter 51 Peg b (Mayor and Queloz, 1995). It was also a hot Jupiter, for which the first extrasolar atmosphere was detected (Charbonneau et al., 2002) as well as the first detection of thermal emission (Charbonneau et al., 2005). The occurrence rate of hot Jupiters is, however, relatively low (e.g., Howard et al., 2012; Wang et al., 2015). On the other hand, super-Earths (and Earth-like planets) are more difficult to detect, but studies

indicate that these are more prevalent than hot Jupiters (Fressin et al., 2013; Zhu et al., 2018; Mulders et al., 2018), and indeed over 1500 super-Earths have already been detected. In 2012, the first thermal emission from a rocky super-Earth was detected (Demory et al., 2012). A few years later, the first thermal phase curve of a super-Earth was observed, enabling the determination of a planet's longitudinal temperature dependence (Demory et al., 2016a) (see also Section 1.1.4 on thermal phase curves).

Some rocky super-Earths might even reside within the habitable zone (e.g., Pepe et al., 2011). The habitable zone is defined as the distance from a star, at which liquid water could exist on a planet's surface (Kasting et al., 1993). In this classical definition, the inner edge is defined by the loss of water through photolysis and hydrogen escape, while the outer edge is defined depending on the amount of greenhouse gases such as CO_2 or H_2O in the atmosphere that would heat a planet's surface through the greenhouse effect (Forget and Pierrehumbert, 1997). A planet's atmosphere is inherently influenced by its tectonic regimes and outgassing from the interior (e.g., Dehant et al., 2019). If we want to understand habitability of distant worlds, it is therefore crucial to study what interior tectonic regimes these planets could exhibit.

1.1.1 Tectonic Regimes

The lithosphere is the outer, rigid shell of a terrestrial planet or body. In a *stagnant lid* regime, the lithosphere is one single, immobile plate. Mercury, Mars and the Moon are expected to be in a stagnant lid regime. On the other hand, a *mobile lid* tectonic regime is characterised by a mobile lithosphere (as for example on Earth). In-between the stagnant and mobile lid, are the so-called *sluggish lid*, *episodic lid*, and *ridge-only* regimes. In a *sluggish lid* regime, the lithosphere is mobile, but has a lower speed than the underlying mantle (Lenardic, 2018). In an *episodic regime*, the planet has a stagnant lid with episodes of mobile lid tectonics where the lithosphere gets recycled (overturns). Venus is believed to be in an episodic lid regime (Turcotte, 1993). In a *ridge-only* regime, stable ridges form on the lithosphere without the formation of subduction zones. Such a regime could operate on planets with low Rayleigh numbers that lack internal heating sources (e.g., icy satellites) (Rozel et al.,

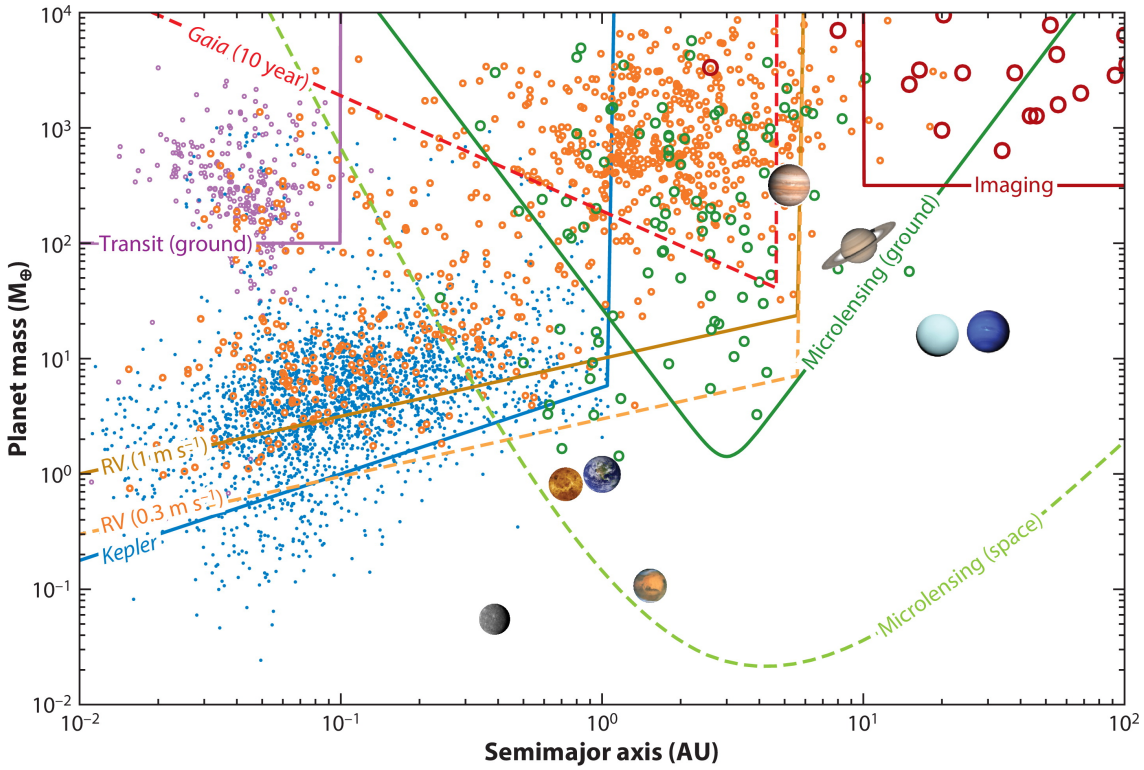

Zhu W, Dong S. 2021
Annu. Rev. Astron. Astrophys. 59:291–336

Figure 1.1 | From Zhu and Dong (2021): Mass versus semi-major axis of known planets, based on the "Confirmed Planets" list from the NASA Exoplanet Archive. The coloured lines show different sensitivity curves of missions and detection methods.

2015).

Earth is the only known planet that exhibits *plate tectonics*. Plate tectonics is a kinematic description where the lithosphere is divided into several plates that move with respect to each other (Morgan, 1968; Schubert et al., 2001, e.g.,). On Earth, the plates move at approximately 5–10 cm/year (e.g., Read and Watson, 1962). Plates move apart from each other at divergent boundaries (so-called mid-ocean ridges). This is also where new plate material (oceanic crust) is formed; while the plates spread, mantle material from the underlying asthenosphere will rise and produce melt through adiabatic decompression melting (e.g., Bottinga and Allegre, 1973). When the melt cools down, crustal material is produced (so-called mid-ocean ridge basalt, MORB). The oceanic lithosphere that moves away from the mid-ocean ridge will cool down and become denser and will then eventually sink into Earth's interior. This process is called subduction. Cold (and dense) mantle material that sinks into the mantle is also called downwelling. On the other hand, material that

rises is called upwelling. Upwelling beneath mid-ocean ridges is passive upwelling, because the mantle material is rising as a response of the diverging plate motion (Lachenbruch, 1976). These usually also have a shallow origin. On the other hand, active upwelling is associated with deep mantle plumes that rise from the core mantle boundary. They form because of instabilities of the lower thermal boundary layer at the CMB and are believed to cause hotspot regions with increased volcanic activity, such as Hawaii (e.g., Morgan, 1971; DePaolo Donald and Michael, 2003).

Last but not least, *degree-1 convection* is a tectonic regime where one hemisphere is dominated by a downwelling, while the other hemisphere is dominated by an upwelling (e.g., Roberts and Zhong, 2006). Such a regime could have operated on Mars (e.g., Zhong and Zuber, 2001; Keller and Tackley, 2009), the Moon (e.g., Zhong et al., 2000), and possibly Earth (Zhong et al., 2007; McNamara and Zhong, 2005).

1.1.2 Solar System rocky planets and moons

Our Solar System is the host of 6 terrestrial objects (composed of silicate rocks and metal): Mercury, Venus, Earth and Mars, the Moon and Jupiter's moon Io. Earth is the only planet where plate tectonics operates, and it is also the only known planet that is inhabited. Venus is very similar to Earth in terms of size and mass ($R \approx 0.95\,\mathrm{R}_\oplus$, $M \approx 0.815\,\mathrm{M}_\oplus$), but it has a very thick atmosphere (around 9.5 MPa) that mostly consists of CO_2, which causes a runaway greenhouse effect leading to surface temperatures around 737 K (Rasool and De Bergh, 1970), which is the hottest surface temperature of any planet in the Solar System. It is still an ongoing question, as to why Venus has been pushed into a runaway greenhouse regime. Plate tectonics is believed to play a crucial role in understanding the habitability of planets as it facilitates the long-term volatile cycling between the interior and the atmosphere and thus helps regulating the planet's climate. Venus lacks plate tectonics (although there is evidence that Venus' lithosphere shows limited, but widespread mobility (Byrne et al., 2021)), and has therefore no efficient mechanism to recycle carbon through a long term carbon cycle, as it operates on Earth (Walker et al., 1981). Some studies suggest that Venus could have harboured surface oceans with habitable conditions billions of years ago and that it was pushed then into the runaway greenhouse state because of its closer proximity to the Sun (e.g., Way et al.,

2016; Way and Del Genio, 2020; Kasting, 1988). Other studies suggest, however, that Venus' current atmosphere has a primordial origin, since it is unlikely that the current thick CO_2 atmosphere originates from volcanic outgassing alone (Head et al., 2021; Gillmann et al., 2022). In order to understand the habitability of (exo)planets, the coupling between climate, mantle and core needs to be taken into account (e.g., Foley and Driscoll, 2016): The climate influences the temperature on the surface of a planet, which in turn influences the likelihood of plate tectonics (Lenardic et al., 2008). The tectonic regime affects the climate through long-term volatile cycles and also controls the core cooling rate, which will influence whether a magnetic field can be sustained. The magnetic field is important for the long-term stability of the climate as it protects the planet's atmosphere from erosion through solar wind and other harmful cosmic rays from space (e.g., Seager, 2013), although it is still debated whether a magnetic field is in fact providing protection against atmospheric escape (e.g., Gunell, Herbert et al., 2018; Ramstad and Barabash, 2021).

Mars does currently not have active plate tectonics. It is in a stagnant-lid regime, where the lithosphere consists of a single rigid plate. Throughout its lifetime, Mars has been geologically and tectonically active (Golombek and Phillips, 2009). Most noticeably is probably the martian dichotomy, which refers to a crustal difference in elevation between the northern and southern crustal thickness. Earlier studies have focussed on explaining the martian dichotomy either as a consequence of degree-1 mantle convection in Mars' early history (e.g., Keller and Tackley, 2009) or through a giant impact (e.g., Marinova et al., 2008). More recent studies try to combine both, simulating a giant impact and its influence on the convection pattern inside Mars' mantle (Golabek et al., 2011, 2018).

Mercury, the Solar System's innermost planet, is the smallest terrestrial planet, but also has the highest bulk density. This is an indication that Mercury must have an unusually large iron core compared to the other terrestrial planets (Urey, 1951). This could have been caused by a giant impact that stripped away most of Mercury's silicate mantle (e.g., Benz et al., 1988; Wetherill, 1988). Mercury has probably been volcanically active early in its history (Byrne et al., 2018), and even though it was long believed that it is tectonically inactive, studies have shown that the planet's crust has been experiencing significant radial contraction driven by interior cooling

(Byrne et al., 2014; Watters et al., 2016). The amount of contraction is still debated. Most recent studies suggest however that it is less than previously thought (no more than 1-2 km since the late heavy bombardment) (Watters, 2021).

Jupiter's satellite Io stands out for its exceptionally high volcanic activity (e.g., Carr et al., 1979). Its surface heat flux of about 2500 $\mathrm{mWm^{-2}}$ is around 35 times larger than Earth's surface heat flux (Schubert et al., 2001). Io's largest source of internal heat is tidal dissipation (e.g., Peale et al., 1979). Tidal dissipation is an important source of internal heat for bodies which are on close-in orbits with high eccentricities. Over time, tidal dissipation will circularise the orbit (tidal circularisation) (e.g., Peale et al., 1979; Zahn, 2008). Io's eccentricity, however, is not decreasing because Io is in an orbital resonance with the Galilean moons Europa and Ganymede.

The Moon's orbit on the other hand is only slightly eccentric and the lunar heat flux (based on Apollo 15 and 17 measurements) is around 18 $\mathrm{mWm^{-2}}$ (Langseth et al., 1976). Because of its small size, the moon has cooled quickly and lost most of its internal heat. The most widely accepted theory of how the moon formed is through a giant impact between the Earth and a Mars-sized object (Canup and Asphaug, 2001). As a consequence of this impact, the moon would have become partially or completely molten (Stevenson, 1987). During solidification and differentiation, radiogenic heat sources are partitioned into the melt, which will then solidify and form the crust (Toksőz and Solomon, 1973). Therefore, most heat-producing elements are now near the surface and the underlying mantle is depleted, which makes mantle convection inside the Moon's mantle less likely (Schubert et al., 2001).

1.1.3 Rocky super-Earths

With the discovery of more and more rocky exoplanets, our attention is now drawn to whether some of these planets might be habitable or not and we therefore need to study what tectonic regimes these planets might exhibit. As shown in Section 1.1, many discovered rocky exoplanets are in the category of so-called super-Earths with masses larger than Earth's. Because of the extended pressure-ranges the tectonic regimes of such super-Earths might be unlike anything we know from our Solar System. With the help of state of the art geodynamic simulations we can now

investigate the effects of these extended pressure ranges and study the planform of tectonic regimes that could operate on super-Earths.

In fact, it is still an open question whether plate-tectonics on these planets is more-likely (e.g., Valencia et al., 2007a; van Heck and Tackley, 2011) or less likely (e.g., O'Neill et al., 2007). Valencia et al. (2007b) used scaling relations to determine the convective stresses that are needed to overcome the lithospheric plate resistance whereas van Heck and Tackley (2011) and O'Neill and Lenardic (2007) ran 2D convection models. An important property that is often neglected is the pressure-dependence of viscosity and/or thermodynamic properties. Stamenković et al. (2012) have found that the pressure dependence of viscosity can lead to sluggish convection which would reduce the likelihood of plate tectonics. Earth's upper part of the lower mantle is likely dominated by bridgmanite. Bridgmanite undergoes a phase-transition to post-perovskite at around 125 GPa which could dominate the lower mantle of super-Earths (Murakami et al., 2004). High-pressure, high-temperature experiments (e.g., Murakami et al., 2004; Fei et al., 2021) and first principle simulations (e.g., Umemoto et al., 2006; Ammann et al., 2009) can be used to reveal the thermodynamic properties and rheologies of minerals under pressures and temperatures that exist inside super-Earths. Tackley et al. (2013) have investigated the effect of post-perovskite rheology by running 2D convection models of different-sized super-Earths that are exclusively internally heated and by inducing plate-like behaviour of the lithosphere using plastic yielding. They found that plate-like tectonic behaviour is likely for Earth-like temperatures. They varied the masses of the planets up to 10 Earth masses and found that mobile-lid behaviour occurs for all of these, with convective regimes that are characterised by large upwellings and small, time-dependent downwellings. For smaller mass planets, the plastic yield stress had to be reduced, however, in order to obtain a mobile lid.

Many super-Earths are also on very short period orbits. So-called ultra-short period planets (USPs) are planets that have orbital periods of less than a day. Such short orbital periods also makes them likely to be tidally locked with a permanent dayside and nightside. The time scale for a planet/satellite to become tidally locked

can be estimated from the following equation (Peale, 1977; Gladman et al., 1996):

$$\tau_{despin} = \frac{wa^6CQ}{3Gm_pk_2R_p^5} \tag{1.1}$$

Where w is the spin rate, a the semi-major axis, C the moment of inertia about the spin axis, Q the specific dissipation function, m_p the planet mass, k_2 the tidal Love number, R_p the planet radius, and G the gravitational constant. Since the despin rate goes as $\tau_{despin} \propto a^6$, we therefore assume here that ultra-short period planets or short-period planets (orbital periods on the order of days) are tidally locked.

Several mechanisms have been proposed on how these ultra-short period planets formed (e.g., Zhou et al., 2005; Gaidos et al., 2007; Raymond et al., 2008) and this discussion is still ongoing. They could for example have formed *in situ*, by accretion of material that has been 'shepherded' inward by a migrating giant planet, or by photo-evaporation of a gaseous planet that migrated inwards from beyond the iceline (Raymond et al., 2008; Winn et al., 2018). Mass-loss through photo-evaporation could also be an explanation for the *small planet radius gap* (also called *Fulton gap*), which is a gap within the populations of close-in planets with radii $R_p < 1.5R_\oplus$ and planets with radii of $R_p = 2 - 3R_\oplus$ (Fulton et al., 2017). Owen and Wu (2017) showed that the evaporation timescale peaks for planets that have a H/He envelope that doubles the core size (iron core and rocky mantle) size. Below that, photo-evaporation dominates which can result in complete stripping of the envelope (leading to planets with $R_p < 1.5R_\oplus$). Planets that have accreted a larger H/He envelope will be able to retain a fraction of that envelope. Such an envelope will result in an increase of the planet's radius that is double the size of the core (Owen and Wu, 2017). If the planet is completely stripped of its atmosphere, this could lead to a bare rock planet with a strong surface temperature contrast between its dayside and nightside. An example of such a super-Earth is super-Earth LHS 3844b (Kreidberg et al., 2019).

Van Summeren et al. (2011) studied the effects of a dichotomous surface temperature on the pattern of convection, the tectonic regime and the rate and distribution of partial melting using incompressible, infinite-Prandtl number models of mantle flow. They have included plastic yielding with a temperature dependent Arrhenius-type viscosity law. They found a hemispheric dichotomy with plate-like tectonics

on the nightside and a continuously evolving mobile lid on the day side. Gelman et al. (2011) have found a similar degree-1 convection pattern for planets that receive intense solar insolation on the dayside. In Chapter 2 and Chapter 3, we will investigate the effects of a strong surface temperature dichotomy on the tectonic regimes of super-Earths LHS 3844b and GJ 486b. For LHS 3844b, the surface temperature contrast between the dayside and nightside has been determined with thermal phase curve observations (Kreidberg et al., 2019)

1.1.4 Thermal phase curves

Tidally locked planets can have strong contrasts in surface temperature between the dayside and nightside (e.g., Showman and Guillot, 2002). Thermal phase curve observations of a planet can be used to determine its longitudinal temperature dependence. A thermal phase curve is a map of the infrared time-dependent change in the brightness of a planet (Parmentier and Crossfield, 2018). The planetary phase curve $F_p/F_\star(\alpha)$ is given by (e.g., Demory et al., 2013):

$$\frac{F_p}{F_\star}(\alpha) = \frac{\langle I_p \rangle(\alpha)}{\langle I_\star \rangle} \left(\frac{R_p}{R_\star} \right)^2 \tag{1.2}$$

Where F_p and $F_\star$ are the planet and star flux respectively, α is the orbital phase, $\langle I_p \rangle$ the hemispherically averaged planet brightness, $\langle I_\star \rangle$ the hemispherically averaged star brightness, and R_p and $R_\star$ are the planet and star radii respectively. From the secondary eclipse depth (when the planet passes behind the star), one can infer the brightness of the planetary dayside. The offset between the eclipse depth and the maximum planetary curve is called the phase curve offset. The phase curve offset corresponds to the longitude of the brightest hemisphere. Such an offset could, for example, be caused by atmospheric circulation where heat gets advected away from the substellar point (Showman and Guillot, 2002; Cho et al., 2003).

The phase curve relative amplitude between the maximum and minimum phase curve can be used to infer the brightness contrast between the brightest and dimmest hemisphere (Parmentier and Crossfield, 2018). The thermal phase curve can then be converted into a brightness temperature map of the planet. Currently, the thermal phase curves of three rocky super-Earths have been observed, namely those of 55

Cancri e (Demory et al., 2016a), LHS 3844b (Kreidberg et al., 2019), and K2-141b (Zieba et al., 2022). The thermal phase curves of 55 Cancri e and K2-141b have revealed that the dayside temperature of these planets is sufficiently high that a global magma ocean can form. 55 Cancri e has a dayside temperature around $T_{\rm day}$ = 2700 K and K2-141b of around $T_{\rm day}$ = 2050 K. For comparison, Earth materials at surface pressures melt at around 1450 K.

1.1.5 Magma ocean worlds

If substantial parts of a planet become molten, a magma ocean forms. The heat required for melting can be delivered through several mechanisms:

- **Accretionary impacts**: During planet formation, a planet accretes planetesimals and planetary embryos and the kinetic energy from these giant impacts gets converted into thermal energy (e.g., Elkins-Tanton, 2012).
- **Radiogenic heating**: This is heat provided from the decay of short- and long-lived radioisotopes, such as ^{26}Al or ^{238}U.
- **Core formation**: During differentiation, the more dense material, like iron, sinks into the core. The gravitational potential from the sinking dense material gets converted into thermal energy through frictional heating (Birch, 1965).
- **Tidal heating**: Tidal heating occurs when tidal forces lead to the distortion of a planetary body's shape that causes frictional heating. This is especially important for planets and moons on short period orbits with large eccentricities (e.g., Tobie et al., 2005; Bolmont et al., 2020).
- **Induction heating**: This is heat produced through electromagnetic induction heating driven by a star's magnetic field. This effect could be significant for planets around fast-rotating M-type stars, as these can host magnetic fields of several hundred gauss (Kislyakova et al., 2017; Kislyakova and Noack, 2020; Noack et al., 2021).
- **Solar radiation**: This is heat that is provided from the host star as radiation (e.g., Léger et al., 2011; Gelman et al., 2011). Although this form of heating

can be neglected for Earth's mantle heat budget, it could be an important source of heat for close-in (and tidally locked) super-Earths, such as 55 Cancri e.

Magma oceans behave rheologically as a liquid and are vigorously convecting (Elkins-Tanton, 2012). The transition from a fluid-like behaviour to solid-like is called the *rheological transition* ϕ_c. If the melt fraction ϕ is larger than ϕ_c, the magma ocean behaves like fluid and has a viscosity on the order of 1 Pa s. If the melt fraction is lower than ϕ_c, the fluid starts to behave more like a solid and viscosity is many orders of magnitude higher (around 10^{21} Pa s). Theory combined with experimental calibration can be used to constrain the rheological transition, as well as to parametrise the viscosity dependence on the melt fraction (e.g., Caricchi et al., 2007; Costa et al., 2009).

If a significant portion of a planet is covered by a magma ocean, the planet is called a *Magma Ocean World* or *Lava World* (Chao et al., 2021). Most rocky planets in our Solar System are believed to have gone through a magma ocean stage (Schaefer and Elkins-Tanton, 2018; Elkins-Tanton, 2012), although this stage was short-lived since there was no mechanism to sustain large melt reservoirs after accretion and core formation. If the liquidus and solidus temperature profile is steeper than the adiabatic temperature gradient, crystallisation of the magma ocean will proceed from the bottom to the top (Abe, 1993; Elkins-Tanton, 2012). However, at high pressures the melt could become denser than the solids which can lead to the formation of a basal magma ocean (Labrosse et al., 2007). For Earth, such a basal magma ocean would have solidified after 2–3 Gyrs, whereas on Venus it could still be present because Venus' interior is cooling more slowly than Earth's (O'Rourke, 2020). The presence of a basal magma ocean has important consequences, as it suppresses the heat loss from the core and thereby the onset of a geodynamo (Labrosse et al., 2007). These magma oceans have mostly formed through accretionary and giant impacts, and through the energy provided from the decay of short-lived radioisotopes and core formation. The martian and terrestrial magma oceans are completely solidified within 5–10 Myrs (Elkins-Tanton, 2012). However, this timescale also depends on whether the planet has an atmosphere acting as a thermal blanket or if the magma completely exposed to space (Solomatov, 2000, 2007).

A magma ocean could potentially be sustained over much longer timescales if the planet is on a very short orbit around its host star and therefore experiences intense insolation or if it experiences significant tidal heating (e.g., Chao et al., 2021). In Chapter 4, we investigate how a sustained magma ocean on the surface of super-Earth 55 Cancri e influences the mantle dynamics of this planet. For this, we also use the results from general circulation models (GCMs), because the thermal phase curve observations determine the temperature of a potential atmosphere, which could be different from the temperature at the surface of the planet.

1.1.6 General Circulation Models

In order to model heat transport and circulation of planetary atmospheres, general circulation models (GCMs) are used. The first GCMs were developed to understand Earth's climate by combining atmospheric and oceanic processes (Phillips, 1956). The equations governing the circulation of an atmosphere are similar to the equations governing mantle convection. GCMs solve the fluid dynamics equations on a sphere using conservation of mass (continuity equation), momentum (Navier-Stokes equations) and energy (thermal energy equation) in order to study the circulation and climate of planetary atmospheres. The reason why a different numerical approach (i.e. different solvers) is needed comes from the fact that atmospheric circulation and solid mantle convection occur on different scales. The planetary mantle behaves like highly viscous fluid whereas atmospheric circulation can be treated as inviscid (Euler equations). Therefore, different versions of the Navier-Stokes equations are needed, which require different solvers. For atmospheric circulation models, the so-called *primitive equations* can be used (Friedlander and Serre, 2003). These are derived from the hydrostatic approximation, where gravity is balanced by the vertical component of the pressure gradient.

GCMs are now also used to solve for the climate and atmospheric circulation of exoplanets. These GCMs might not need the whole complexity that is necessary to study Earth's climate, but on the other hand have to include different processes that are relevant in exoplanet atmospheres. Such processes could, for example, be the treatment of shocks, radiative transfer, magnetic fields or the formation of clouds (Heng and Showman, 2015). GCMs have been used to study hot-Jupiters (Showman

and Guillot, 2002) or the atmospheric circulation of potential atmospheres of rocky (tidally-locked) super-Earths (e.g., Joshi et al., 1997; Pierrehumbert, 2010; Heng et al., 2011). GCMs can be used to relate a planet's thermal phase curve observation to its climate (Hammond and Pierrehumbert, 2017). In this thesis, we use the results from GCMs to constrain the surface temperature in our interior dynamic models.

1.2 Thesis structure

The goal of this thesis is to study the different tectonic regimes that could operate on tidally locked super-Earths. To achieve this, we constrain the dayside to nightside surface temperature contrast using observational data from thermal phase curve observations (Section 1.1.4). For the cases where the planet potentially has an atmosphere, we also use the results from general circulation models (Section 1.1.6).

To probe the interior dynamics of rocky super-Earths we use the mantle convection code StagYY with two-dimensional spherical annulus geometry. In section 1.3, I provide an outline of the theoretical and computational methods.

In Chapter 2, I discuss the case of super-Earth LHS 3844b, for which the thermal phase curve suggests that this super-Earth is most likely devoid of an atmosphere. For this planet, we find that hemispheric tectonics is a possible tectonic regime for tidally locked rocky super-Earths with a strong temperature contrast between the dayside and nightside.

In Chapter 3, I present the results for the interior dynamics of super-Earth GJ 486b. For this planet, it is not known whether it was able to retain an atmosphere. We therefore use the results from GCMs to infer the surface temperature contrasts assuming different types of atmospheres. In this chapter, we dive deeper into understanding what causes hemispheric tectonic regimes or degree-1 convection on tidally locked super-Earths.

In Chapter 4, I present the case of the lava world 55 Cancri e. This planet receives intense insolation from its host star and therefore most likely harbours a magma ocean on the dayside and potentially even on the nightside. In this chapter, I discuss the consequences of such a global magma ocean and how it affects the interior mantle dynamics.

Finally, in Chapter 5, I provide both summary and conclusions of this thesis, and present an outlook and directions of future research topics concerning the interior dynamics of rocky super-Earths.

1.3 Modelling mantle convection

1.3.1 Navier-Stokes Equations

On geological timescales, rocks inside the mantle of Earth and other rocky planets behave like a highly viscous fluid. We can therefore consider conservation of mass, momentum, and energy of a fluid continuum in order to solve how rocks flow inside the mantle of rocky planets. Mass conservation is given by:

$$\frac{\partial \rho}{\partial t} + \frac{\partial}{\partial x_i}(\rho u_i) = 0 \tag{1.3}$$

Where ρ is density, t is time, x is position and u is velocity. In order to determine the conservation of momentum for a fluid continuum, we can consider the force balance on an elemental parcel of fluid. This leads to the Navier-Stokes equations:

$$\rho \frac{Du_i}{Dt} = -\frac{\partial P}{\partial x_i} + \frac{\partial \tau_{ij}}{\partial x_j} + \rho g \tag{1.4}$$

Where P is pressure, g is gravitational acceleration, and p is the fluid pressure. $\frac{D}{Dt}$ is the material (or total) derivative and is given by

$$\frac{D}{Dt} = \frac{\partial}{\partial t} + u_i \frac{\partial}{\partial x_i} \tag{1.5}$$

τ_{ij} is the deviatoric stress tensor and is related to the strain rate tensor ϵ_{ij} by a stress-strain rate relation:

$$\tau_{ij} = 2\mu\epsilon_{ij} + \lambda\epsilon_{kk}\delta_{ij} \tag{1.6}$$

Where δ_{ij} is the Kronecker delta, μ is the dynamic viscosity, and λ is the second viscosity. The strain rate tensor ϵ_{ij} of a fluid is given by:

$$\epsilon_{ij} = \frac{1}{2}\left(\frac{\partial u_i}{\partial x_j} + \frac{\partial u_j}{\partial x_i}\right) \tag{1.7}$$

One can define a bulk viscosity $k_b = \lambda + \frac{2}{3}\mu$. Under the Stokes assumption, k_b is neglected. The left hand-side term of Eq. 1.4 ($\rho\frac{Du_i}{Dt}$) represents the inertial forces and can be neglected in highly viscous flows (infinite Prandtl number approximation). In the anelastic liquid approximation, one assumes a time-independent but pressure-dependent reference density profile for the mass and energy conservation (Jarvis and McKenzie, 1980). We can also linearise the equation of state, because density changes that arise from temperature and pressure variations are small compared to the average density of the mantle (after (Schubert et al., 2001)):

$$\rho = \bar{\rho}(\bar{T},\bar{P}) + \overline{\left(\frac{\partial\rho}{\partial P}\right)}_T p' + \overline{\left(\frac{\partial\rho}{\partial T}\right)}_p T' = \bar{\rho}(\bar{T},\bar{P}) + \bar{\rho}\bar{\chi}_T P' - \bar{\alpha}\bar{\rho}T' \tag{1.8}$$

Where T is temperature, α the thermal expansivity, and χ_T the isothermal compressibility. The over-bar refers to the reference state and the primes to the departure from it. The *truncated*, anelastic liquid approximation further assumes that variations of density due to pressure variations are small. This removes the $\bar{\rho}\bar{\chi}_T P'$ term on the RHS of Equation 1.9.

$$\rho = \bar{\rho}(\bar{T},\bar{P}) - \bar{\alpha}\bar{\rho}T' \tag{1.9}$$

We now determine the nondimensional version of the Navier-Stokes equation by scaling various variables by characteristic scales. Table 1.1 shows the characteristic scales used for the non-dimensionalisation. Non-dimensional variables are denoted by an asterisk. For example the non-dimensional density is $\rho^* = \rho/\rho_r$. The subscript 'r' denotes a reference value.

In terms of these non-dimensional variables, the anelastic, infinite Prandtl number Navier-Stokes equation (1.4) is given by:

$$0 = -\frac{\partial P'^*}{\partial x_i^*} + \overline{g}_i^*\overline{\rho}^*\overline{\chi}_T^* P'^* \frac{\mathcal{D}}{\gamma_r}\frac{c_{p_r}}{c_{v_r}} - \overline{g}_i^*\overline{\rho}^*\overline{\alpha}^* T'^* Ra + \frac{\partial}{\partial x_j^*}\left[\mu^*\left(\frac{\partial u_i^*}{\partial x_j^*} + \frac{\partial u_j^*}{\partial x_i^*}\right)\right] \tag{1.10}$$

Ra is the Rayleigh number given by:

$$\mathrm{Ra} = \frac{\rho_r g_r \alpha_r \Delta T_{sa} D^3}{\eta_r \kappa_r} \tag{1.11}$$

variable name	symbol (units)	characteristic scale
length	x_i (m)	D
density	ρ (kg/m^3)	ρ_r
temperature	T (K)	ΔT_{sa}
isothermal compressibility	χ_T (m s^2/kg)	χ_r
thermal expansivity	α (K^{-1})	α_{p_r}
specific heat capacity	c_p (J/(kg K))	c_{p_r}
thermal conductivity	k (W/(m K))	k_r
velocity	u (m/s)	$u_r = k_r/(\rho_r c_{p_r} D)$
viscosity	μ (Pa s)	μ_r

Table 1.1 | Characteristic scales used for non-dimensionalisation. The subscript 'r' denotes a reference value. ΔT_{sa} is the superadiabatic temperature gradient.

Where ΔT_{sa} is the super-adiabatic temperature gradient. The non-dimensional Rayleigh number Ra multiplies the buoyancy force associated to temperature variations in the momentum equation. It is therefore one of the principal dimensionless parameters as this controls the vigour of convection inside the mantle (Schubert et al., 2001) The equation for the conservation of energy is given by:

$$\rho c_p \frac{DT}{Dt} - \alpha T \frac{DP}{Dt} = \frac{\partial}{\partial x_i}\left(k \frac{\partial T}{\partial x_i}\right) + \Phi + \rho H \tag{1.12}$$

Where k is thermal conductivity and H is the rate of internal heat production per unit mass, c_p the specific heat capacity at constant pressure, and Φ is the dissipation function given by:

$$\Phi = \tau_{ij} \frac{\partial u_i}{\partial x_j} \tag{1.13}$$

Equation 1.12 is also called the advection-diffusion equation. In order to solve for the flow inside the mantle, the equations for conservation of mass (Eq. 1.3), momentum (Eq. 1.10), and energy (Eq. 1.12) need to be solved together. For this, we use the code StagYY (Tackley, 2008) to solve for the flow inside the mantle in the two-dimensional spherical annulus geometry (Hernlund and Tackley, 2008).

1.3.2 Numerical methods

StagYY solves for highly viscous flow using a finite difference/volume technique on a staggered grid. Pressure and temperatures are defined at the centre of cells and velocities are defined at the centres of faces perpendicular to the relevant velocity

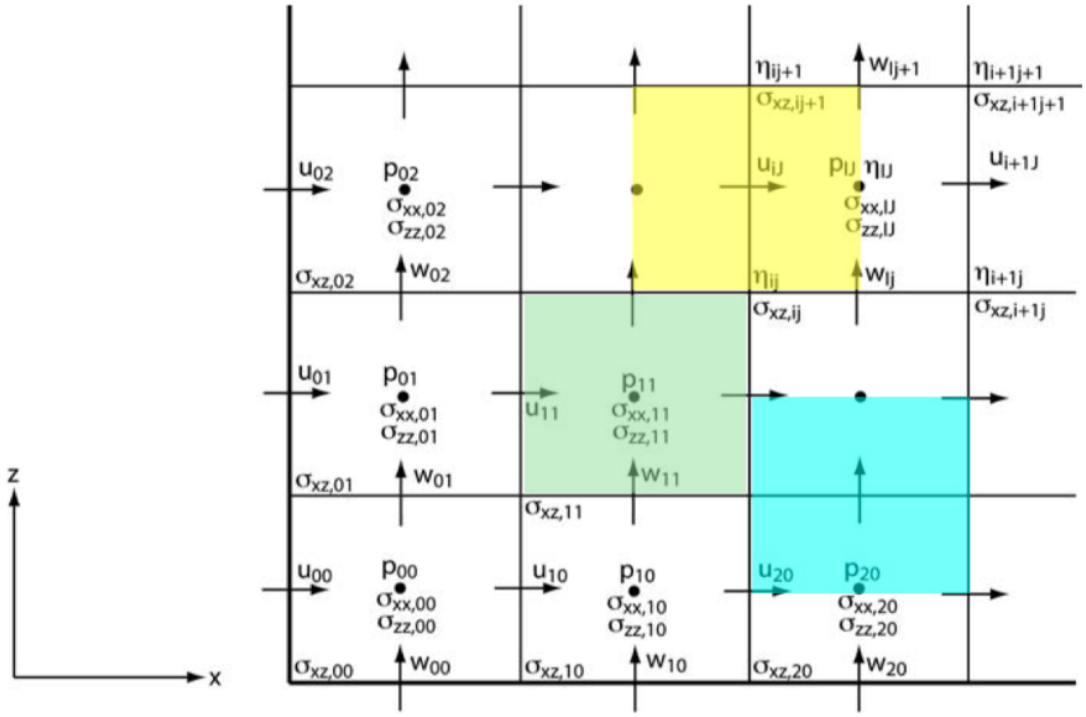

Figure 1.2 | Adapted from (Ismail-Zadeh and Tackley, 2010): Locations of pressure, velocity components, stresses, and viscosity components on a 2D staggered grid. In green is the control volume for the continuity equation. In yellow and blue are the control volumes for the y- and z-momentum equation respectively.

component. Such a staggered grid allows for greater accuracy and avoids the possibility of checkerboard oscillations (Ismail-Zadeh and Tackley, 2010). Figure 1.2 shows how pressure, velocity, stresses and viscosity are defined in a 2-dimensional staggered grid. At each time step, the flow solver determines the pressure and velocity field by solving the continuity and momentum equation. Then, a time step is taken using the advection-diffusion equation (energy equation). This two-step approach is possible because the continuity and momentum equations do not depend explicitly on time. In this work, we use a direct solver to solve the coupled set of linear equations arising from the discretisation of the momentum and continuity equation. For the energy equation, we use the *Total Variation Diminishing (TVD)* finite volume scheme for advection and an implicit diffusion solver for the diffusion part. Our models incorporate compressibility by employing the truncated, anelastic, infinite Prandtl number (TALA) approximation. We use the 2D *spherical annulus geometry* (Hernlund and Tackley, 2008) for all our models. In this geometry, the model domain is a 2D slice around the equator with a 'virtual' thickness that is

proportional to the radius. This ensures that the influences of curvature inside the mantle are taken into account.

1.3.3 Boundary conditions

In order to obtain numerical solutions, we need to define boundary conditions. For the mantle, these boundaries are the surface and the core-mantle-boundary (CMB), which are the interface between the mantle and the core. In order to reach closure of the system, we need to define both mechanical (e.g., velocity, stresses) and thermal boundary conditions (e.g., temperature, heat flux). For all our models, we set both the surface and the CMB to be free-slip (horizontal shear stress is zero). We also set the radial component of the velocity at the surface and CMB to be zero. This means, that there is no mass flow into or out of the domain. This condition can be formulated as (Ismail-Zadeh and Tackley, 2010):

$$u_i n_i = 0, \quad \frac{\partial u_{\tau i}}{\partial n_i} = 0. \tag{1.14}$$

Where u_τ is the projected velocity onto the tangential plane of the boundary and n is the normal to the tangential plane. Regarding the thermal boundary conditions, we use an isothermal boundary condition for the CMB (i.e. the temperature is fixed at the CMB), because a molten outer liquid core will rapidly equilibrate any temperature differences that arise at the CMB as a consequence of the comparatively slow convection of the mantle. For the surface, we use a constant tidally locked or radiative tidally locked boundary condition. In the constant tidally locked case, the surface temperature is constant in time but varies with latitude. This variation can be determined by assuming that at equilibrium, the power emitted by the planet at a given latitude θ is the same as absorbed:

$$\sigma T_s^4(\theta) dA = \frac{L_\odot}{4\pi d^2} d\Sigma \tag{1.15}$$

Where $\sigma = 5.670 \cdot 10^{-8}\,\mathrm{Wm^{-2}K^{-4}}$ is the Stefan-Boltzmann constant, $T_s(\theta)$ is the surface temperature of the planet at latitude θ, $L_\odot$ is the star's luminosity, d is the distance of the planet, dA is the emitting surface element ($\pi R_p^2 \cos\theta$ for a tidally locked planet), and $d\Sigma = \pi R_p^2 \cos^2\theta$ is the cross section of the planet that absorbs

the stellar flux. Therefore, the surface temperature variation for a tidally locked planet is given by:

$$T_s(\theta) = \begin{cases} T_{\text{night}} + (T_{\text{day}} - T_{\text{night}}) \cdot \cos(\theta)^{1/4}, & \text{if } -90^\circ \leqslant \theta < 90^\circ \\ T_{\text{night}}, & \text{if } 90^\circ \leqslant \theta < 270^\circ \end{cases} \tag{1.16}$$

Where T_{night} is the nightside temperature and T_{day} is the temperature at the sub-stellar point, which is located at $\theta = 0^\circ$.

In the radiative case, the temperature at the surface is determined using:

$$\sigma T_s^4 = F_{\text{top}} + \sigma T_{\text{rad}}^4 \tag{1.17}$$

Where F_{top} is the surface heat flux from the interior and T_s is the surface temperature. T_{rad} is defined as the temperature of the planet when it is in stellar equilibrium with the irradiation from the star.

1.3.4 Equations of state

For the reference state density profile, a 3$^{\text{rd}}$-order Birch-Murnaghan equation of state is used:

$$P(\rho) = \frac{3K_{a0}}{2}\left[\left(\frac{\rho}{\rho_0}\right)^{7/3} - \left(\frac{\rho}{\rho_0}\right)^{5/3}\right]\left\{1 + \frac{3}{4}(K'_{a0} - 4)\left[\left(\frac{\rho}{\rho_0}\right)^{2/3} - 1\right]\right\} \tag{1.18}$$

Where ρ_0 is the density at $P = 0$, K_{a0} is the adiabatic bulk modulus at $P = 0$ and $K'_{a0} = (\frac{\partial K}{\partial P})_a$ the pressure derivative of the adiabatic bulk modulus at $P = 0$. The thermal expansivity is determined by:

$$\alpha(P) = \frac{\rho(P)\Gamma(P)c_p}{K_a(P)} \tag{1.19}$$

Where $K_a(P)$ is the adiabatic bulk modulus, given by:

$$K_a(P) = \rho\left(\frac{\partial P}{\partial \rho}\right)_a \tag{1.20}$$

Hence, $K_a(P)$ can be determined using equations (3.2) and (1.20). $\Gamma(P)$ is the Grüneisen parameter, which is defined by:

$$\Gamma(P) = \frac{\alpha}{\rho c_p K_a} \tag{1.21}$$

$\Gamma(P)$ varies as:

$$\Gamma = \Gamma_0 \left(\frac{\rho_0}{\rho}\right) \tag{1.22}$$

The adiabatic compressibility is defined as the inverse of the adiabatic bulk modulus:

$$\chi_a \equiv \frac{1}{K_a} = \frac{1}{\rho}\left(\frac{\partial \rho}{\partial P}\right)_a \tag{1.23}$$

Using the hydrostatic equilibrium and Equation 1.21, one can write the density gradient as a function of depth z:

$$\frac{\partial \rho}{\partial z} = \frac{\rho \alpha g}{c_p \Gamma} \tag{1.24}$$

Equation 1.24 is then integrated to determine the reference density profile. For our models, we either use a 1-phase system consisting of olivine (ol) or a 3-phase system consisting of the olivine system (ol), the pyroxene-garnet system (px-gt) and a melt system. For the 3-phase system, solid material consists of 60% olivine, and 40% pyroxene-garnet. The melt fraction determines how much of the solid will be in the melt system. For the olivine system, we include 3 phase transitions (olivine-spinel, spinel-perovskite, and perovskite-post-perovskite) occurring at $410\, g/g_\oplus$ km, $660\, g/g_\oplus$ km, and $2740\, g/g_\oplus$ km respectively (where g is the planet's surface gravitational acceleration, with $g_\oplus = 9.81\,\mathrm{m/s^2}$ being Earth's surface gravitational acceleration). For the pyroxene-garnet system, we include 4 phase transitions (basalt-eclogite, pyroxene-garnet, garnet-perovskite, and perovskite-post-perovskite occurring at $40\, g/g_\oplus$ km, $410\, g/g_\oplus$ km, $720\, g/g_\oplus$ km, and $2740\, g/g_\oplus$ km. The melt phase does not have any phase transitions. Table 3.1 shows the parameters used for the reference density profiles. Table 1.3 shows the parameters used for the phase transitions, where $\Delta\rho$ is the density jump and γ the Clapeyron slope of the phase transition.

Figure 1.3 shows the reference state density for super-Earth 55 Cancri e. The

bulk density of an N-component mixture with individual densities ρ_i, and mass fractions X_i is determined using a volumetric average:

$$\rho = \left(\sum_{i=1}^{N} \frac{X_i}{\rho_i} \right)^{-1} \tag{1.25}$$

Similarly, the thermal expansivity of a mixture is determined using:

$$\alpha = \rho \sum_{i=1}^{N} \frac{X_i}{\rho_i} \alpha_i \tag{1.26}$$

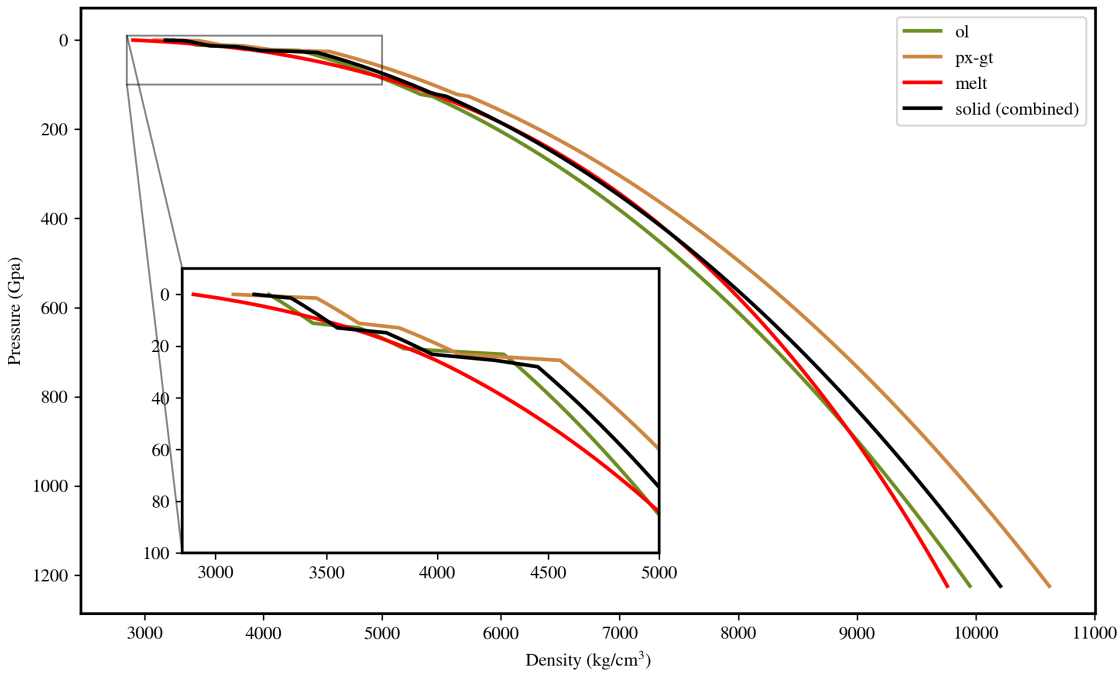

Figure 1.3 | Reference state density for super-Earth 55 Cancri e including the olivine, pyroxene-garnet and melt system.

Mineralogy	K_0 (GPa)	K'	ρ_s (kg/m^3)	Γ_0
upper mantle (olivine)	163	4.0	3240	1.3
upper mantle (pyroxene)	163	4.0	3080	1.3
transition zone	85	4.0	3226	0.85
bridgmanite	210	3.9	3870	1.3
post-perovskite	210	3.9	3906	1.3
melt	30	6.0	2750	0.6

Table 1.2 | Birch-Murnaghan parameters for reference density profiles.

Depth (km)	Temperature (K)	$\Delta\rho$ (kg/m^3)	γ (MPa/K)
Olivine-spinel-bridgmanite-postperovskite			
410	1600	180	2.5
660	1900	400	−2.5
2740	2300	61.6	10.0
Pyroxene-garnet-bridgmanite-postperovskite			
60	1000	350	1.5
410	1600	150	1.0
710	1900	400	1.0
2740	2300	61.6	10.0

Table 1.3 | Parameters used for the phase transitions.

.

1.3.5 Rheology

We use an Arrhenius law to model diffusion creep in the mantle:

$$\eta(T,z) = \eta_0 \exp\left(\frac{E_a + PV_a(P)}{RT} - \frac{E_a}{RT_0}\right) \tag{1.27}$$

Where η_0 is a reference viscosity, E_a is the activation energy, $V_a(P)$ the activation volume and $R = 8.31445\,\mathrm{JK^{-1}mol^{-1}}$ the universal gas constant, and T_0 is the temperature at $P = 0$. The activation volume depends on pressure following the law:

$$V(P) = V_0 \exp\left(-\frac{P}{P_{decay}}\right) \tag{1.28}$$

Where P_{decay} is the decay pressure controlling the pressure dependence. For our models, we use use the parameters from Tackley et al. (2013) for the viscosity of the upper mantle, bridgmanite and post-perovskite. These parameters are given in Table 3.2.

Mineralogy	E_0 (kJ/mol)	V_0 (cm^3/mol)	p_{decay} (GPa)	η_0 (Pa s)
Upper mantle	300	5.0	∞	10^{21}
Bridgmanite	370	3.65	200	$3.0 \cdot 10^{23}$
Post-perovskite lower bound	162	1.4	1610	$1.9 \cdot 10^{21}$
Post-perovskite upper bound	780	5.0	1100	$1.05 \cdot 10^{34}$

Table 1.4 | From (Tackley et al., 2013): Parameters used for the Arrhenius-like viscosity law (Eqs. (1.27) and (3.4))

.

The outermost, rigid layer of a planet (lithosphere) is prone to failure if differential stresses are sufficiently large. We model this through a plastic yielding criteria.

At low pressure, the strength of the lithosphere is related to its fracture strength or frictional sliding of faults (Byerlee's law (Byerlee, 1978)). At higher pressure, the strength is related to ductile failure caused by dislocation motion of the lattice (Kohlstedt et al., 1995). Both, the brittle and ductile components are encapsulated within a pressure-dependent yield stress σ_y:

$$\sigma_{\mathrm{y}} = \min(c_f P, \sigma_{\mathrm{duct}} + \sigma'_{\mathrm{duct}} P) \tag{1.29}$$

Where c_f is the friction coefficient and σ'_{duct} is the ductile yield stress gradient. If the stress exceeds the yield stress σ_y, the viscosity gets reduced to an effective viscosity given by:

$$\eta_{\mathrm{eff}} = \frac{\sigma_{\mathrm{y}}}{2\dot{\epsilon_{\mathrm{II}}}} \quad \text{if} \quad 2\eta\epsilon_{\mathrm{II}} > \sigma_y \tag{1.30}$$

Where $\dot{\epsilon_{\mathrm{II}}}$ is the second invariant of the strain rate tensor and η is calculated using Equation 1.27.

1.3.6 Algorithm to detect and track thermal anomalies

To quantify the mobility and position of thermal anomalies (i.e. "plumes" for hot rising material, and "downwellings" for cold sinking material), we constructed a plume detection and tracking algorithm. We adopt a similar approach as in Labrosse (2002) where plumes and downwellings are identified using a thermal threshold that depends on depth: For each point of the temperature field, the threshold determines if it is part of a plume, a downwelling or neither. The plumes and downwellings can then be connected using a connected component analysis or using a k-means clustering analysis. Here, we identify plumes and downwellings only as a function of longitude: For each longitude bin, we determine the number of temperature points that are below (downwelling) or above (plume) the temperature threshold. The plumes and downwellings are then identified from the resulting histogram. The width of the bins is chosen depending on the number of longitudinal grid points. A width that is too small may lead to splitting of plumes/downwellings whereas a too large width might lead to a non-detection.

1.3.7 Magma ocean parametrisation

If the insolation from the host star is high enough a magma ocean can form (Section 1.1.5). A magma ocean behaves rheologically as a liquid (viscosity on the order of 1 Pa s) and is vigorously convecting, whereas the solid mantle behaves like a highly viscous fluid. For example, Earth's mantle viscosity ranges from 10^{19} to 10^{24} Pa s (e.g., Anderson, 1966) . In reality, numerical schemes cannot accommodate that many order of magnitudes difference of viscosity, as the dynamic regime of the magma ocean is very different from the solid mantle. We therefore parametrise the heat transport within the magma ocean. Because the magma ocean is vigorously convecting and therefore heat transport is very efficient, we model heat transport inside the magma ocean by assuming a very high thermal conductivity (eddy diffusivity). The heat flux inside the magma ocean is parametrised using (e.g., Abe, 1997; Lourenço et al., 2020):

$$J_q = -k_h \left[\frac{\partial T}{\partial r} - \left(\frac{\partial T}{\partial r} \right)_a \right] - k \frac{\partial T}{\partial r} \tag{1.31}$$

Where k is the thermal conductivity, $\left(\frac{\partial T}{\partial r}\right)_a$ is the adiabatic temperature gradient, and k_h is the effective thermal conductivity of the melt. We calculate k_h depending on the melt fraction ϕ and the rheological transition ϕ_c using:

$$k_h = \frac{k_{\mathrm{h,max}}}{2} \left[1 + \tanh \left(\frac{\phi - \phi_c}{\Delta \phi_c} \right) \right] \tag{1.32}$$

Where $k_{\mathrm{h,max}}$ is the maximum effective thermal conductivity, which we fix for our models. $\Delta\phi_c$ is a parameter that controls the width of the rheological transition. The temperature distribution inside the magma ocean is nearly adiabatic and isentropic (Solomatov, 2007). For a one-phase system, the adiabatic temperature profile is given by:

$$\frac{dT}{dP} = \frac{\alpha T}{\rho c_p} \tag{1.33}$$

We include latent heating effects occurring in the mixed region ($0 < \phi < 1$) by assuming an effective heat capacity C_p' and an effective thermal expansion parameter

α' in the energy equation (e.g., Solomatov, 2007):

$$C_p' = C_p + \frac{\Delta H}{T_{\text{liq}} - T_{\text{sol}}} \tag{1.34}$$

Where T_{sol} is the solidus and T_{liq} the liquidus temperature.

$$\alpha' = \alpha + \frac{\Delta \rho}{\bar{\rho}(T_{\text{liq}} - T_{\text{sol}})} \tag{1.35}$$

Where ΔH is the latent heat of melting, $\Delta \rho$ is the density difference between the solid and melt phase and $\bar{\rho}$ is the volumetrically averaged density. We fix the latent heat of melting/freezing as $\Delta H = 600\,\text{kJ/kg}$ and the density difference between the melt and solid phase is determined using:

$$\Delta \rho = \frac{\Delta H \bar{\rho}^2}{\gamma T} \tag{1.36}$$

Where γ is the Clapeyron slope of the solid-melt phase transition, which is given by:

$$\gamma = \frac{\bar{\rho} g}{\frac{dT_m}{dz}} \tag{1.37}$$

Where $\frac{dT_m}{dz}$ is the phase-averaged slope of the melting curves:

$$\frac{dT_m}{dz} = \phi \frac{dT_{\text{liq}}}{dz} + (1 - \phi) \frac{dT_{\text{sol}}}{dz} \tag{1.38}$$

Chapter 2

Hemispheric tectonics on super-Earth LHS 3844b

This chapter has been published as Meier, T.G., Bower, D.J., Lichtenberg, T., Tackley, P.J. and Demory, B.-O (2021). Hemispheric tectonics on Super-Earth LHS 3844b. *The Astrophysical Journal*, 908, L48

The version included in this thesis is published as arXiv preprint with identifier *arXiv:2103.02374*.

Abstract

The tectonic regime of rocky planets fundamentally influences their long-term evolution and cycling of volatiles between interior and atmosphere. Earth is the only known planet with active plate tectonics, but observations of exoplanets may deliver insights into the diversity of tectonic regimes beyond the solar system. Observations of the thermal phase curve of super-Earth LHS 3844b reveal a solid surface and lack of a substantial atmosphere, with a temperature contrast between the substellar and antistellar point of around 1000 K. Here, we use these constraints on the planet's surface to constrain the interior dynamics and tectonic regimes of LHS 3844b using numerical models of interior flow. We investigate the style of interior convection by assessing how upwellings and downwellings are organized and how tectonic regimes manifest. We discover three viable convective regimes with a mobile surface: (1) spatially uniform distribution of upwellings and downwellings, (2) prominent down-

welling on the dayside and upwellings on the nightside, and (3) prominent downwelling on the nightside and upwellings on the dayside. Hemispheric tectonics is observed for regimes (2) and (3) as a direct consequence of the day-to-night temperature contrast. Such a tectonic mode is absent in the present-day solar system and has never been inferred from astrophysical observations of exoplanets. Our models offer distinct predictions for volcanism and outgassing linked to the tectonic regime, which may explain secondary features in phase curves and allow future observations to constrain the diversity of super-Earth interiors.

2.1 Introduction

Plate tectonics is the unifying theory of Earth Science that explains the geological and surface evolution of Earth for at least the past 3 Gyr. Plate tectonics is a fundamental component of long-term (geological) cycles that enable exchange of volatiles between the interior and atmosphere. These cycles regulate climate and provide the necessary ingredients to nurture and sustain life on Earth and are thus essential to understanding the habitability of distant worlds. The discovery of plate tectonics on Earth arose from seafloor mapping and seismology, but these techniques cannot be used to discern tectonic regimes on rocky exoplanets. Instead, observations of the thermal phase curve are available for select planets. Here, we link phase curve observations to numerical models of interior flow and constrain the possible tectonic regimes of super-Earth LHS 3844b.

Since the first thermal map of a super-Earth was constructed for super-Earth 55 Cnc e (Demory et al., 2012, 2016b), other super-Earths have been targeted with observations to constrain their thermal emission and thus constrain their day- and nightside temperatures. Recent efforts focused on LHS 3844b have found coincidence between the substellar point and the observed hotspot, and inferred a dayside temperature of 1040 ± 40 K and a nightside temperature around 0 K (Kreidberg et al., 2019). These suggest that heat redistribution is inefficient; therefore the planet has neither substantial melt at its surface nor an active atmosphere. The observational data suggests the emission originates from bare rock with a low albedo (Kreidberg et al., 2019). Therefore, LHS 3844b has established itself as a case study for under-

standing the interior dynamics and tectonics of ultra-short period super-Earths.

Whether or not plate tectonics (mobile lid convection) operates on super-Earths has been a long-standing debate (e.g., Valencia et al., 2006; O'Neill et al., 2007), but the debate is notably hindered by the lack of observational constraints to supplement theoretical and numerical modeling efforts. Tectonic regimes manifest from the interior dynamics of a planet, specifically the style and vigor of convection in the outermost silicate shell (the mantle). Hence tectonic regimes are the surface expression of mantle flow that extends deep in the planet. Therefore, introducing observational constraints into models is essential to provide new insights into the viable tectonic regimes operating on rocky exoplanets such as LHS 3844b.

It is unknown how the strong temperature contrast imposed by stellar irradiation on LHS 3844b influences its interior flow and hence its tectonic regimes. Thus we utilize advanced models of interior flow coupled with thermal phase curve observations to determine the viable convective regimes operating in the interior of an ultra-short period super-Earth. This enables us to probe the coupling between the surface and interior of LHS 3844b and thereby infer observational strategies for further geological characterization.

2.2 Constraining interior dynamics with observations

LHS 3844b is 1.3 Earth radii (Vanderspek et al., 2019) and the dayside and nightside temperatures are 1040 K and $\approx$ 0 K, respectively (Kreidberg et al., 2019). We estimate the longitudinal temperature variation by assuming a blackbody at equilibrium and that only the dayside reradiates energy received from the star. Since the thermal phase curve only constrains the average longitudinal dependence of surface temperature, we construct models of interior flow within 2D spherical annulus geometry (Hernlund and Tackley, 2008). Mantles behave as highly viscous fluids, so we solve for Stokes flow (mass, momentum, and energy conservation) using the mantle convection code StagYY (Tackley, 2008). Since the mass of LHS 3844b has not been measured, we assume its mantle is silicate rock and has the same relative thickness as Earth. We adopt a hydrostatic reference state to provide the mantle

profiles of material properties (Tackley et al., 2013). Utilizing an Arrhenius-type viscosity law, the mantle is modeled with an upper mantle, a perovskite layer, and a post-perovskite layer assuming a lower bound estimate of the viscosity (Tackley et al., 2013). The perovskite-post-perovskite interface occurs at a depth around 1680 km (total mantle depth is ≈3500 km).

Lithospheric strength is modeled by a plastic yielding criteria (σ_{duct}) to obtain self-consistent plate-like behavior (Moresi and Solomatov, 1998; Tackley, 2000). Laboratory experiments estimate the yield stress to be a few hundred MPa (Kohlstedt et al., 1995) and numerical simulations employ a yield stress less than $\sim$ 150 MPa to obtain plate-like behavior for Earth-like planets (Tackley, 2000). We vary the ductile yield stress between 10 MPa and 300 MPa to model a lithosphere that is weak and strong, respectively. Planetary mantles can be heated from below from cooling of an iron-rich (geophysical) core and heated from within from decay of radionuclides or tidal heating. We therefore explore two heating modes: (1) basal heating, where the mantle is heated exclusively by the geophysical core, and (2) mixed-mode heating, where constant mantle heat production (Earth-like at 5.2×10^{-12} W kg$^{-1)}$ supplements heating by the core. Kane et al. (2020) estimate the age of the host star as 7.8 ± 1.6 Gyr, but an estimate of the stellar radionuclide abundances is presently not available to provide a constraint on the radiogenic heat budget of the planet (e.g., Unterborn et al., 2015). Therefore, we assume an Earth-like internal heat budget, in accordance with previous modeling efforts (e.g., Kane et al., 2020).

2.3 Tectonic regimes and interior flow

Our simulations discover three mobile lid tectonic regimes, each of which is associated with a distinct interior temperature and flow field: (1) uniform distribution of upwellings and downwellings (Figs. 2.1A and 2.2A), (2) downwellings on the dayside and upwellings on the nightside (Figs. 2.1B, D and 2.2B, D), and (3) downwellings on the nightside and upwellings on the dayside (Figs. 2.1C and 2.2C). Figure 2.1 shows the mantle temperature for three times of each model where the substellar point is located at 0 degrees. Figure 2.2 shows evolutionary tracks that summarize the distribution of upwellings (red tracks) and downwellings (blue tracks) with

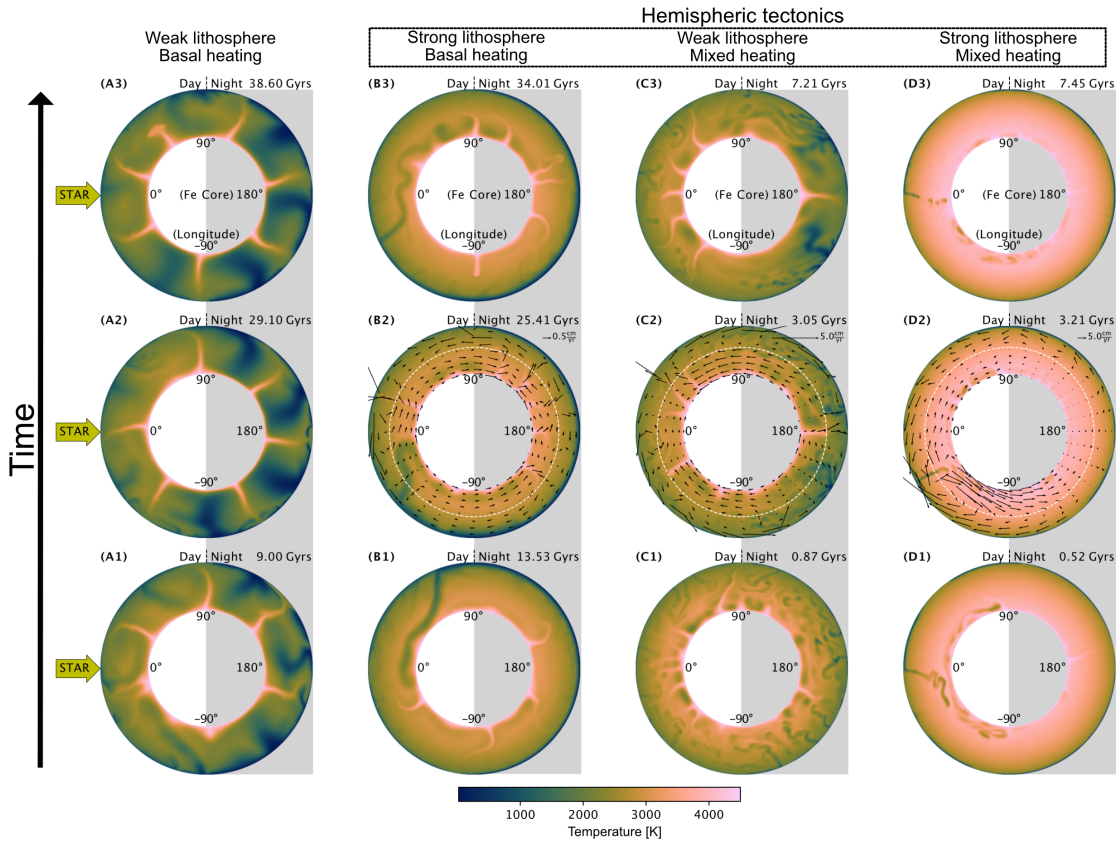

Figure 2.1 | Mantle temperature for tectonic regimes of LHS 3844b for (A) weak lithosphere (σ_{duct}= 10 MPa) and basal heating, (B) strong lithosphere (σ_{duct}= 300 MPa) and basal heating, (C) weak lithosphere (σ_{duct}= 10 MPa) and mixed heating, and (D) strong lithosphere (σ_{duct}= 300 MPa) and mixed heating. Upper left label in each cross-section (A3, B3, etc.) indicates the time of the cross-section in Figure 2.2. The substellar point is at 0° longitude and the nightside (90° – 270°) is denoted by a gray background. White dashed line in the mid-mantle in B2, C2, and D2 shows the boundary between perovskite (low pressure) and post-perovskite (high pressure).

longitude and time. The time of the corresponding temperature fields in Fig. 2.1 is indicated by horizontal dashed lines in Fig. 2.2. The internal heating ratio (e.g., Korenaga, 2017) is zero (by definition) for the basally heated models and between 0.7 and 0.8 for the internally heated cases. The time-averaged core–mantle boundary (CMB) heat flux is ≈ 70 mW m^{-2} and ≈ 50 mW m^{-2} for the internally heated weak and strong lithosphere models, respectively. For the basally heated models, the CMB heat flux is ≈ 95 mW m^{-2} and ≈ 65 mW m^{-2} for the weak and strong lithosphere models, respectively.

2.3.1 Uniform distribution of upwellings and downwellings

A uniform distribution of upwellings and downwellings is predicted if the planet is dominantly basal heated and has a weak lithosphere (Figs. 2.1A and 2.2A). However, downwellings are stronger on the nightside than the dayside because the upper thermal boundary layer imposes a larger temperature contrast between the surface and the interior (Fig. 2.1A). This results in strong downwellings since the contrast determines both thermal buoyancy as well as material strength through viscosity. High viscosity downwellings dictate the long-wavelength pattern of flow and thus shepherd the upwellings (also known as plumes, orange/pink structures in Fig. 2.1A) along the core–mantle boundary (CMB) into position between the downwellings. The pinning of plumes by downwellings is evident by the longitudinal stability of the upwelling and downwelling tracks over several Gyrs (Fig. 2.2A).

Both the downwellings and the upwellings exhibit little lateral migration in longitude, only oscillating back and forth by 45–60 degrees. Low viscosity upwellings mirror the migration of high viscosity downwellings, maintaining a constant separation at all times (Fig. 2.2A). This occurs for the dayside and the nightside, even though the downwellings are weaker on the dayside. The evolutionary tracks in Fig. 2.2A also reveal that upwellings and downwellings are maintained by a constant draining of the upper and lower thermal boundary layer, respectively. Hence once the arrangement of downwellings and upwellings is established in the interior, they tend to persist and no new boundary layer instabilities occur. Therefore both the day- and nightside only exhibit a small amount of time-dependent flow.

2.3.2 Hemispheric tectonics: downwellings on dayside

A dominant downwelling on the dayside and upwellings on the nightside are predicted with a strong lithosphere, independent of the heating mode (Figs. 2.1B, D and 2.2B, D). A degree-1 convection pattern is established and hence hemispheric tectonics operates at the surface. Figures 2.1B and 2.2B show the temperature for the basally heated model with a strong lithosphere. A prominent downwelling forms on the dayside and descends into the deep mantle (Fig. 2.1: B1). It flushes hot material from the lower thermal boundary layer around the CMB from the dayside to the nightside, thereby promoting plumes on the nightside that rise to the surface

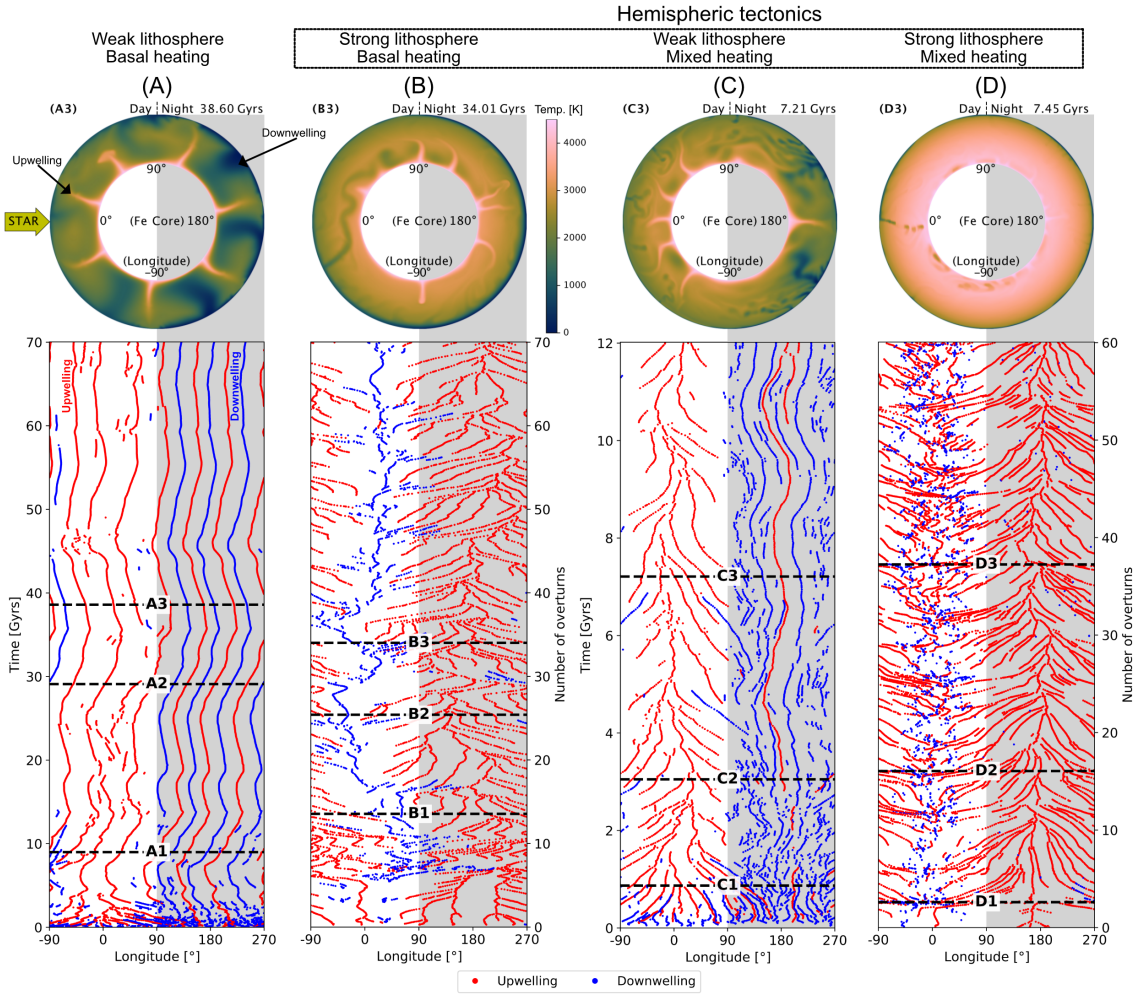

Figure 2.2 | Evolutionary tracks for tectonic regimes of LHS 3844b. Cross-sections (A3, B3, C3, and D3) show arrangement of upwellings and downwellings in the mantle. Below, the evolution charts show the longitude of upwellings (red) and downwellings (blue) as a function of time. Horizontal dashed lines denote the times of the cross-sections including those in Fig. 2.1. The substellar point is at 0° longitude and the nightside (90° – 270°) is denoted by a gray background.

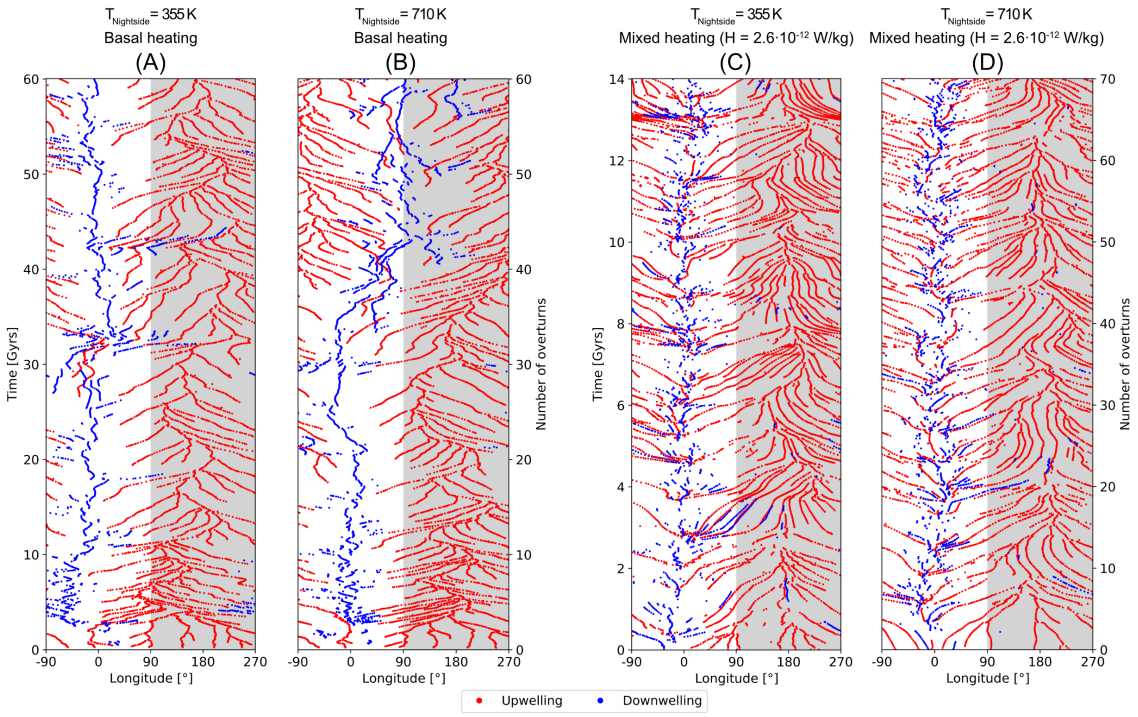

Figure 2.3 | Evolutionary tracks for the strong lithosphere case with a higher nightside temperature (based on observational uncertainty) and reduced internal heating rate compared to the reference cases (Fig. 2.2: B, D). (A) basal heating and $T_{\mathrm{Nightside}} = 355$ K, (B) basal heating and $T_{\mathrm{Nightside}} = 710$ K, (C) mixed heating (half the reference rate) and $T_{\mathrm{Nightside}} = 355$ K, and (D) mixed heating (half the reference rate) and $T_{\mathrm{Nightside}} = 710$ K. Hemispheric tectonics persist throughout this parameter variation.

(Fig. 2.1: B2, B3). This deep mantle flow from dayside to nightside is accommodated in the post-perovskite layer, whereas the return flow is established in the perovskite layer above and delivers cold material from the nightside to the dayside (Fig. 2.1: B2). The near-surface advection of cold material from the nightside to the dayside thickens the upper thermal boundary layer on the dayside, which helps to sustain the prominent downwelling.

Figure 2.2B shows that the downwelling (blue track) remains close to the substellar point (0°) rather than to the day–night terminator (90° or -90°). The downwelling displaces hot material laterally along the CMB, thereby promoting the thickening of the lower thermal boundary layer and hence plume formation. This leads to the initiation of upwellings on the dayside that are pushed toward the nightside (Fig. 2.1: B3). This is evident in the evolutionary tracks (Fig. 2.2B, red), where upwellings migrate up to 180° from near the substellar point to rise near the antistellar point (180°).

A similar degree-1 convection pattern is observed for a planet with a strong lithosphere and a mixed heating mode (Fig. 2.1D). The single downwelling is weak since a majority of the lithosphere is sufficiently strong to resist dynamic instability (Fig. 2.1: D3). Furthermore, high mantle temperature ($\approx$ 3488 K) due to internal heating causes the downwelling to dissipate quickly and also reduces the temperature contrast (hence thermal buoyancy) of upwellings. Although the downwelling is weak, the high mantle temperature ensures material flows readily due to the temperature dependence of viscosity. Therefore, a degree-1 flow regime is established with comparable interior velocities as for a purely basally heated planet where the downwelling is stronger but the mantle cooler (compare Fig. 2.1: B2 and Fig. 2.1: D2). The sweeping of hot material to the nightside by the downwelling is evident in Fig. 2.1(D1) and Fig. 2.2(D).

We also investigated if hemispheric tectonics persist for higher nightside temperatures based on the uncertainty from the observations (Kreidberg et al., 2019). For basal heating with nightside temperatures of 355 and 710 K, we find that hemispheric tectonics (downwellings on dayside) persist (Figs. 2.3A, B). Similarly, hemispheric tectonics also persist when the internal heating rate is a factor of 2 less than the reference models (Figs. 2.3C, D).

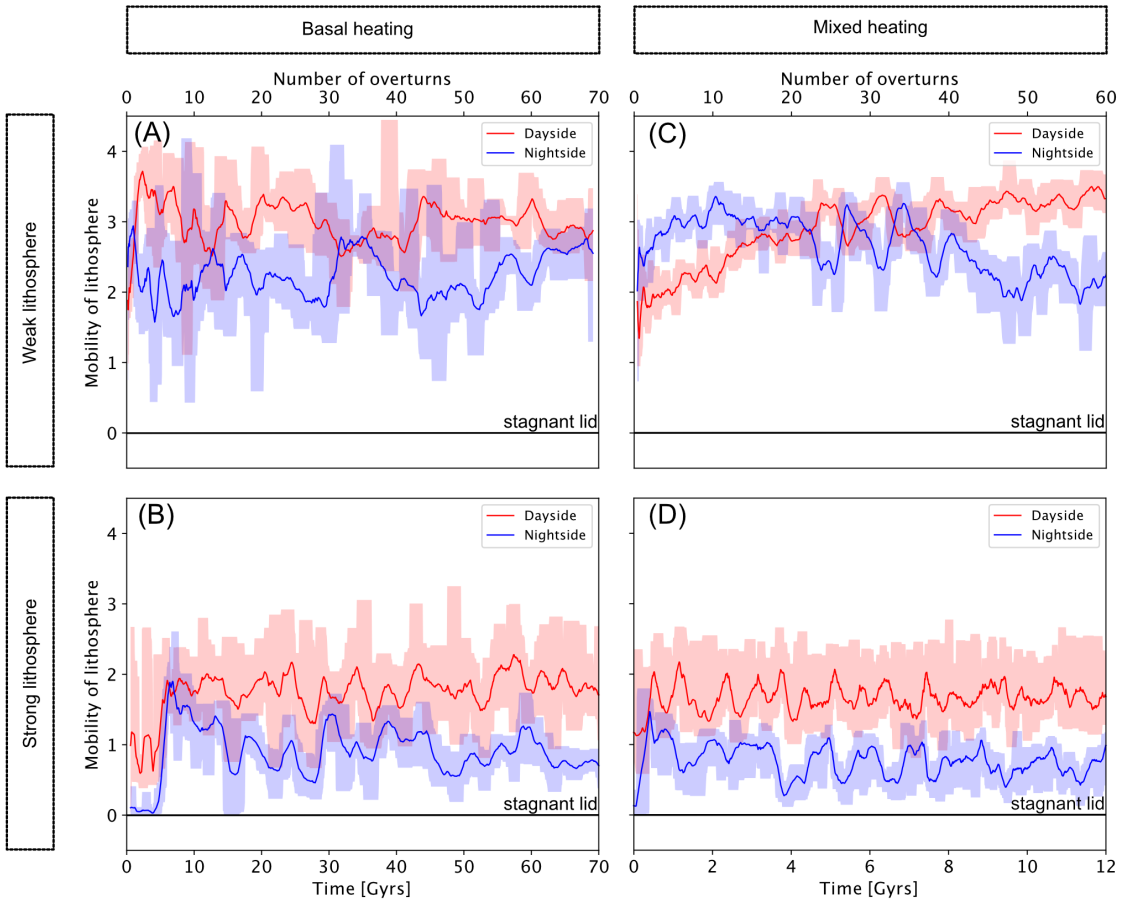

Figure 2.4 | Surface mobility, which is the ratio of the root mean square (rms) surface velocity to the RMS of the convective velocity in the mantle (Earth mobility is around 1.3). Red and blue lines show the dayside and nightside, respectively. The shaded regions on either side of the line represent the minimum and maximum values.

2.3.3 Hemispheric tectonics: downwellings on the nightside

We observe another hemispheric tectonic regime if the planet has a weak lithosphere and mixed heating mode (Figs. 2.1C and 2.2C). A degree-1 pattern is established and now strong downwellings occur on the nightside and upwellings accumulate on the dayside (Fig. 2.1: C3). Unlike the previous hemispheric regime (a single downwelling on the nightside), there are several downwellings on the nightside as demonstrated by two prominent downwelling tracks either side of the antistellar point (Fig. 2.2C, blue) and transient downwellings that occur closer to the day–night terminator. Weak downwellings form on the dayside, although these tend to remain in the perovskite layer and do not propagate to depth in the post-perovskite layer (Fig. 2.1: C3, C2). A prominent upwelling forms at the antistellar point (180°) that remains stable and exhibits minimal lateral movement (Fig. 2.1: C3), anchored by the two prominent downwellings on either side (Fig. 2.2C). The degree-1 pattern of convection is once again driven by downwellings that propagate to depth, in this case on the nightside. The downwellings sweep hot material in the post-perovskite layer along the CMB toward the dayside, where plumes rise and merge at the substellar point. A return flow is established in the upper perovskite layer where warm material from the surface of the dayside is advected to the cooler antistellar point (Fig. 2.1: C2).

2.4 Implications

2.4.1 Hemispheric tectonics and surface mobility

Our numerical simulations that are constrained by phase curve observations suggest that LHS 3844b may exhibit persistent hemispheric tectonics due to the approximately 1000 K temperature contrast between its day- and nightside. Hemispheric tectonics are not inferred for any solar system planet at present day. Currently Earth has a dominant degree-2 pattern of convection, as dictated by downwellings in the Pacific and broad hot anomalies (possibly upwellings) beneath Africa and the Pacific Ocean. Transient hemispheric tectonics on Earth may occur during supercontinent formation (landmasses assemble on one hemisphere), but according to the geological

record this is not a stable and long-lived configuration. Venus does not have a mobile surface driven by persistent downwellings, but rather its crustal thickness and mean surface age suggests episodic overturn of the surface (Rolf et al., 2018). Observations support a prominent role for upwellings to explain surface features (coronae) and active upwellings may cluster in Venus' southern hemisphere (Gülcher et al., 2020). However, these upwellings are not shepherded into the southern hemisphere by persistent downwellings in the northern hemisphere.

For Mars, a transient degree-1 convection pattern may have initiated following a giant impact that generated massive magmatism to source a Tharsis-like volcanic province (Golabek et al., 2011). However, a mobile surface on Mars lasted for only half a billion years or so, after which it transitioned to a stagnant lid (no surface mobility; (Zhang and O'Neill, 2016)). In numerical models of a generic tidally locked Earth-sized planet, Van Summeren et al. (2011) observe downwellings on the nightside and upwellings on the dayside; we now find that a similar regime can manifest for a larger rocky planet (LHS 3844b) using phase curve observations and fluid simulations appropriate for a super-Earth interior. We also discover a previously unrecognized regime of hemispheric tectonics that is characterized by downwellings on the dayside and upwellings on the nightside. Hence our data-constrained models emphasize the importance of hemispheric tectonic regimes to interpret observations of rocky exoplanets.

For a strong lithosphere, convective stresses in the interior are insufficient to yield the nightside lithosphere and promote downwellings. Instead, the nightside lithosphere establishes a surface return flow to the dayside that accommodates the deep flow of material from the day- to the nightside initiated by downwellings (Figs. 2.1B, D). As the cold lithosphere is transported to the dayside, it becomes warmer and accommodates more deformation. All models produce mobile surfaces, so even the strong lithosphere models do not prevent surface motion (Fig. 2.4). Neither the dayside nor nightside transition to a stagnant lid with zero surface velocity (Fig. 2.4). We recover a stagnant lid regime in models (not shown) without plastic yielding (i.e. $\sigma_{\text{duct}} \rightarrow \infty$ MPa) and find no interior dichotomy due to the lack of downwellings. Instead, weak upwellings are approximately uniformly distributed but become stifled by interior heat production that raises the mantle temperature.

We consider lithospheric strength to depend on lithospheric composition, which we assume to be uniform. Future work could investigate the effects of temperature dependent yield stress. For our models with a strong lithosphere, the high temperature on the dayside reduces the viscosity of the lithosphere sufficiently to allow it to flow and sink. High temperature would likely decrease the plastic yielding parameter, further facilitating downwellings on the dayside (Hansen et al., 2019) and preventing downwellings on the nightside (where the yielding parameter would increase). Hence the asymmetry between the flow on the dayside and nightside would be further enhanced and increase the likelihood of hemispheric tectonics. Finally, melting and crustal production would likely increase the overall mobility of the lithosphere (Lourenço et al., 2016).

2.4.2 Plumes, volcanism, and observations

Upwellings (plumes) form through two types of interactions with downwellings (e.g., Tan et al., 2002). First, the leading edge of downwellings sweep hot material along the CMB to form upwellings (e.g., Fig. 2.1(B1)). For hemispheric tectonics, this causes the partitioning of upwellings in one hemisphere and downwellings in the other hemisphere. Second, upwellings can form beneath downwellings since cold downwellings trap hot material beneath, thus enabling incipient plumes to accumulate buoyancy before breaking through and rising to the surface (e.g., Fig. 2.1(B3), 30°). A long-lived cluster of upwellings in a particular hemisphere may promote extensive magmatism and volcanism. For example, upwellings can explain the origin of some large igneous provinces (LIPs) on Earth, which are large surface emplacements of basaltic magma (e.g., Coffin and Eldholm, 1994). LIPs drive extensive outgassing (e.g. CO_2, Black and Gibson, 2019) and climate modification. Our models reveal that plumes can be evenly distributed in the interior, preferentially on the dayside, or preferentially on the nightside. For a uniform distribution, where upwellings are pinned in place by downwellings, upwellings only sample deep mantle material from a small region at the CMB (around 60°). For hemispheric tectonics, plumes are instead flushed around the CMB to the opposite hemisphere, thereby sampling a much larger fraction of the deep interior and delivering this chemical signature to the near-surface.

We time-average the surface heat flux from the interior and determine its contribution to the thermal phase curve. The thermal phase curve that is applied as the surface boundary condition in our reference models is shown in Fig. 2.5a. Figure 2.5b shows the nightside thermal phase curve including the interior contribution. The dayside phase curve is not shown since the interior heat flux is negligible compared to stellar insolation such that it has little influence on the surface temperature. The nightside is a favorable target for observing the heat contribution from the interior due to temperatures around 0 K for an atmosphere-less planet (no reflected light or reradiation of the host star's light). An interior heat contribution, as dictated by the interior convective regime, could produce a variation of the geometric transit depth (Kipping and Tinetti, 2010). However, the expected spectral signatures are significantly below the ppm-level in the near-to-mid infrared, which is beyond the capabilities of current or planned instrumentation (Fig. 2.5).

On the dayside, which is observed during the secondary transit, the contribution of the interior heat flux to the eclipse depth would be on the same order of magnitude as for the transit depth. A further complication for the secondary transit is that deconvolving the interior flux from stellar contributions requires knowledge of the stellar spectrum and planetary surface properties (to determine the reflected, absorbed, and reradiated light). Thus, it may be difficult to observe the contribution from the interior heat to the thermal phase curve if heat is conducted through a solid lid. However, if massive outpourings of melt occur on the surface associated with plumes (akin to LIPs), this will generate regions of high heat flux and possibly provide a means to test the existence of hemispheric tectonics with future astrophysical observations. Furthermore, if upwellings facilitate or source outgassing of volatiles on one hemisphere, this may perturb the atmospheric composition and properties on this hemisphere. This may similarly produce a secondary signal in multiwavelength phase curve observations, in addition to the dominant signal from the day–night temperature contrast.

Parameterized stagnant lid models of volcanic outgassing and atmospheric erosion show that the lack of an atmosphere for LHS 3844b is consistent with a volatile poor mantle (Kane et al., 2020). Our stagnant lid models produce a uniform distribution of upwellings, which implies spatially uniform melting and outgassing at

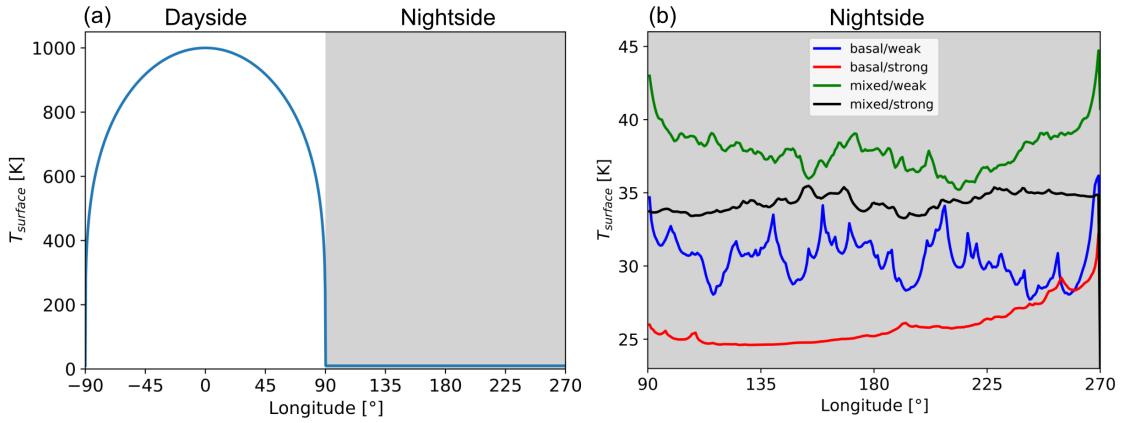

Figure 2.5 | (a) Imposed surface temperature motivated by the thermal phase curve of LHS 3844b (b) Thermal phase curves of the nightside of LHS 3844b that include the contribution of the heat flux from the interior.

the surface. Upwellings in the stagnant lid regime are laterally mobile because they are not anchored in place by downwellings. Kane et al. (2020) find that the heat-producing element budget, mantle viscosity, and initial temperature, do not have a significant influence on the size of the atmosphere of LHS 3844b. However, hemispheric tectonics could lead to differences in melt production and outgassing between the dayside and nightside, potentially modifying the size and chemical composition of an atmosphere. If LHS 3844b is devoid of an atmosphere and has a volatile poor mantle, we can preclude weakening of the lithosphere by surface water. This suggests LHS 3844b has a strong lithosphere, lending support to hemispheric tectonics characterized by a downwelling on the dayside and upwellings on the nightside.

2.5 Conclusions

Our numerical experiments suggest that hemispheric tectonics may operate on LHS 3844b, where one hemisphere is characterized by downwellings and the opposite hemisphere by upwellings. For hemispheric tectonics, upwellings may lead to preferential melt generation and outgassing on one hemisphere that could manifest as a secondary signal in phase curve observations. However, the contribution to the thermal phase curve from the interior flux is on the order of 15–30 K, which would produce spectral signatures that are significantly below the ppm level in the near-to-mid infrared, and will therefore be challenging to detect by current and near-future observations. Nevertheless, outpourings of melt (extrusive volcanism) with high

temperature (> 1000 K) fueled by deep mantle upwellings could imprint a signature in the thermal phase curve. If melting is more prevalent on one hemisphere, the associated degassing of volatiles could preferentially perturb the composition and properties of a thin and transient atmosphere on that side of the planet.

Appendix

2.A Spectral signatures from interior heat flux

Figure 2.5 shows that the interior heat contribution is on the order of 20–45 K. In this section, we elaborate on how this translates into spectral signatures that are significantly below the ppm-level in the near-to-mid infrared.

The eclipse depth (assuming no reflection) in a given bandpass is given by (Charbonneau et al., 2005):

$$\Delta F_{\mathrm{II}} = \left(\frac{R_p}{R_*}\right)^2 \frac{\int F_p(\lambda) S(\lambda)(\lambda/hc) d\lambda}{\int F_*(\lambda) S(\lambda)(\lambda/hc) d\lambda} \tag{2.1}$$

Where λ is the wavelength, R_p is the radius of the planet, R_* the radius of the star, F_p is the flux from the planet, F_* the flux from the star, S(λ) the spectral response function, h is Planck's constant and c the speed of light. The factor $\lambda/(hc)$ converts the fluxes into a photon-weighted flux and the spectral response function converts the number of photons into electrons, which depends on the instrument. Here, we assume that the filter bandwidths are narrow, so that we can therefore ignore the spectral response function. We also assume that the flux is given by Planck's law:

$$F(\nu, T) = \frac{2h\nu^3}{c^2} \frac{1}{e^{h\nu/(kT)} - 1} \tag{2.2}$$

Figure 2.6 shows the different eclipse depths in ppm for the Mid-Infrared Instrument (MIRI) of the James Webb Space Telescope (JWST). As one can see, if the interior contribution to the surface temperature is only 20–40 K, this would only lead to a fraction of ppm for planet with the size of LHS 3844b ($1.3 R_\oplus$).

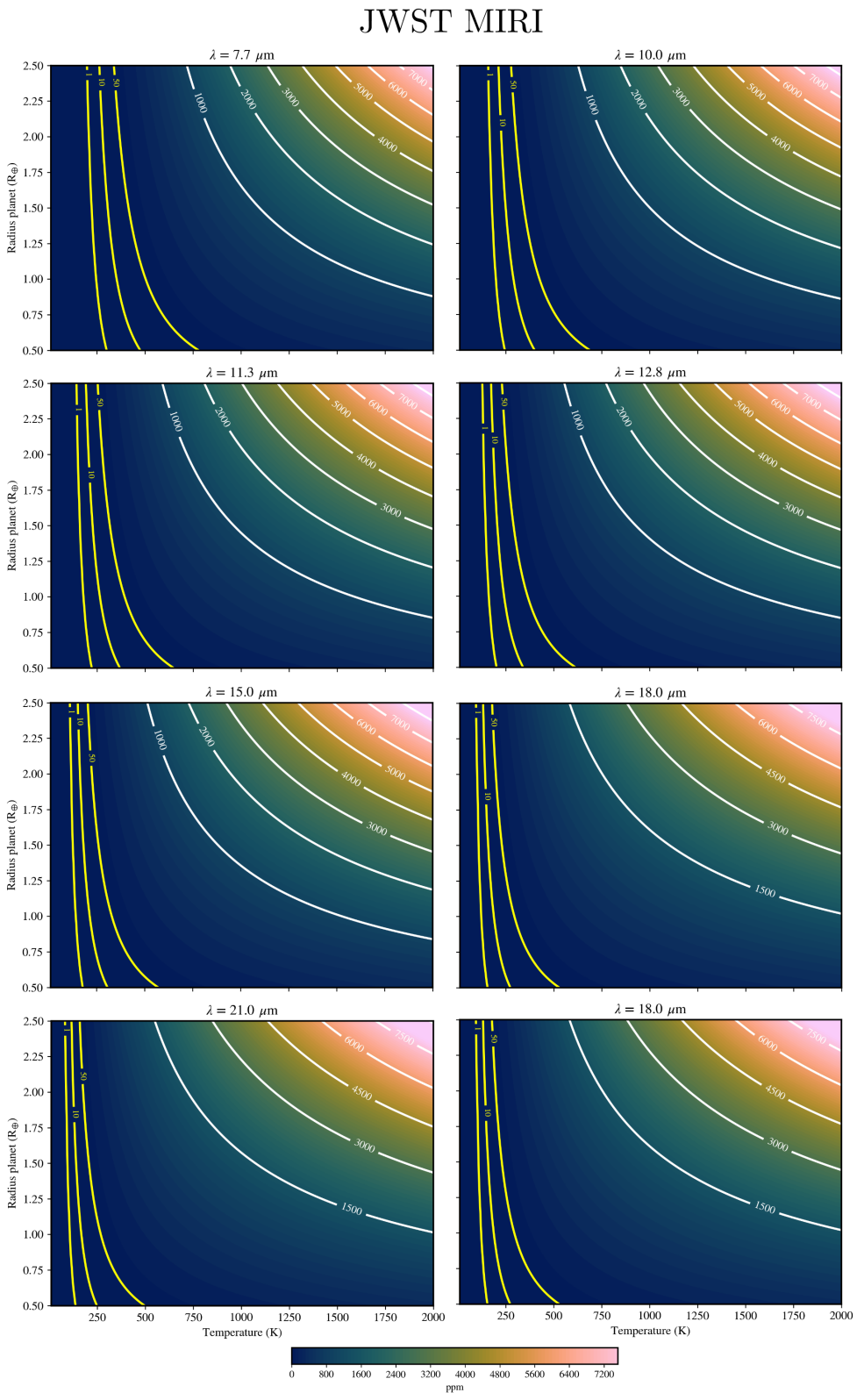

Figure 2.6 | Eclipse depths (in ppm) for different MIRI (Mid-Infrared Instrument) wavelengths assuming different temperatures and sizes of the planet. The eclipse depth is calculated using equation (2.1). The contours show a selection of constant-ppm levels. LHS 3844b has radius of $1.3R_\oplus$ and the interior heat contribution to the surface temperature is on the order of 20–45 K, which would only lead to a fraction of ppm eclipse depth even for $\lambda = 18\,\mu$m

2.B Additional figures

Figure 2.5(b) shows the temperature of the nightside including the contribution of the heat flux from the interior. Figure 2.7 shows the heat flux from the interior. To convert the time-averaged heat flux into a temperature we use the Stefan-Boltzmann law:

$$F = \sigma T^4 \tag{2.3}$$

Where $\sigma = 5.670 \cdot 10^{-8}\,\mathrm{Wm^{-2}K^{-4}}$ is the Stefan-Boltzmann constant.

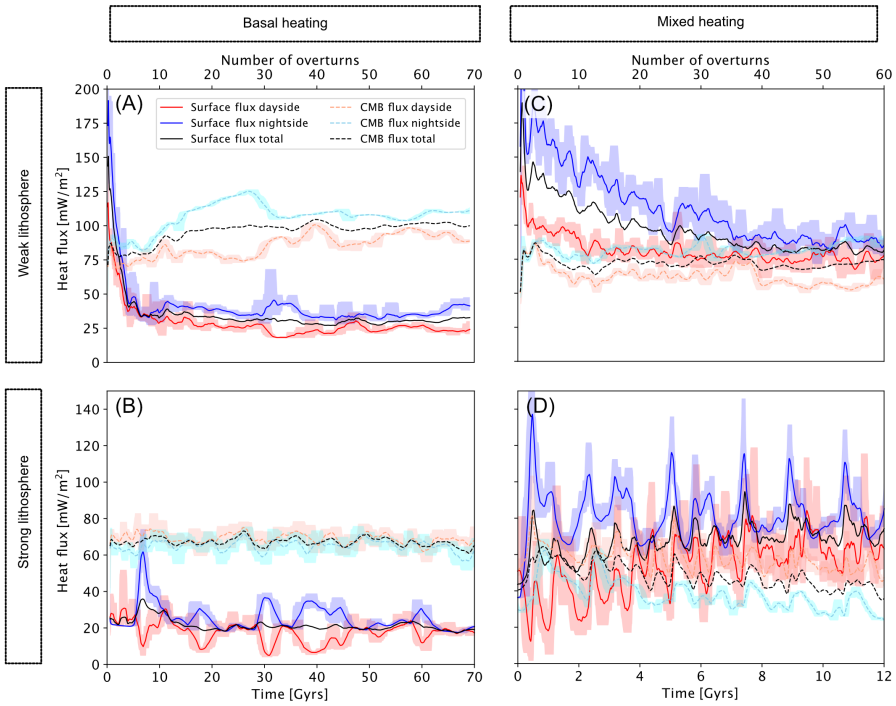

Figure 2.7 | Surface heat flux from the interior for super-Earth LHS 3844b. Red and blue lines show the dayside and nightside, respectively. The shaded regions on either side of the line represent the minimum and maximum values.

Figure 2.8 shows the mantle viscosity for the tectonic regimes of LHS 3844b corresponding to the mantle temperatures shown in figure 2.1.

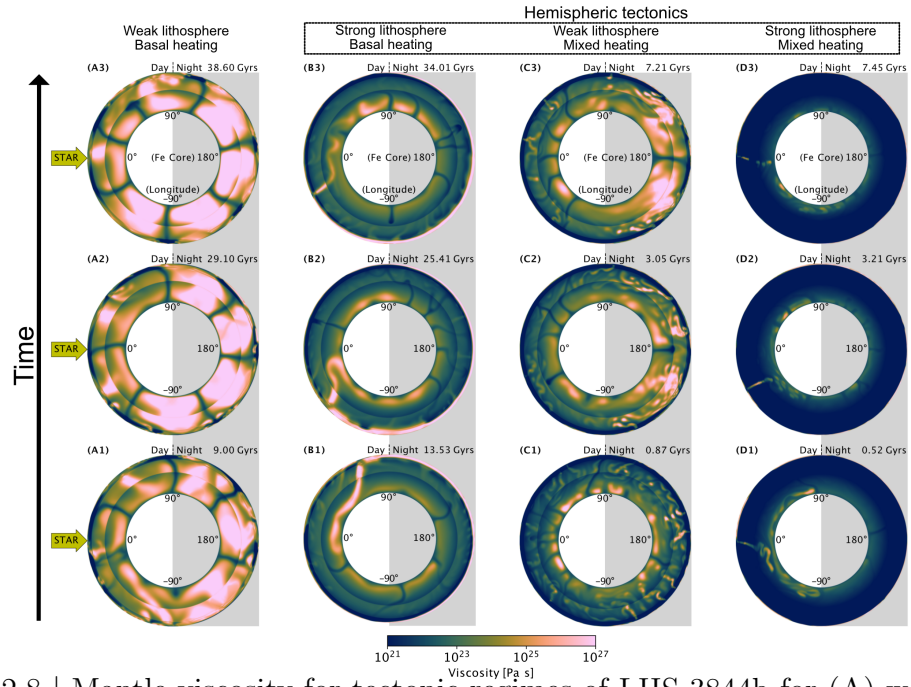

Figure 2.8 | Mantle viscosity for tectonic regimes of LHS 3844b for (A) weak lithosphere ($\sigma_{\rm duct}$= 10 MPa) and basal heating, (B) strong lithosphere ($\sigma_{\rm duct}$300 MPa) and basal heating, (C) weak lithosphere ($\sigma_{\rm duct}$ = 10 MPa) and mixed heating, and (D) strong lithosphere ($\sigma_{\rm duct}$ = 300 MPa) and mixed heating. The substellar point is at 0° longitude and the nightside (90° – 270°) is denoted by a gray background.

Chapter 3

Interior dynamics of super-Earth Gliese 486b

This chapter is under preparation and is to be submitted as Meier, T.G., Bower, D.J., Lichtenberg, T., Hammond, M., and Tackley, P. J. (2022), Interior dynamics of super-Earth Gliese 486b.

Abstract

In this chapter, we build-up on our previous study of super-LHS 3844b for which we found that hemispheric tectonics is a possible tectonic regime. In such a regime, which we define as a special case of degree-1 convection, a strong downwelling forms preferentially on one hemisphere and upwellings rise on the other side. Here, we study the interior dynamics of super-Earth Gliese 486b, which has approximately the same radius as LHS 3844b ($1.3\,R_{\oplus}$). As opposed to LHS 3844b, it is not certain whether Gliese 486b was able to retain an atmosphere or not. An atmosphere would allow transport of heat from the dayside towards the nightside and thereby reduce the surface temperature contrast between the two hemispheres. We therefore investigate whether hemispheric tectonics is a possible tectonic regime also for lower surface temperature contrasts. We constrain the surface temperature contrasts with the results from general circulation models. We also investigate how the strength of the lithosphere affects the formation of degree-1 convection and/or hemispheric tectonics. We find that degree-1 convection is a consequence of the

strong lithosphere (developing for a ductile yield stress above around 125–200 MPa, depending on the surface temperatures), while hemispheric tectonics is favoured for strong temperature contrasts between the dayside and nightside and higher surface temperatures.

3.1 Introduction

Here, we investigate the possible tectonic regimes of the (most likely) tidally-locked super-Earth GJ 486b, which has a radius of 1.31 $R_\oplus$ and a mass of 2.81 $M_\oplus$ (Trifonov et al., 2021). This places Gliese 487b on the 'Earth-like' (50% enstatite, 50% iron) composition line in the mass-radius diagram (Trifonov et al., 2021). Because the planet is on a very short orbit of 1.467 days around its red dwarf host star and has a high equilibrium temperature of 700 K, it is also a suitable target for future follow-up observations that aim to characterise its potential atmosphere (Trifonov et al., 2021). It is still debated whether planets on such close orbits around their host-star are able to retain an atmosphere (Zahnle and Catling, 2017). Most super-Earths are likely to lose their secondary atmosphere that was generated from magma ocean outgassing, but this atmosphere could potentially be revived through volcanic outgassing (Kite and Barnett, 2020). A secondary atmosphere has recently been detected on the Earth-like exoplanet GJ 1132 b, which orbits an M4.5 dwarf star on a 1.6 days orbit (Swain et al., 2021). Depending on the physical and chemical state of a potential atmosphere, heat circulation between the dayside and nightside will either be enhanced or oppressed. The corresponding temperature contrast could therefore be less pronounced which could lead to different tectonic regimes compared to a planet that is devoid of an atmosphere. Here, we therefore assume different types of potential atmosphere for super-Earth Gliese 486b in order to study the possible tectonic regimes that this planet might exhibit. In particular, we are interested whether a strong temperature contrast between the dayside and the nightside favours a hemispheric tectonic regime and whether efficient heat circulation inhibits hemispheric tectonics.

Here, we define hemispheric tectonics as a special case of spherical harmonics degree-1 convection (one upwelling and one downwelling), where the downwelling

gets pinned to either the dayside or nightside and the upwelling (or several upwellings) are on the other hemisphere. A degree-1 convection pattern could have existed in the mantles of Mars (e.g. Zhong and Zuber, 2001; Keller and Tackley, 2009), the Moon (e.g. Zhong et al., 2000), or Earth (e.g. Zhong et al., 2007; McNamara and Zhong, 2005). Degree-1 convection could be induced by depth- and temperature-dependence of viscosity (Yoshida and Kageyama, 2006), small core size (Zhong et al., 2000), or if the mantle viscosity is stratified with a weak asthenosphere (Zhong and Zuber, 2001; Roberts and Zhong, 2006). An endothermic phase change, such as spinel to bridgmanite and magnesiowüstite is also expected to promote long-wavelength patterns (Tackley et al., 1993). On Mars, a transient degree-1 convection pattern could have formed after a giant impact leading to massive volcanism and the formation of a large volcanic province (Tharsis) (Golabek et al., 2011; Citron et al., 2018). Earth's current convection pattern is predominantly degree-2 for at least the past 120 Myrs as indicated by Earth's subduction history (McNamara and Zhong, 2005; Zhong et al., 2007). Long-wavelength patterns are favoured for the formation of supercontinents and could have led to the formation of Pangea and other supercontinents on Earth (Yoshida and Santosh, 2011).

With the discovery of more and more rocky exoplanets, attention has been drawn towards understanding the convection patterns of these distant worlds. Van Summeren et al. (2011) have shown that a surface temperature contrast of more than 400 K is able to maintain an asymmetric degree-1 mantle convection pattern. Similarly, Gelman et al. (2011) found that tidally locked planets that receive intense insolation from their host star are more likely to develop a degree-one convection pattern with mantle upwellings preferentially located at the substellar point. In a previous study, we have analysed the possible tectonic regimes of super-Earth LHS 3844b (see Chapter 2 on the interior dynamics of super-Earth LHS 3844b). This planet has a radius of 1.3 $R_\oplus$ and is most likely devoid of an atmosphere, and its thermal phase curve observation suggest a strong surface temperature contrast with a dayside temperature of 1040 K at the substellar point and 0—700 K on the nightside (Kreidberg et al., 2019). Our study suggests that this planet might exhibit hemispheric tectonics with a strong downwelling on the dayside and upwellings that are getting pushed towards the nightside in the case of a strong lithosphere.

If the planet has a weak lithosphere, a uniform tectonic regime establishes with downwellings and upwellings uniformly distributed around the mantle (Meier et al., 2021).

Here, we investigate the effect of lithospheric strength on the degree of convection of super-Earth Gliese 486b and how these convection patterns get influenced by different surface temperature contrasts between the dayside and nightside. In particular, we will show that degree-1 convection ensues from a strong lithosphere while hemispheric tectonics is a consequence of both a strong lithosphere and a strong temperature contrast and higher surface temperatures.

3.2 Methods

As it is not known whether this planet was able to retain an atmosphere, we will use general circulation models (GCMs) to determine what the different surface temperatures on this super-Earth could be (see section 3.2.1). The core-mantle-boundary (CMB) is set to be isothermal at $T_{\mathrm{CMB}} = 4500\,\mathrm{K}$. Since we do not include any interior heat sources, the models are purely basally heated. Since both mass and radius have been determined for this super-Earth we can make an assumption on the thickness of the mantle and the core size assuming an Earth-like composition. To do this, we solve for the internal structure equations, as in Valencia et al. (2007b):

$$\frac{dP}{dr} = -\rho(r)g(r) \tag{3.1a}$$

$$\frac{dm}{dr} = 4\pi r^2 \rho(r) \tag{3.1b}$$

$$\frac{dg}{dr} = 4\pi G\rho(r) - \frac{2Gm(r)}{r^3} \tag{3.1c}$$

Where r is the radius, P the pressure, m the mass, $G = 6.6743 \cdot 10^{-11}\,\mathrm{m^3 kg^{-1} s^{-2}}$ the gravitational constant, g the gravitational acceleration, and ρ the density. We determine the density profile $\rho(P)$ as a function of P using a 3^{rd}-order Birch-Murnaghan equation of state:

$$P(\rho) = \frac{3K_{a0}}{2}\left[\left(\frac{\rho}{\rho_0}\right)^{7/3} - \left(\frac{\rho}{\rho_0}\right)^{5/3}\right]\left\{1 + \frac{3}{4}(K'_{a0} - 4)\left[\left(\frac{\rho}{\rho_0}\right)^{2/3} - 1\right]\right\} \tag{3.2}$$

Where K_{a0} is the adiabatic bulk modulus at $P = 0$ and $K'_{a0} = (\frac{\partial K}{\partial P})_S$ the pressure derivative of the adiabatic bulk modulus at $P = 0$.

Mineralogy	K_{a0} (GPa)	K'_{a0}	ρ_s (kg/m^3)
upper mantle (olivine)	163	4.0	3240
transition zone	85	4.0	3226
bridgmanite	210	3.9	3870
post-perovskite	210	3.9	3906
(outer) core	201	4.0	7050

Table 3.1 | Birch-Murnaghan parameters for reference density profiles. The values for the mantle are from (Tackley et al., 2013) and the values for the outer core from (Zeng and Sasselov, 2014). ρ_s corresponds to the (extrapolated) density at the surface ($P = 0$).

These equations are then solved iteratively to find a solution that agrees with the total mass of the planet from observations. This leads to a radius of the core mantle boundary of approximately $r_{\text{cmb}} = 4900\,\text{km}$ and a mantle depth of $d_{\text{mantle}} = 3380\,\text{km}$. The surface gravitational acceleration is $g = 16.4\,\text{ms}^{-2}$ (assumed constant throughout the mantle).

We model the mantle convection of Gliese 486b using the code StagYY (Tackley, 2008) in a two-dimensional (2D) spherical annulus geometry (Hernlund and Tackley, 2008). As it is usually done for Earth-like models, the infinite Prandtl number approximation is made (i.e. inertial forces are neglected). Compressibility is assumed by employing the truncated anelastic liquid approximation (TALA) where a reference state density profile is prescribed that varies with depth. Material properties, such as thermal expansivity α and thermal conductivity k also depend on pressure (Fig. 3.1).

All models have a resolution of 256 cells in the angular direction and 128 cells in the radial direction. The initial temperature field has thermal boundary layers at the surface and CMB of thickness $d_{\text{TBL}} = 260\,\text{km}$ with a potential temperature of 2000 K and we also include random Gaussian noise with an amplitude of 100 K. Viscosity depends on pressure and temperature and is determined using an Arrhenius-like law:

$$\eta(P,T) = \eta_0 \exp\left(\frac{E_a + PV_a(P)}{RT} - \frac{E_a}{RT_0}\right) \tag{3.3}$$

Where η_0 is a reference viscosity, E_a is the activation energy, $V_a(P)$ is the activation

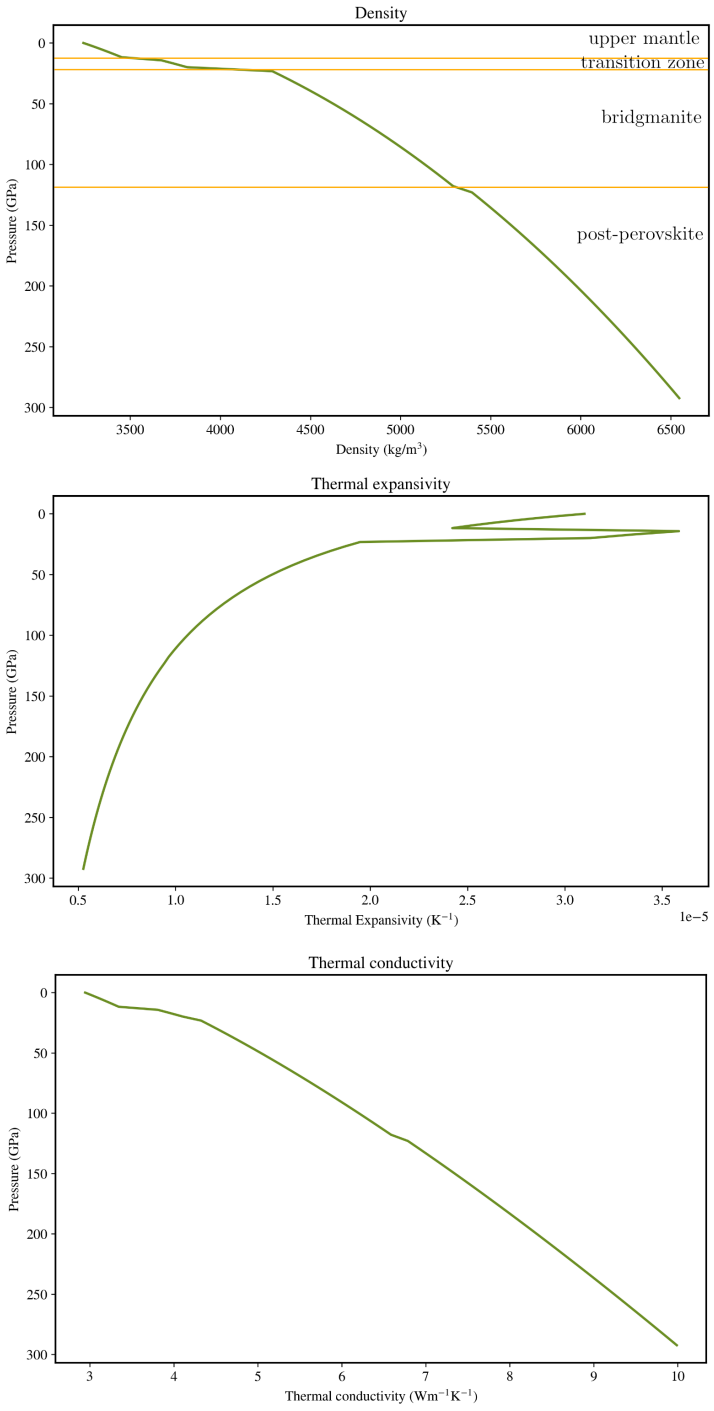

Figure 3.1 | Reference profiles for density ρ, thermal expansivity α and thermal conductivity k.

volume, and $R = 8.311\,\mathrm{JK^{-1}mol^{-1}}$ is the universal gas constant. The activation volume depends on pressure and is given by:

$$V_a(P) = V_0 \exp\left(-\frac{P}{P_{\text{decay}}}\right) \tag{3.4}$$

Where P_{decay} is the decay pressure controlling the pressure dependence of the activation volume.

Table 3.2 shows the parameters used for the viscosity (Tackley et al., 2013). We use a minimum and maximum cutoff for the viscosity of $\eta_{\text{min}} = 10^{18}\,\mathrm{Pa\,s}$ and $\eta_{\text{min}} = 10^{28}\,\mathrm{Pa\,s}$. The mantle is divided into 3 viscosity layers: upper mantle, bridgmanite, and post-perovskite layer (pPv).

Mineralogy	E_a (kJ/mol)	V_0 ($\mathrm{cm^3/mol}$)	P_{decay} (GPa)	η_0 (Pa s)
Upper mantle	300	5.0	∞	10^{21}
Bridgmanite	370	3.65	200	$3.0 \cdot 10^{23}$
Post-perovskite lower bound	162	1.4	1610	$1.9 \cdot 10^{21}$

Table 3.2 | From (Tackley et al., 2013): Parameters used for the Arrhenius-like viscosity law (Eqs. 3.3 and 3.4)

.

We also model the strength of the lithosphere (outermost rigid layer of the planet) through a plastic yielding criterion. At low pressure, this strength is related to its fracture strength of frictional sliding of faults (Byerlee's law (Byerlee, 1978)). At high pressure, the strength is related to ductile failure caused by dislocation motion of the lattice (Kohlstedt et al., 1995). Both the brittle and ductile components are encapsulated within a pressure-dependent yield stress σ_y:

$$\sigma_{\text{y}} = \min(c_f P, \sigma_{\text{duct}} + \sigma'_{\text{duct}} P) \tag{3.5}$$

Where c_f is the friction coefficient and σ'_{duct} is the ductile yield stress gradient. If the stress exceeds the yield stress σ_y, the viscosity gets reduced to an effective viscosity given by:

$$\eta_{\text{eff}} = \frac{\sigma_{\text{y}}}{2\dot{\epsilon_{\text{II}}}} \quad \text{if} \quad 2\eta\epsilon_{\text{II}} > \sigma_y \tag{3.6}$$

Where $\dot{\epsilon_{\text{II}}}$ is the second invariant of the strain rate tensor and η is calculated using Equation 3.3. From laboratory experiments, the strength of the lithosphere is on the

order of several hundred MPa (Kohlstedt et al., 1995), while numerical simulations often use a ductile yield strength smaller than 200 MPa in order to obtain a plate-like style of convection (mobile lid). In this study, we use a Byerlee's friction coefficient $c_f = 1\,\mathrm{MPa}$ (Byerlee, 1978), and the ductile yield strength σ_{duct} is varied from 10 (weak lithosphere) to 300 MPa (strong lithosphere). For the ductile yield stress gradient, we use $\sigma'_{\mathrm{duct}} = 0.01$ in order to avoid yielding of the deep mantle (Tackley et al., 2013).

3.2.1 Surface temperature

We run a suite of models with different surface temperatures that are either calculated using theoretical calculations or from GCMs. The equilibrium temperature of the planet is given by: (Méndez and Rivera-Valentín, 2017)

$$T_{\mathrm{eq}} = T_\star \sqrt{\frac{R_\star}{2d}} \left(\frac{1-A}{\beta\epsilon}\right)^{1/4} \tag{3.7}$$

Where $T_\star$ is the equilibrium temperature of the host star GJ 486a, $R_\star$ its radius, A the bond albedo, d the distance of the planet from the star, and ϵ is the fraction of the planet surface that re-radiates the absorbed flux. $\beta = 1$ if the planet is a fast rotator, $\beta = 0.5$ if the planet is tidally locked and $\beta = 1/4$ for the substellar point of a tidally locked planet. Assuming different efficiencies of heat redistribution in the atmosphere (i.e. different values of β), we determine the dayside and nightside temperatures for the interior modelling runs. The corresponding parameters are shown in Table 3.3. The surface temperature boundary condition is then given by:

$$T(\theta) = \begin{cases} T_{\mathrm{night}} + (T_{\mathrm{day}} - T_{\mathrm{night}})\cos^{1/4}(\theta) & \text{if } \theta \in [-90, 90[\quad \text{(dayside)} \\ T_{\mathrm{night}} & \text{if } \theta \in [90, 270[\quad \text{(nightside)} \end{cases} \tag{3.8}$$

The host star GJ 486a has an equilibrium temperature of $3340 \pm 54\,\mathrm{K}$, which leads to an equilibrium temperature of 700 K for $\beta = 0.5$ and $T_{\mathrm{day}} = 833\,\mathrm{K}$ at the substellar point. Figure 3.2 shows the surface temperatures from the general circulation models (GCMs) for different surface pressures p_s, optical depths τ and mean molecular weights μ. A mean molecular weight of $\mu = 2\,\mathrm{g/mol}$ corresponds to a hydrogen-dominated atmosphere, similar to a volatile-rich primordial atmosphere. A mean

molecular weight of $\mu = 28\,\mathrm{g/mol}$ corresponds to a nitrogen-dominated atmosphere, akin to a secondary atmosphere that could have formed after the planet has lost its primordial atmosphere. From this suite of GCMs, we determined the corresponding dayside and nightside temperatures for the interior models. The corresponding models are shown in Table 3.4. The surface temperature boundary condition is again determined using Equation 3.8.

The corresponding surface temperatures used as a thermal surface boundary condition in the interior models are shown in Figure 3.3. Surface temperatures that have been determined assuming different efficiencies of heat redistribution (using Equation 3.7) are shown with a dashed line. The surface temperatures that have been inferred from GCM simulations are shown with a solid line. For the M_{850}^{1200} and M_{300}^{300} model, we also vary the plastic yield strength σ_{duct} from 50 to 200 MPa. The corresponding model parameters are shown in Tables 3.5 and 3.6.

Model	dayside temp. (K)	nightside temp. (K)	σ_{duct} (MPa)	heat redistribution
M_{10}^{990}-300	990	10	300	tidally locked ($\beta = 1/4$)
M_{350}^{845}-300	845	350	300	average heat redistribution
M_{700}^{700}-300	700	700	300	uniform ($\beta = 1$)
M_{300}^{300}-300	300	300	300	uniform Earth temp.
M_{10}^{990}-10	990	10	10	tidally locked ($\beta = 1/4$)
M_{350}^{845}-10	845	350	10	average heat redistribution
M_{700}^{700}-10	700	700	10	uniform ($\beta = 1$)
M_{300}^{300}-10	300	300	10	uniform Earth temp.

Table 3.3 | Dayside and nightside temperatures for different efficiencies of heat redistribution. M_{10}^{990} and M_{700}^{700} are deduced from Equation 3.7. M_{350}^{845} is an average between M_{10}^{990} and M_{700}^{700}, representing a case with average heat redistribution. M_{300}^{300} corresponds to a model with Earth-like surface temperature.

3.3 Results

3.3.1 Efficiencies of heat redistribution

Here, we present the results for the interior mantle dynamics of Gliese 486b where the surface temperatures have been derived theoretically for different efficiencies of heat redistribution using Equation 3.7. The corresponding temperature profiles are

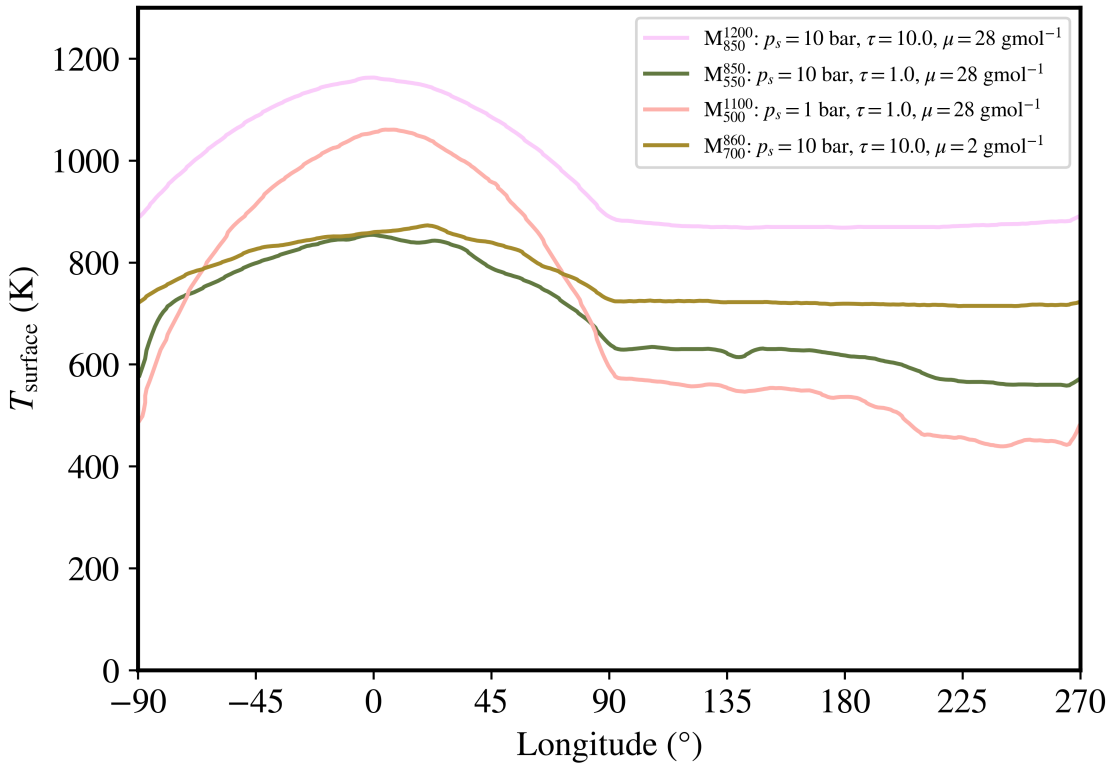

Figure 3.2 | Surface temperatures from general circulation models (GCMs) for different surface pressures p_s, optical depths τ and mean molecular weights μ. The corresponding surface temperatures that are used in the models are shown in Figure 3.3.

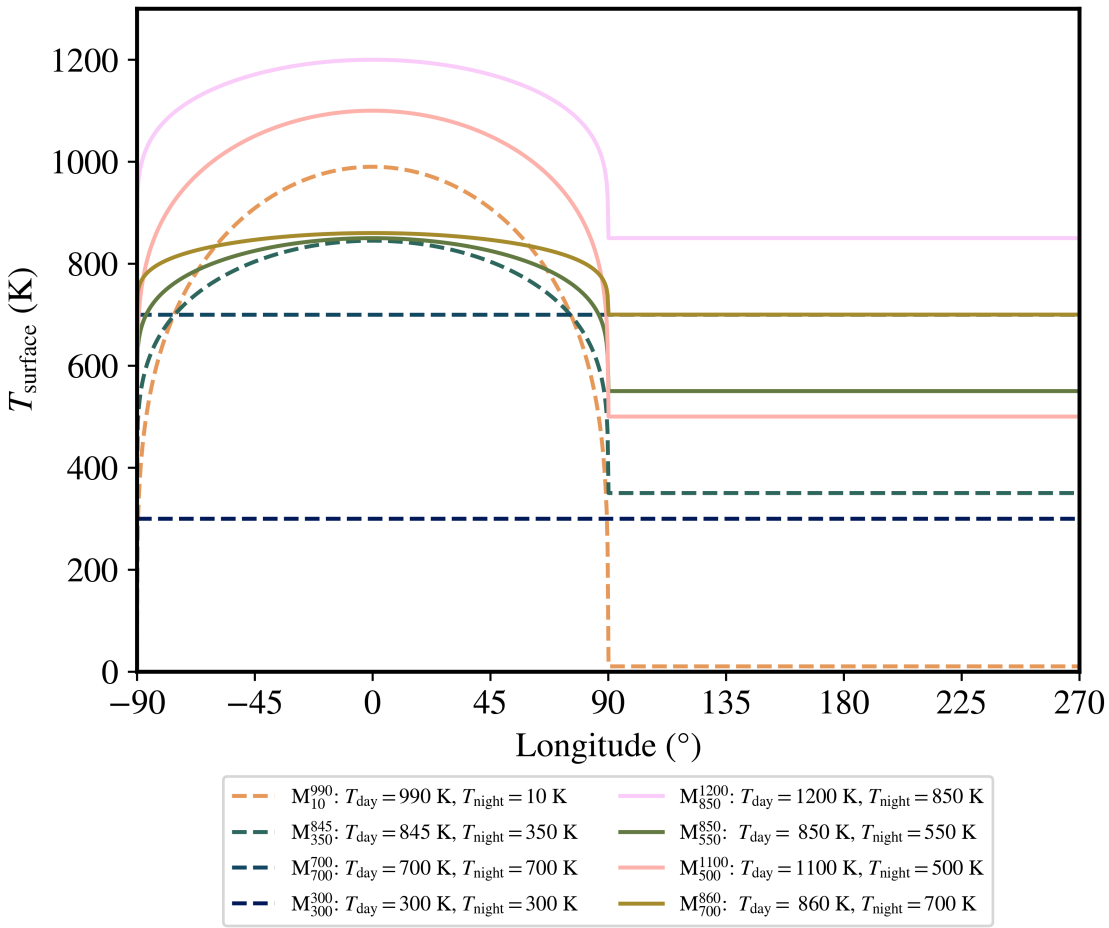

Figure 3.3 | Surface temperatures used for the different model runs. The dashed lines show the models where the temperature contrast has been determined assuming different efficiencies of heat redistribution (Equation 3.7). The solid lines show models where the temperature contrast is inferred from GCM simulations (Figure 3.2).

.

Model	dayside temp. (K)	nightside temp. (K)	σ_{duct} (MPa)	atmospheric parameters p_s (bar)	τ	μ (g/mol)
$M_{850}^{1200}-100$	1200	850	100	10	10.0	28
$M_{550}^{850}-100$	850	550	100	10	1.0	28
$M_{500}^{1100}-100$	1100	500	100	1	1.0	28
$M_{700}^{860}-100$	860	700	100	10	10.0	2
$M_{850}^{1200}-300$	1200	850	300	10	10.0	28
$M_{550}^{850}-300$	850	550	300	1	1.0	28
$M_{500}^{1100}-300$	1100	500	300	1	10.0	28
$M_{700}^{860}-300$	860	700	300	10	10.0	2

Table 3.4 | Dayside and nightside temperatures derived from GCMs with different atmospheric parameters.

Model	dayside temp. (K)	nightside temp. (K)	σ_{duct} (MPa)
$M_{850}^{1200}-25$	1200	850	25
$M_{850}^{1200}-50$	1200	850	50
$M_{850}^{1200}-75$	1200	850	75
$M_{850}^{1200}-125$	1200	850	125
$M_{850}^{1200}-150$	1200	850	150
$M_{850}^{1200}-175$	1200	850	175
$M_{850}^{1200}-200$	1200	850	200
$M_{850}^{1200}-225$	1200	850	225
$M_{850}^{1200}-250$	1200	850	250

Table 3.5 | Parameters for the models where the plastic yielding strength is varied for the M_{850}^{1200} model.

Model	dayside temp. (K)	nightside temp. (K)	σ_{duct} (MPa)
$M_{300}^{300}-25$	300	300	25
$M_{300}^{300}-50$	300	300	50
$M_{300}^{300}-75$	300	300	75
$M_{300}^{300}-125$	300	300	125
$M_{300}^{300}-150$	300	300	150
$M_{300}^{300}-175$	300	300	175
$M_{300}^{300}-200$	300	300	200
$M_{300}^{300}-225$	300	300	225
$M_{300}^{300}-250$	300	300	250

Table 3.6 | Parameters for the models where the plastic yielding strength is varied for the M_{300}^{300} model.

shown in Figure 3.3.

3.3.1.1 Models with low yield stress ($\sigma_{\mathbf{duct}} = 10\,\mathbf{MPa}$)

In this section, we present the results for the models with a low yield stress ($\sigma_{\mathrm{duct}} = 10\,\mathrm{MPa}$) (see Table 3.3). Figure 3.4 shows snapshots of the mantle temperature at 50 Gyrs for the models with a weak lithosphere ($\sigma_{\mathrm{duct}} = 10\,\mathrm{MPa}$) and the corresponding evolutionary tracks of upwellings and downwellings. All models have a uniform distribution of hot upwellings and cold upwellings regardless of the temperature contrast. However, the downwellings are much stronger (i.e. colder and more viscous) for the models with a stronger temperature contrast between the dayside and the nightside. As it can be seen from the evolutionary tracks, the location of the upwellings and upwellings is very stable. Downwellings for the M_{10}^{990}-10 are not showing up on the evolutionary track plot because they are too faint compared to the downwellings on the nightside to be detected by the downwelling detection algorithm 1.3.6. One can see from the mantle temperature snapshot that downwellings are still present on the dayside. Figures 3.4(C,D) show the results for a uniform surface temperature of 700 and 300 K respectively. Downwellings and upwellings are both uniformly distributed and there is (as expected) no dichotomy between the dayside and nightside. Both downwellings and upwellings are more stable for the 300 K case because the lower temperature makes the downwellings more viscous and therefore also more sluggish.

3.3.1.2 Models with high yield stress ($\sigma_{\mathbf{duct}} = 300\,\mathbf{MPa}$)

$\mathbf{M}_{10}^{990}$-300: Tidally locked without heat redistribution A strong downwelling forms on the dayside of the planet and upwellings get pushed preferentially towards the nightside (Fig. 3.5A). The nightside is more yielded than the dayside and is very viscous (as it reaches the maximum viscosity allowed by the numerical model). Initially, a downwelling forms closer to the terminator at the nightside, but later breaks away. A downwelling on the nightside is not stable. This is tested with a model that starts with the downwelling on the nightside. In this case, the hemispheric tectonic regime reconfigures the position of the downwellings and upwellings over the span of ≈ 40 Gyrs. After that time, the downwelling is again preferentially on the dayside and upwellings are on the nightside.

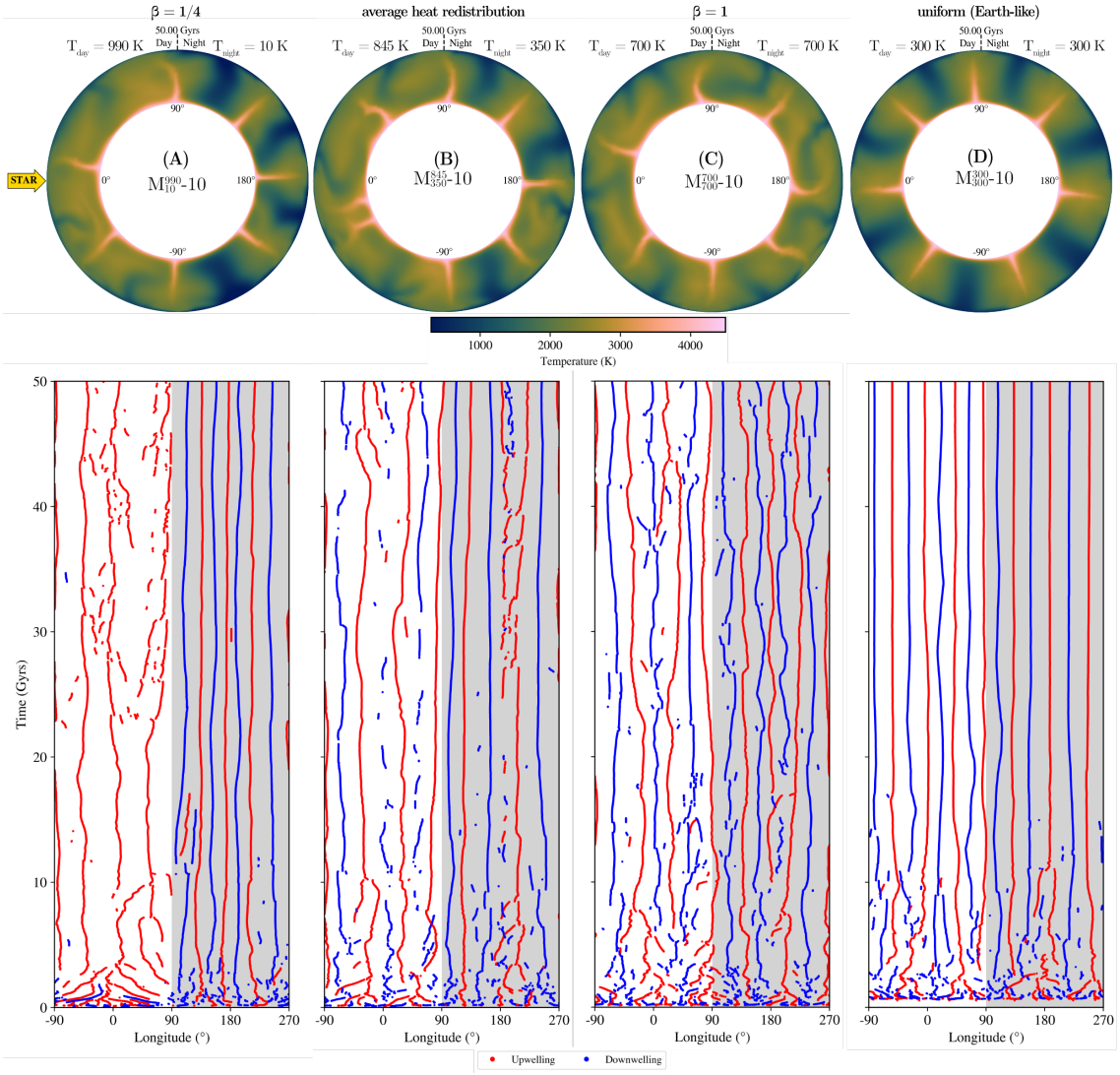

Figure 3.4 | Snapshots of mantle temperature for super-Earth GJ 486b at 50 Gyrs for the models with a weak lithosphere ($\sigma_{\text{duct}} = 10\,\text{MPa}$) (top row) and the corresponding evolutionary tracks of upwellings (red) and downwellings (blue) (bottom row).

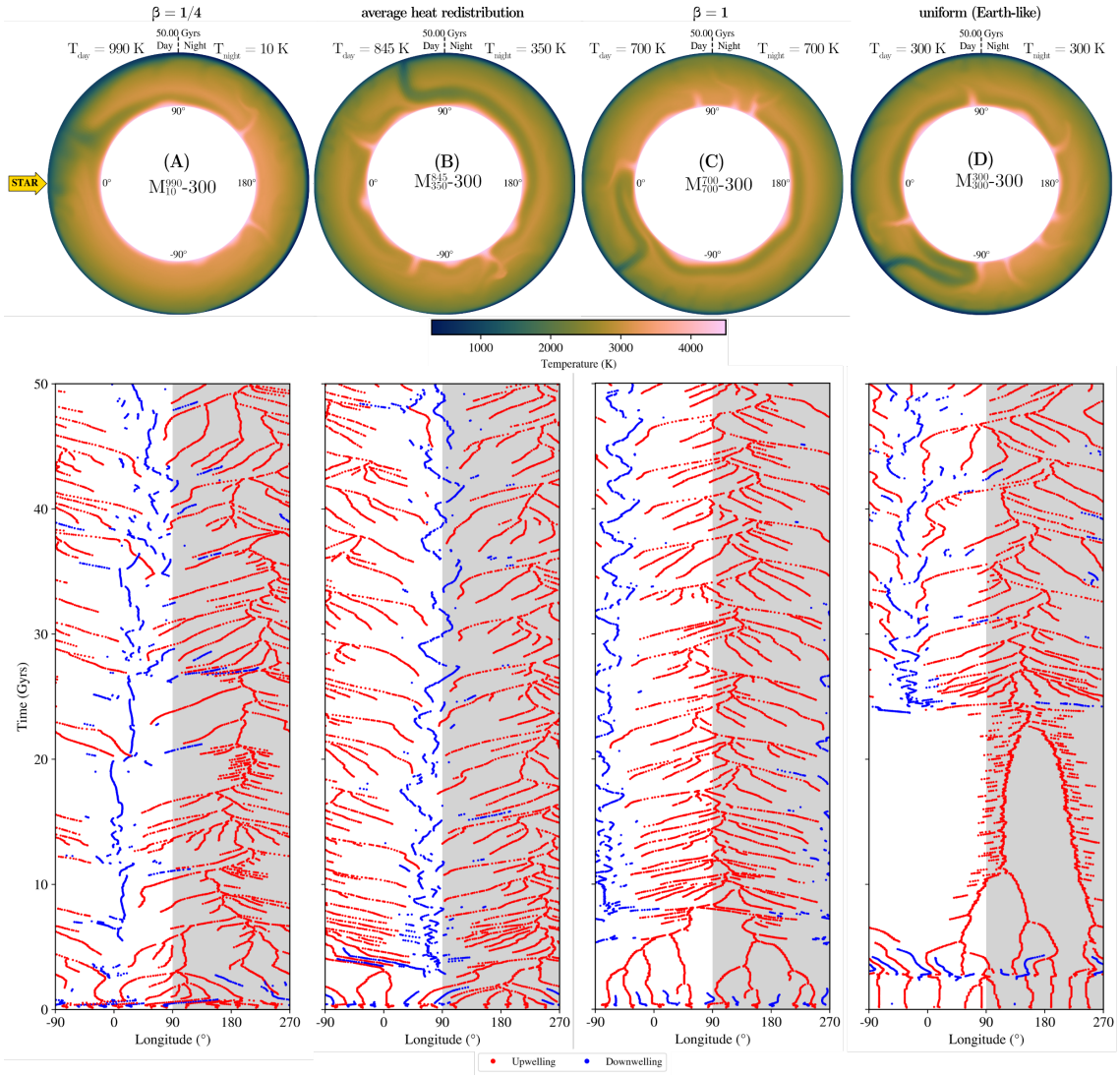

Figure 3.5 | Snapshots of mantle temperature for super-Earth GJ 486b at 50 Gyrs (top row) and the corresponding evolutionary tracks of upwellings (red) and downwellings (blue) for the models with a strong lithosphere ($\sigma_{\rm duct} = 300\,{\rm MPa}$) (bottom row). The surface temperature profiles are derived assuming different efficiencies of heat redistribution.

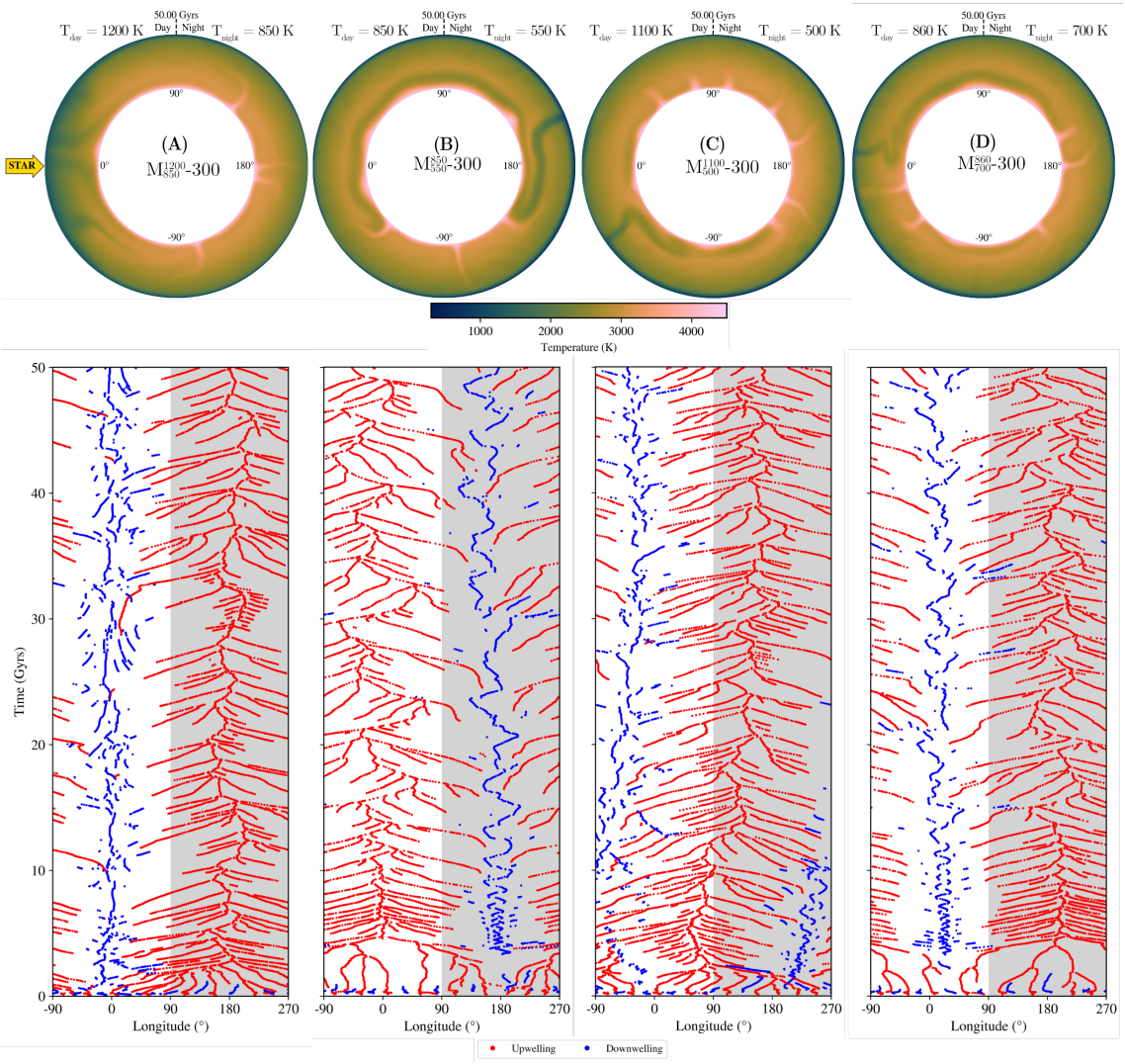

Figure 3.6 | Snapshots of mantle temperature for super-Earth GJ 486b at 50 Gyrs (top row) and the corresponding evolutionary tracks of upwellings (red) and downwellings (blue) for the models with a strong lithosphere ($\sigma_{\text{duct}} = 300\,\text{MPa}$) (bottom row). The surface temperatures are derived from general circulation models.

M_{350}^{845}-300: Average heat redistribution A downwelling forms at the top terminator where it oscillates over time between the dayside and the nightside (Fig. 3.5B). Upwellings are preferentially around the lower terminator. The nightside upper mantle is rather viscous, although the thermal boundary layer is not as thick as for the M_{10}^{990}-300 model. Before the downwelling forms, cold material accumulates around the upper terminator. An upwelling at the substellar point leads to strong deformation and strain at the surface and the upwelling then moves towards the terminator. At the terminator, cold material will then subduct into the deep mantle.

M_{700}^{700}-300: Uniform temperature (fast rotator) This model has no dayside-nightside temperature contrast. The surface temperature is set at 700 K. In this case, the downwelling forms and moves around the terminator (Fig. 3.5C). This configuration is stable. Towards the end of the run, the downwelling has moved approximately 45° towards the anti-stellar point. This configuration rotated by 180° is also a stable configuration, where the downwelling will then move slightly around the top terminator. This therefore corresponds to a degree-1 convection regime.

M_{300}^{300}-300: Uniform Earth-like temperature This is also a model with no dayside-nightside temperature contrast. The temperature is lower than in the other models at 300 K. For a very long time ($\approx$ 22 Gyrs) there are only upwellings (Fig. 3.5D). The upper thermal boundary layer thickens due to cooling, but no downwellings form. At around 22 Gyrs, a plume impinges on the nightside. This leads to thermally induced weakening of the lithosphere resulting in two plates moving towards the dayside where they will collide with each other. This provides enough stress to cause yielding and promote a downwelling on the dayside. The downwelling is able to continuously drain the cold thermal boundary layer and a degree-1 convection pattern is established. The rotated model for this case shows that the convection pattern with a downwelling on the nightside is also a stable pattern. Therefore, this regime does not correspond to a hemispheric tectonic regime.

3.3.2 Results using GCM models

In this section, we present the results for the interior models of GJ 486b where the surface temperatures have been derived using general circulation models. The corresponding temperature profiles are shown in Figure 3.3.

3.3.2.1 Models with high yield stress ($\sigma_{\mathbf{duct}} = 300\,\mathbf{MPa}$)

M^{1200}_{850}-300: Thick atmosphere with large optical depth (high μ) This model is similar to M^{990}_{10}-300: A strong downwelling forms on the dayside and upwellings are getting pushed towards the nightside. A return flow of cold material from the nightside towards the dayside replenishes the cold thermal boundary layer on the dayside before it accumulates enough buoyancy and breaks away (Fig. 3.5A). This return flow of cold material is accommodated in the upper mantle.

M^{850}_{550}-300: Thick atmosphere with small optical depth (high μ) This model is characterised by a strong downwelling on the nightside and upwellings that are getting pushed towards the dayside (3.6B). This is a reversed tectonic regime compared to M^{990}_{10}-300. The return flow in the upper mantle is also reversed: Cold material now flows from the dayside towards the nightside.

M^{1100}_{500}-300: Thin atmosphere with small optical depth (high μ) This model is again characterised by a downwelling on the dayside and upwellings on the nightside. Up to 12 Gyrs, the downwelling is on the nightside (close to the terminator) and slowly moves towards the dayside (3.6C). On the dayside, smaller downwellings are forming occasionally and then merge with the already present strong downwelling over the whole course of the model run.

M^{860}_{700}-300: Thick atmosphere with large optical depth (low μ) The results of this model are very similar to the M^{990}_{10}-300 model. A strong downwelling forms on the dayside and upwellings get pushed towards the nightside. Compared to the M^{990}_{10}-300 model, the cold thermal blanket that occasionally forms on the dayside, is less thick (3.6D). The temperature contrast for this model is quite low and there is also no strong differences in viscosity, strain rate or yielding. In fact, the rotated model (starting with a downwelling on the nightside) is also stable and there is now

a return flow of cold material from the dayside towards the nightside and upwellings get pushed preferentially towards the dayside. Contrary to the rotated M_{10}^{990}-300 model, this model however does not have a preferred direction for the degree-1 convection pattern.

3.3.2.2 Models with medium yield stress ($\sigma_{\mathbf{duct}} = 100\,\mathbf{MPa}$)

Figure 3.7 shows snapshots of the mantle temperature and evolutionary tracks of upwellings and downwellings for the models with a medium yield stress ($\sigma_{\mathrm{duct}} = 100\,\mathrm{MPa}$). Upwellings are uniformly distributed for all cases. For high dayside surface temperatures (models M_{850}^{1200}-100, M_{500}^{1100}-100) , downwellings are thin on the dayside and fade away quickly (Fig. 3.7: A,C). For lower dayside surface temperatures (models M_{550}^{850}-100, M_{700}^{860}-100), downwellings also develop on the dayside and are able to subduct into the deep mantle (Fig. 3.7: B,D). Several cold and viscous downwellings develop on the nightside for all models, but they are less strong as for the models with a low yield stress. As one can see by comparing the evolutionary tracks with the ones for the models with a weak lithosphere (3.4), the downwellings and upwellings are more mobile in the case with $\sigma_{\mathrm{duct}} = 100\,\mathrm{MPa}$. As the downwellings are less viscous, they are not able to lock the plumes in location leading to more time dependence.

3.3.3 Varying the yield stress

Figure 3.8 shows snapshots of the mantle temperature and evolutionary tracks of upwellings and downwellings for the M_{850}^{1200} model for different strengths of the lithosphere. σ_{duct} has been varied from 25 MPa to 250 MPa. For $\sigma_{\mathrm{duct}} \geqslant 150\,\mathrm{MPa}$, a degree-1 convection pattern forms with a strong downwelling preferentially on the dayside and upwellings that are getting pushed towards the nightside. For very low yield stress ($\sigma_{\mathrm{duct}} \leqslant 50\,\mathrm{MPa}$), a uniform convection pattern is established: upwellings and downwellings are distributed uniformly around the mantle with stronger downwellings on the nightside. For medium yield stress ($75\,\mathrm{MPa} \leqslant \sigma_{\mathrm{duct}} \leqslant 125\,\mathrm{MPa}$), the convection pattern is still uniform, and the downwellings become equally strong on both side (i.e., they have weakened on the nightside compared to the models with lower yield stress). The transition regime between a uniform and hemispheric

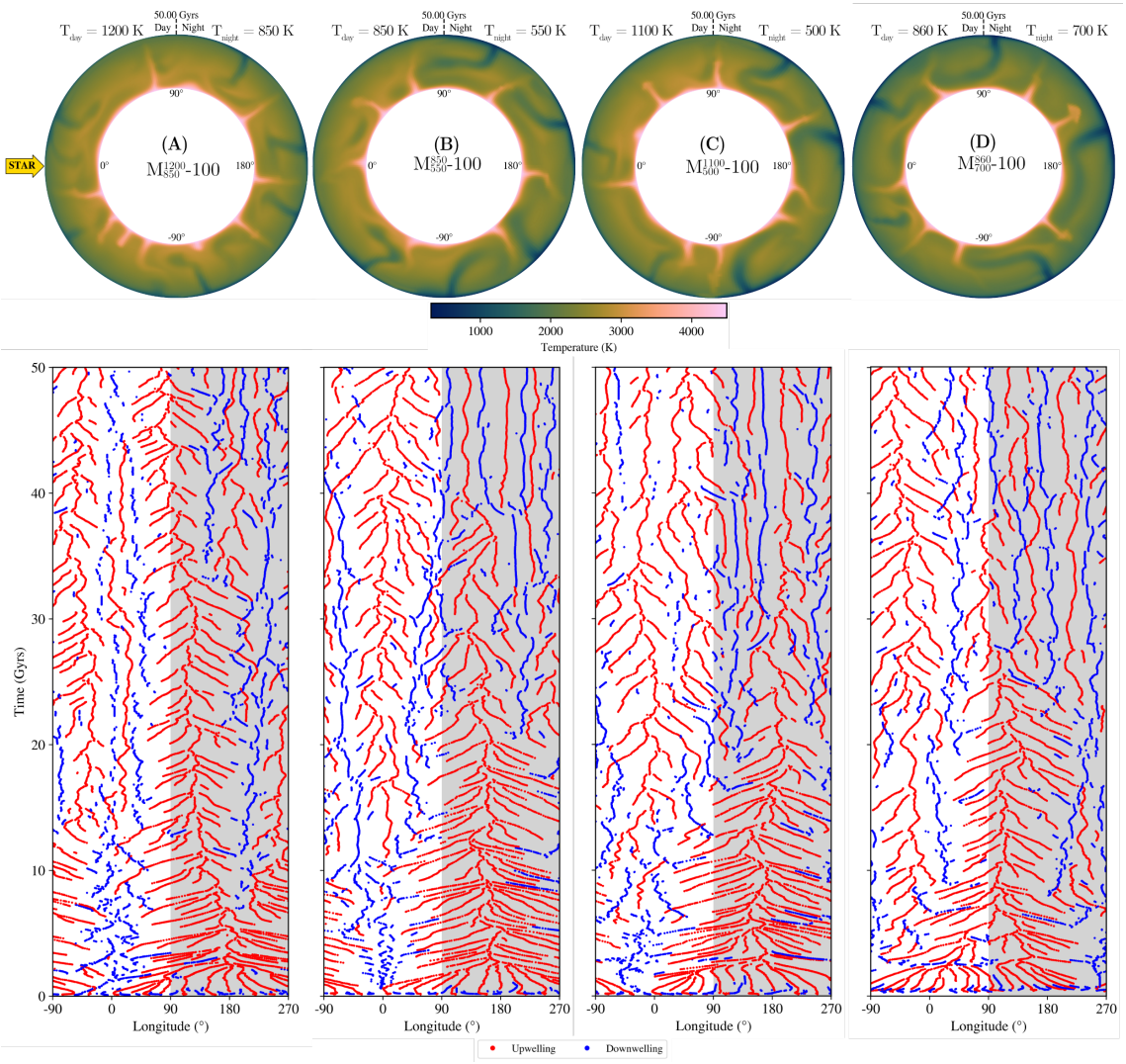

Figure 3.7 | Snapshots of mantle temperature for super-Earth GJ 486b at 50 Gyrs (top row) and the corresponding evolutionary tracks of upwellings (red) and downwellings (blue) for the models with a strong lithosphere ($\sigma_{\text{duct}} = 100\,\text{MPa}$) (bottom row). The surface temperatures are derived from general circulation models.

tectonic regime is occurring between 125 MPa $\leqslant \sigma_{\rm duct} \leqslant$ 150 MPa. In this regime, downwellings are preferentially on the dayside and they do not develop anymore on the nightside. Upwellings are still uniformly distributed around the CMB and downwellings on the dayside are of smaller scale than in the hemispheric tectonic regime.

Figure 3.9 shows snapshots of the mantle temperature and evolutionary tracks of upwellings and downwellings for the M_{300}^{300} model for different strengths of the lithosphere $\sigma_{\rm duct}$. $\sigma_{\rm duct}$ has been varied from 25 MPa to 250 MPa. For lower yield stresses ($\sigma_{\rm duct} \leqslant 125$ MPa), upwellings and downwellings are uniformly distributed. The downwellings are strongest for the models with very low yield stress and become fainter with increasing yield stress. A degree-1 convection pattern establishes for $\sigma_{\rm duct} \geqslant 250$ MPa (the model with $\sigma_{\rm duct} = 300$ MPa is shown in Fig. 3.5D). The transition between a uniform convection pattern and a degree-1 convection pattern happens between 150 MPa $\leqslant \sigma_{\rm duct} \leqslant$ 225 MPa. Model M_{300}^{300}-200 has a degree-1 convection pattern after 50 Gyrs, but it is degree-2 (two strong downwellings, one at the substellar and one at the anti-substellar point) for most of the model run (Fig. 3.9H). One can also see that with increasing yield stress, it takes longer for downwellings to develop. For a very low yield stress, downwellings develop almost instantly whereas for a higher yield stress the cold upper thermal boundary layer first needs to build up before downwellings develop. Therefore, the mantle is first dominated by hot upwellings rising from the CMB towards the surface.

3.4 Discussion

3.4.1 Degree-1 convection and Hemispheric tectonics

GJ 486b has the same radius within errobars as LHS 3844b ($1.3 R_\oplus$), for which we found that hemispheric tectonics are possible for high yield stresses (Meier et al., 2021). Here, we define a hemispheric tectonic regime as a degree-1 pattern of convection where the downwelling is preferentially pinned on one hemisphere and upwellings then are getting pushed towards the other side.

Our models for LHS 3844b assumed an Earth-like core-to-radius ratio (≈ 0.55), whereas for GJ 486 we use a core-to-radius ratio of 0.59, which we determined by

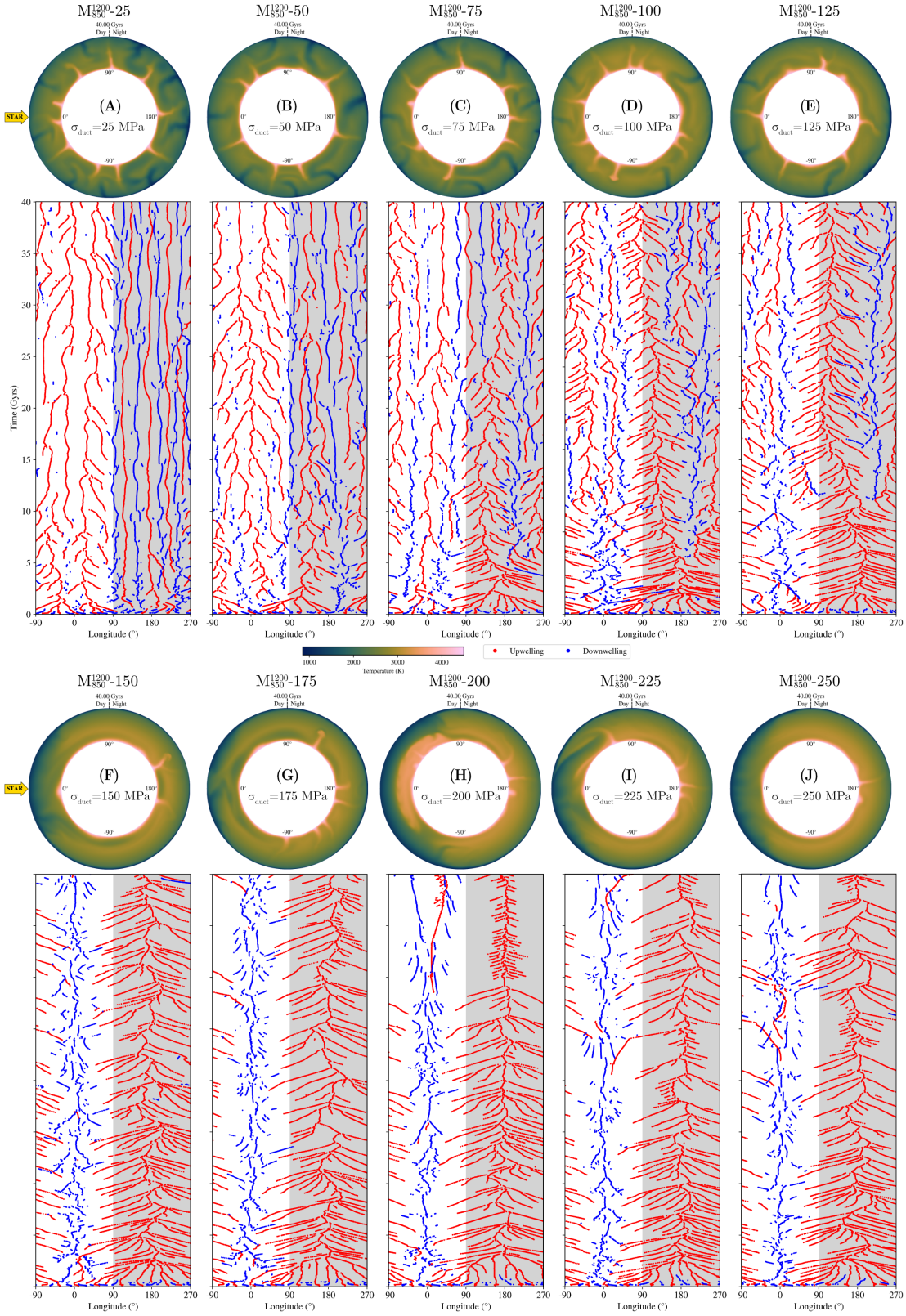

Figure 3.8 | Snapshots of mantle temperature (top panels) and the corresponding evolutionary tracks of upwellings (red) and downwellings (blue) (lower panels) for the M_{850}^{1200} models for different strengths of the lithosphere (σ_{duct}).

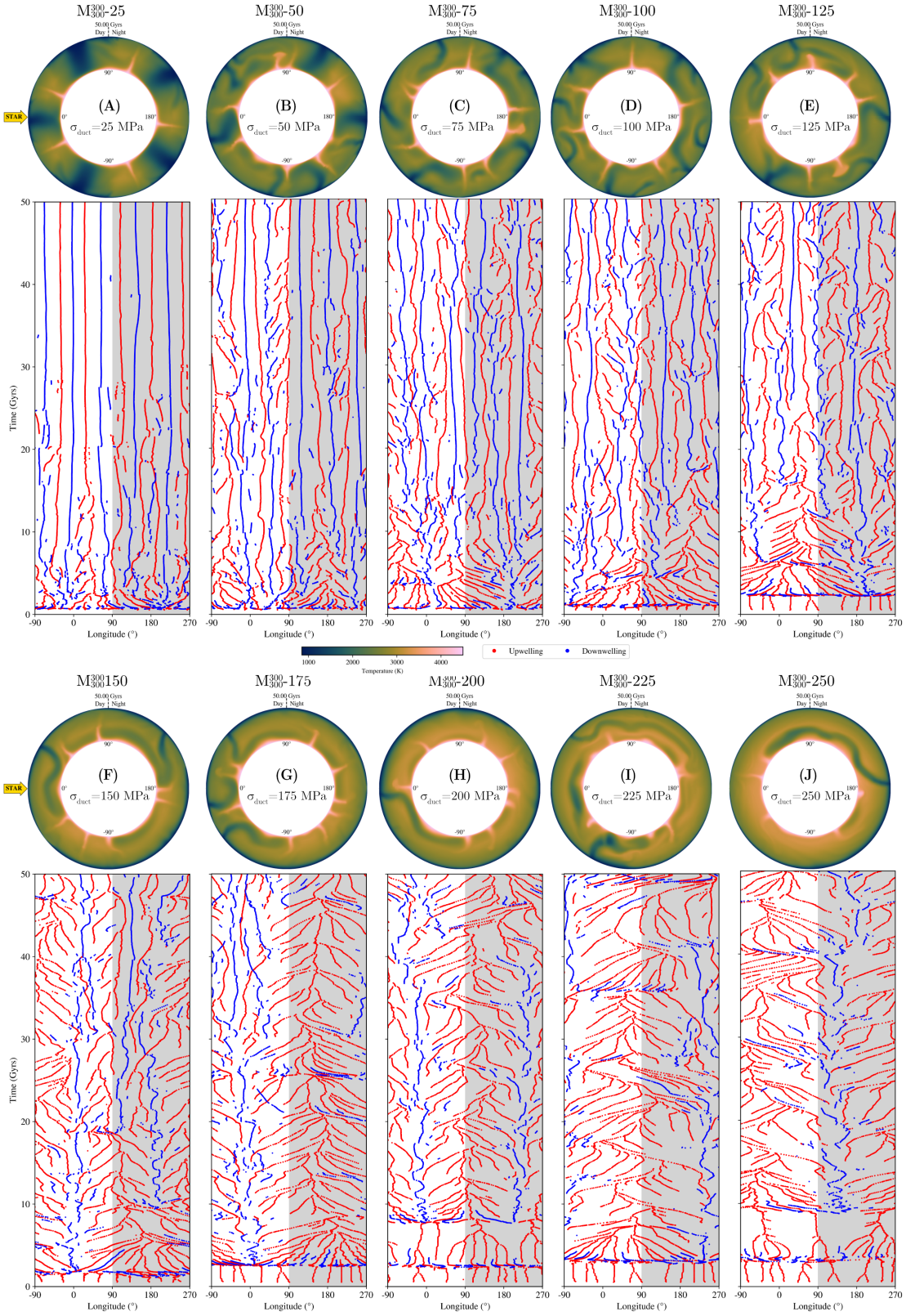

Figure 3.9 | Snapshots of mantle temperature (top panels) and evolutionary tracks of upwellings (red) and downwellings (blue) (lower panels) for the M_{300}^{300} models for different strengths of the lithosphere ($\sigma_{\rm duct}$).

solving the internal structure equations (Section 3.2). A smaller core size could make a degree-one convection pattern more likely (Zhong et al., 2000). Similarly, including internal heating would likely increase the likelihood for degree-1 convection (McNamara and Zhong, 2005). Temperature- and pressure-dependence of viscosity will also cause long-wavelength structures of convection (Yoshida and Kageyama, 2006) or if the mantle viscosity is stratified with a weak asthenosphere (Zhong and Zuber, 2001). For LHS 3844b, we have found that including internal heating pushes the models with lower yield stress into a hemispheric tectonic regime, while the pattern of flow is steady and uniform if no internal heating is included (Meier et al., 2021). The models of GJ 486b with a weak lithosphere have a similar convection pattern as we found for LHS 3844b, which is a uniform distribution of upwellings and downwellings. Here, we find that increasing the ductile yield stress (strength of the lithosphere) increases the wavelength of mantle flow. A degree-one convection pattern establishes for all models of GJ 486b with high yield stress (Figs. 3.8 & 3.9), regardless of the temperature contrast between the dayside and nightside. This is most likely due to a stronger viscosity contrast across the top thermal boundary layer for larger yield stresses. In that case, the boundary layer has more time to grow, which increases the viscosity contrast through temperature and pressure dependence. If the yield stress is low, smaller stresses are needed to yield the lithosphere creating an almost iso-viscous layer (where η_{eff} is given by Equation 3.6. This creates a steady state with downwellings und upwellings that are almost immobile (Fig. 3.9A). By increasing the yield stress, the model becomes less steady as the increasing yield stress adds more non-linearity to the model and therefore also increases the time-dependence. This raises the question whether the hemispheric tectonic regimes that are observed for some models are actual hemispheric tectonic regimes or if the downwelling just coincidentally formed on the dayside. In the next section, we address this question and discuss how a strong temperature contrast between the dayside and nightside can pin the downwelling to the nightside leading to a hemispheric tectonic regime.

3.4.2 Stability of convection pattern

The models with a strong lithosphere ($\sigma_{\rm duct} = 300\,$MPa) all show a degree-1 convection pattern or even hemispheric tectonics (Figs. 3.5 and 3.6). In a hemispheric tectonics regime, the strong downwelling is preferentially on one hemisphere and upwellings are getting pushed towards the other side, whereas in a degree-1 convection regime the downwellings and upwellings do not have a preferred location. Model M_{10}^{1100} shows a similar hemispheric tectonic regime as for the strong lithosphere case of LHS 3844b (Meier et al., 2021), which is a $1.3R_\oplus$ super-Earth that supposedly does not have an atmosphere (Kreidberg et al., 2019). Since both planets have the same radius within errobars, we therefore expect that the tectonic regime of GJ 486b with no atmosphere is similar to that of LHS 3844b. For LHS 3844b with a strong lithosphere, we found that the strong surface temperature contrast can lead to hemispheric tectonics with a downwelling preferentially on the dayside and upwellings that are getting pushed towards the nightside. Here, we find that a degree-1 convection pattern establishes also for more moderate temperature contrasts or even no temperature contrast between the dayside and nightside at all (M_{300}^{300}-300, M_{700}^{700}-300, Fig. 3.5: C, D). This indicates that the degree-1 convection pattern is a consequence of rheology–particularly the strength of the lithosphere—rather than the temperature contrast between the dayside and nightside.

In order to analyse the effect of the surface temperature contrast, we run 'perturbed' models that using an initial state that corresponds to the 180°-rotated state where a degree-1 convection pattern has already been established. Figures 3.10 and 3.11 show the results for these perturbed models for the case where the surface temperatures have been derived from assuming heat redistribution efficiencies and from GCM models, respectively. The model with the strongest temperature contrast and the coolest nightside (M_{10}^{990}) is stable against this perturbation: After approximately 20 Gyrs, the downwelling will again be preferentially on the dayside (Fig. 3.10A). The convection regime of this model is therefore hemispheric tectonics, and not only a degree-1 convection pattern where the downwelling would be stable at any position.

The other models where the surface temperature is derived from different heat redistribution efficiencies (M_{300}^{845}, M_{700}^{700}, and M_{300}^{300}) are not stable against the pertur-

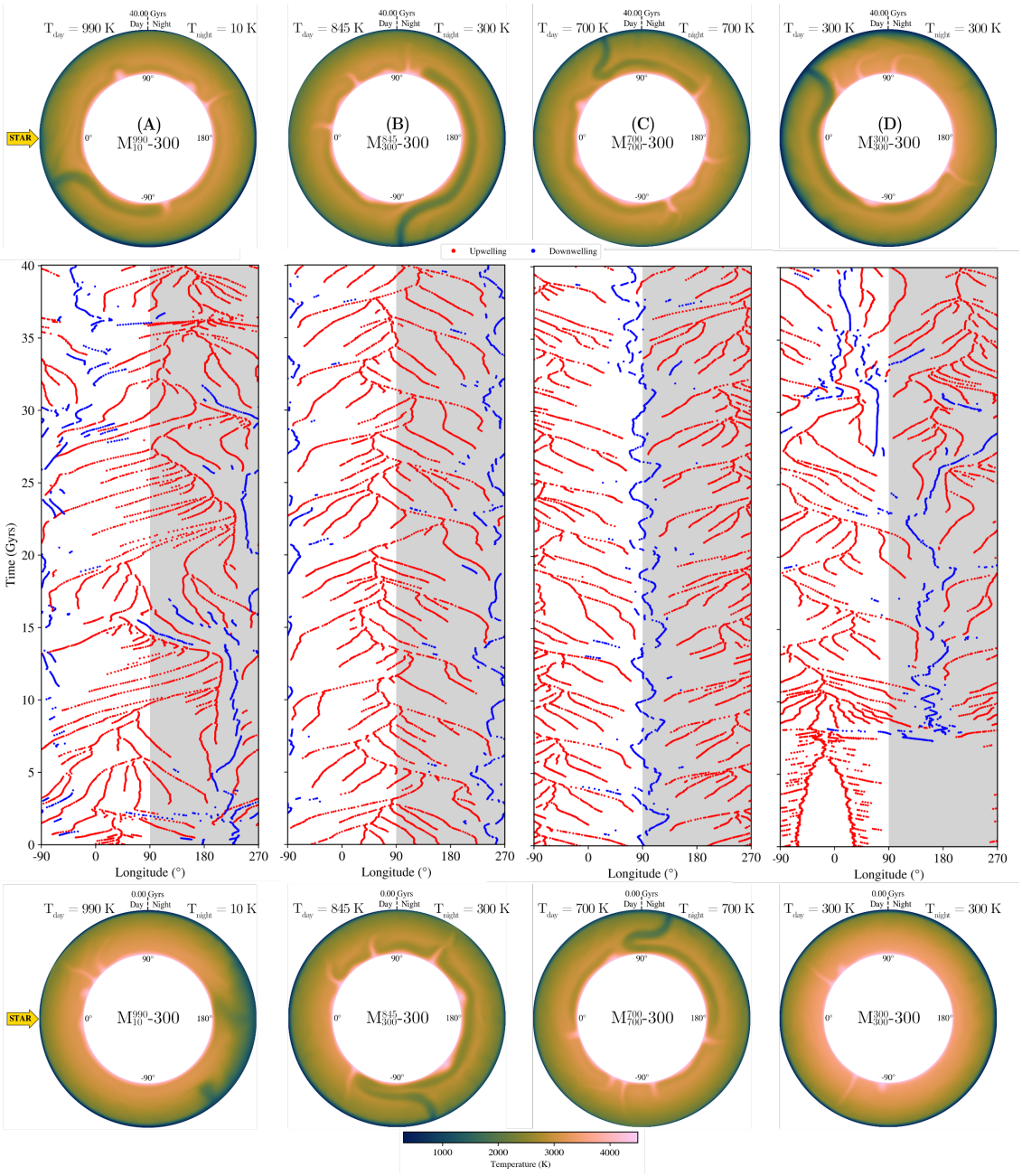

Figure 3.10 | Snapshots of mantle temperature for super-Earth GJ 486b at 0 (bottom row) and 40 Gyrs (top row) and the corresponding evolutionary tracks of upwellings (red) and downwellings (blue) (middle row) for the models with a strong lithosphere ($\sigma_{\text{duct}} = 300\,\text{MPa}$), and where the surface temperature profiles are derived assuming different efficiencies of heat redistribution. The initial mantle temperature (bottom row) corresponds to the 180°-rotated end-of-run state of the models shown in Fig. 3.5.

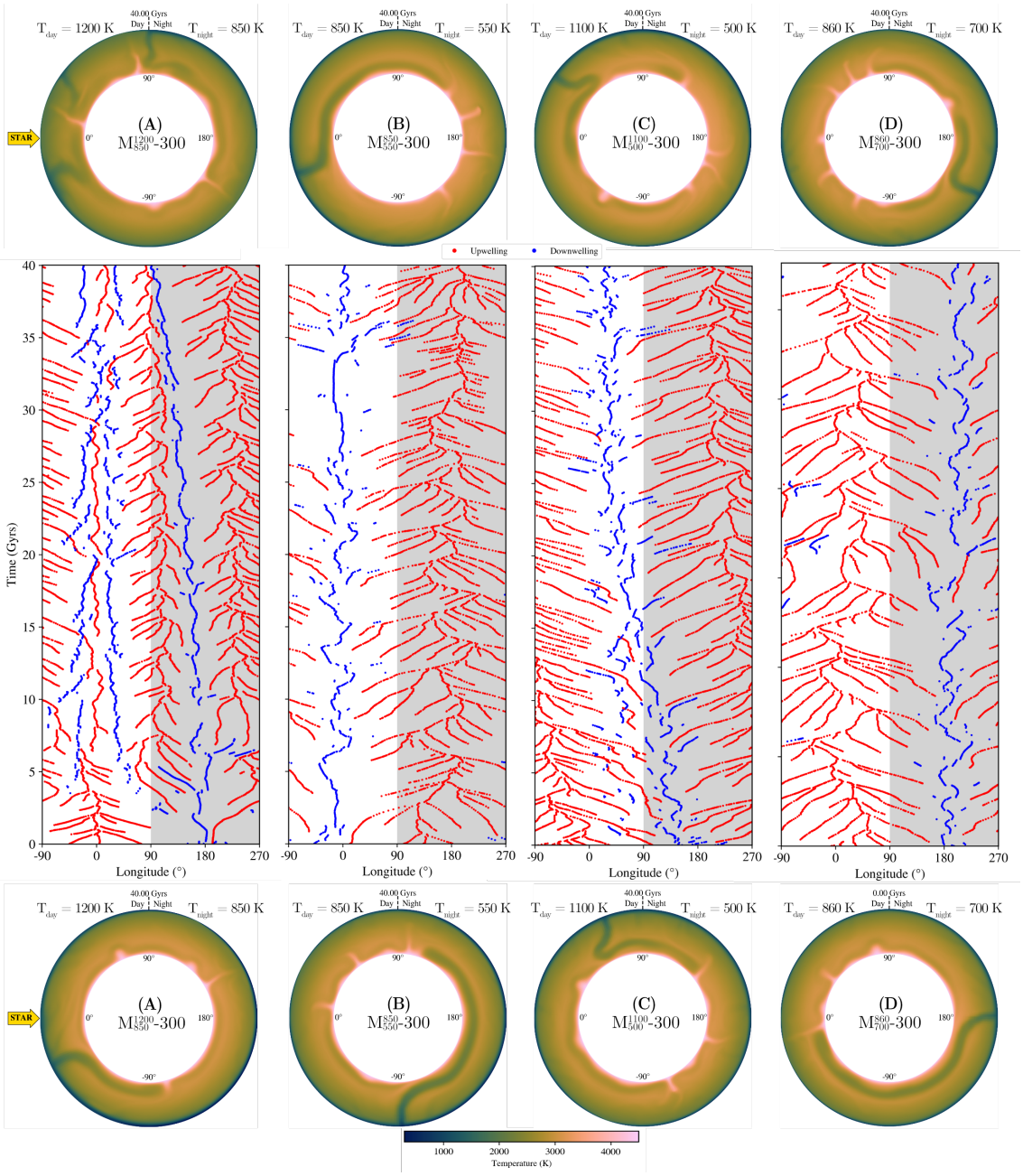

Figure 3.11 | Snapshots of mantle temperature for super-Earth GJ 486b at 0 (bottom row) and 40 Gyrs (top row) and the corresponding evolutionary tracks of upwellings (red) and downwellings (blue) (middle row) for the models with a strong lithosphere ($\sigma_{\text{duct}} = 300\,\text{MPa}$), and where the surface temperature profiles are derived from GCM simulations. The initial mantle temperature (bottom row) corresponds to the 180°-rotated end-of-run state of the models shown in Fig. 3.6.

bation. The downwelling does not move back to the original (unperturbed) location over geological timescales. Therefore, these models develop a degree-1 convection pattern, but not hemispheric tectonics. The downwellings oscillate around their initial states by roughly 45°. Figure 3.11 shows the perturbed models where the surface temperature is derived from GCM simulations. As it can be seen from the evolutionary plots, models M^{850}_{550}-300 and M^{860}_{700}-300 are not stable against the rotation by 180°. The downwellings will remain and oscillate around their perturbed location by roughly 45°. On the other hand, M^{1200}_{850}-300 and M^{1100}_{500}-300 are stable against the perturbation and are therefore in a hemispheric tectonic regime. For the M^{1200}_{850}-300 model, downwellings develop again on the dayside after ≈ 5 Gyrs and the already developed downwelling on the nightside moves back towards the dayside over a very long timescale (≈ 40 Gyrs). For the M^{1100}_{500}-300 model, the already developed downwelling on the nightside has moved back towards the dayside after ≈ 10 Gyrs.

Model	dayside temp. (K)	nightside temp. (K)	tectonic regime
M^{990}_{10}-300	990	10	hemispheric
M^{845}_{350}-300	845	350	degree-1
M^{700}_{700}-300	700	700	degree-1
M^{300}_{300}-300	300	300	degree-1
$M^{1200}_{850}-300$	1200	850	hemispheric
$M^{850}_{550}-300$	850	550	degree-1
$M^{1100}_{500}-300$	1100	500	hemispheric
$M^{860}_{700}-300$	860	700	degree-1

Table 3.7 | Overview of the tectonic regimes for the models with a strong lithosphere. If the tectonic regime is *hemispheric*, this indicates that downwellings move back towards their unperturbed position. If the tectonic regime is *degree-1*, the downwelling will also be stable at the perturbed position. This indicates a degree-1 convection pattern, where the downwellings and upwellings do not have a preferred location.

Table 3.7 shows an overview of the different perturbed models and whether their tectonic regime is hemispheric tectonics or degree-1 convection. In a hemispheric tectonic regime, the strong downwelling is preferentially pinned on one hemisphere, whereas in degree-1 convection it has no preferred location. Figure 3.12 shows an overview of the tectonic regimes for Gliese 486b for the case of a strong lithosphere. Overall, a strong temperature contrast between the dayside and nightside favours a

hemispheric tectonic regime. Also, the dayside temperature needs to be sufficiently hot for hemispheric tectonics, as it can be seen from model M_{300}^{845}, which has a rather strong temperature contrast but does not develop hemispheric tectonics. Point A in Figure 3.12 has been defined assuming that hemispheric tectonics requires a minimum temperature contrast of $\approx$ 200 K. For LHS 3844b, we have also run models with nightside temperatures of $T_{\rm night}$ = 355 K and 710 K. Even though at the time of that study, we concluded that hemispheric tectonics persists even for hotter nightside temperatures, it seems now more apparent that the model with $T_{\rm night}$ = 710 K (with basal heating) actually exhibits a degree-1 convection pattern, and not actual hemispheric tectonics 2.3(B). This in-depth study of the tectonic regimes of GJ 486b has therefore enabled us to adjust our interpretation of the tectonic regimes of super-Earth LHS 3844b. However, perturbed models, and longer run-times will be necessary in order to make a conclusion about the stability of LHS 3844b's convection regimes.

The model with $T_{\rm night}$ = 355 K is rather stable as downwellings that move towards the dayside are disappearing quickly again (see Fig. 2.3(A)), but it is difficult to say whether this regime is actually hemispheric tectonics without running a perturbed model. We estimate the location of Point B in Figure 3.12 by assuming that the LHS 3844b model with $T_{\rm night}$ = 355 K and $T_{\rm day}$ = 1000 K lies at the boundary between hemispheric tectonics and degree-1 convection. However, more model runs are necessary to define this transition from degree-1 convection to hemispheric tectonics. We can assume, however, that planets with a very small temperature contrast do not exhibit hemispheric tectonics and that this likelihood increases for planets with a very strong temperature contrast even if the dayside temperature is not very hot.

3.4.3 Observations

GJ 486b is a suitable target for future emission and transit spectroscopy and phase curve observations (Trifonov et al., 2021). Transit and thermal emission spectroscopy could be used to investigate whether Gliese 486b has a potential atmosphere and give insights into its chemical composition and thickness (Morley et al., 2017). Transit spectroscopy is probing the day-night terminator region of an atmo-

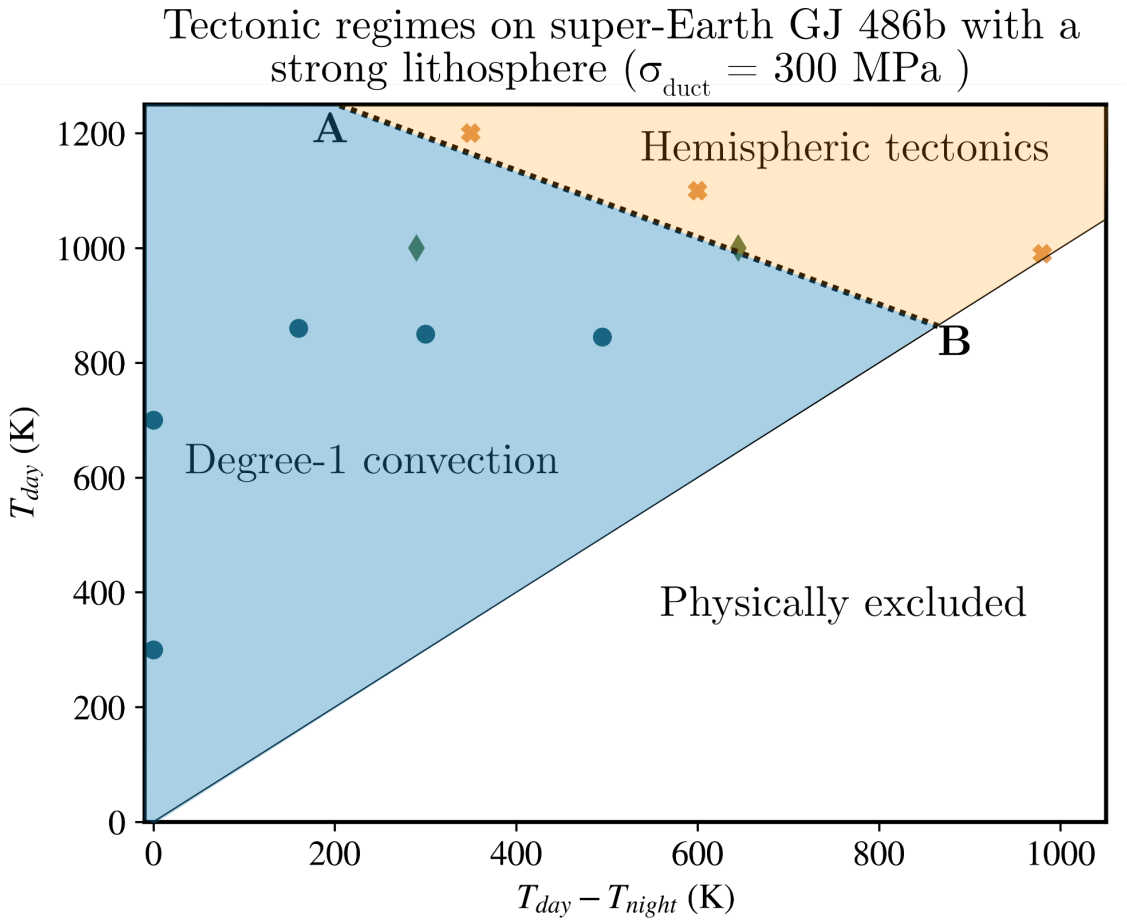

Figure 3.12 | Overview of the tectonic regimes for the models with a strong lithosphere. An increased temperature contrast between the dayside and nightside as well as an increased (dayside) temperature increases the likelihood of hemispheric tectonics (orange shaded region). For lower temperature contrasts and lower dayside temperatures, the mantle is in a degree-1 convection regime with no preferred location for upwellings and downwellings (blue shaded region). The diamond markers indicate models from our study on LHS 3844b. The choice for the points A and B is explained in Section 3.4.2. More model runs are necessary to determine where the transition from degree-1 convection to hemispheric tectonics is. The white region is excluded as this would result in negative temperature on the nightside.

sphere (e.g., Kreidberg, 2018). Some of our models show an asymmetry between the north and south terminator with a downwelling moving around one terminator and upwellings getting pushed towards the other hemisphere. These models are in a degree-one convection regime but do not exhibit hemispheric tectonics as the temperature contrast is not moving downwellings and upwellings towards a preferred location. If upwellings have a preferred location (e.g., nightside or terminators) that is stable over geological timescales, this could lead to preferential melt generation and outgassing at that location (Black and Gibson, 2019).

Transit spectroscopy usually assumes that the terminator region is homogeneous. Space missions, such as JWST or TESS could probe for asymmetries between the morning and evening terminators (Espinoza and Jones, 2021). A north-south asymmetry would be more difficult to detect as the star light will pass through the northern and southern atmosphere almost instantaneously if the planet's orbital plane is not strongly inclined. North-south or morning-evening asymmetries arise due to the 3D nature of the planet. Therefore, it would also be necessary to run 3D interior dynamic models in order to investigate whether degree-one convection or hemispheric tectonics persists. In order to find observational evidence for a hemispheric tectonic regime, we would need observations of the atmospheric compositions of both the dayside and nightside or the corresponding surfaces.

Emission spectroscopy probes the dayside temperature structure and chemical composition of a planet's dayside atmosphere (e.g., Madhusudhan, 2019). A reflection spectrum in the mid- to near-infrared can be used to identify different rocky surface types of an exoplanet (Hu et al., 2012). The nightside of a planet remains difficult to probe. Phase resolved emission spectra can give insights into the thermal structure of an exoplanet's atmosphere (e.g., Stevenson et al., 2014). Emission from a planet's nightside can usually be neglected at visible wavelengths, but could contribute to planet's transit depth at infrared wavelengths (Kipping and Tinetti, 2010). For super-Earth LHS 3844b, we found that the contribution to the thermal phase curve from the interior flux alone would produce temperature differences on the nightside on the order of 15–30 K, which is significantly below the detection capabilities of current and near-future observations (Meier et al., 2021). The same conclusion applies to super-Earth Gliese 486b as the flux from the interior is on the

same order of magnitude. If upwellings on the nightside indeed would lead to preferential melt generation on the nightside, these could imprint themselves in phase curve observations or attenuate the observed transit depth. In summary, a combination of different observations (i.e., transmission spectroscopy, emission and reflection spectroscopy and thermal phase curve observations) will most likely be necessary to confirm hemispheric tectonics on a tidally locked super-Earth. Hence, consideration of the interior dynamics of rocky exoplanets such as Gliese 486b will feedback into determining the requirements of future observational facilities and missions.

3.5 Conclusions

In this study, we investigated the different tectonic regimes of super-Earth GJ 486b using 2D numerical mantle convection models. We constrained the surface temperature contrasts assuming different heat efficiencies of heat circulation and from general circulation models. We investigated how the interior mantle flow is affected by the corresponding surface temperature contrasts and how it depends on the strength of the lithosphere, which we modelled through employing a plastic yielding criterion.

Models with a low yield stress ($\sigma_{\text{duct}} = 10\,\text{MPa}$) develop a mobile tectonic regime with downwellings and upwellings uniformly distributed around the mantle. Downwellings are colder and more viscous on the nightside if the nightside is much cooler than the dayside. These regimes are similar to the tectonic regimes we found for super-Earth LHS 3844b with a weak lithosphere (Meier et al., 2021). Models with a medium yield stress ($\sigma_{\text{duct}} = 100\,\text{MPa}$) develop a similar convection regime, albeit downwellings and upwellings are more mobile.

For models with a high yield stress ($\sigma_{\text{duct}} = 300\,\text{MPa}$), we find that a degree-1 convection pattern is established, independent of the temperature contrast between the dayside and nightside. An increased temperature contrast or overall higher surface temperature increases the likelihood of hemispheric tectonics, in which the downwelling is preferentially pinned on one hemisphere. The transition from a uniform regime to degree-1 convection occurs around $\sigma_{\text{duct}} = 125$–$200\,\text{MPa}$ depending on the surface temperature contrast.

A suite of different observational techniques will be necessary in order to distin-

guish the different convection patterns that we find from our simulations. Similar to what we found for LHS 3844b, the heat contribution from the interior will most likely not lead to significant spectral signatures in the thermal phase curve observations that could be detectable by current or near-future space observations. However, if upwellings lead to preferential melt generation and outgassing of volatiles on one hemisphere, this might lead to signatures that could be detected by transmission or emission and reflection spectroscopy.

Chapter 4

Interior dynamics of super-Earth 55 Cancri e

This chapter is under preparation and is to be submitted as Meier, T.G., Bower, D.J., Lichtenberg, T., Hammond, M., and Tackley, P. J. (2022), Interior dynamics of super-Earth 55 Cancri e.

Abstract

In this study, we investigate the tectonic regimes of the tidally locked lava world 55 Cancri e. This super-Earth has a radius of 1.8 Earth radii and the thermal phase curve observations suggest a strong contrast between the dayside ($T_{\mathrm{day}} = 2700\,\mathrm{K}$) and nightside ($T_{\mathrm{night}} = 1400\,\mathrm{K}$) with the hottest point significantly shifted from the substellar point towards the east, indicating some degree of heat circulation. The dayside (and potentially even the nightside) is hot enough to harbour a magma ocean. Here, we model the interior mantle flow of this planet and investigate how the convection regimes are affected by different temperature contrasts between the dayside and nightside. We use results from general circulation models (GCMs) of atmospheres to constrain the surface temperature contrasts. We find that large super-plumes form on the dayside if that hemisphere is covered by a magma ocean and the nightside remains solid or only partially molten. In that case, cold material will passively move into the deep interior on the nightside. If both the dayside and nightside are fully molten, the magma ocean will equilibrate temperatures at

the interface with the underlying solid mantle and plumes do not have a preferred location anymore. A tectonic regime where the upwelling is preferentially on the dayside might lead to preferential outgassing on that hemisphere which could lead to the build-up of atmospheric species that could be chemically distinct from the nightside.

4.1 Introduction

Here, we focus on the (likely) tidally locked super-Earth 55 Cancri e (McArthur et al., 2004). 55 Cancri e has a radius of around 1.8 Earth radii and its thermal phase curve indicates a nightside temperature around 1400 K with a significant shift of the hottest point (2700 K) located 41 ± 12 degrees east from the substellar point (Demory et al., 2016a) indicating atmospheric circulation. Hammond and Pierrehumbert (2017) have run general circulation models (GCMs) for different types of atmospheres. Their best-fitting model consists of an atmosphere with a 90%-10% mixture of H_2 and N_2 with a mean-molecular weight $\mu = 4.6\,\mathrm{gmol}^{-1}$, optical depth $\tau = 4.0$, and surface pressure $p_s = 5\,\mathrm{bar}$, which produces a significant hot spot and temperature contrast, albeit as not as large as the observed ones. Because of the high solar irradiation, the planet is most likely covered by a magma ocean, placing it into the category of lava planets (Chao et al., 2021). Depending on the amount of heat circulation between the dayside and nightside, a hemispheric magma ocean could form with a molten dayside and a cold, rocky nightside (Léger et al., 2011). Subsequent outgassing of volatiles (e.g., CO_2, H_2O) from a (dayside) magma ocean could then lead to a large outgassed secondary atmosphere (e.g., Bower et al., 2019). This atmosphere could, however, be lost because of the intense radiation from the host star (Valencia et al., 2010). Heavier outgassed elements, such as Na, O_2 or SiO_2 that are outgassed from silicate melts, might be retained and form a thin silicate-vapour atmosphere (Schaefer and Fegley, 2009; Kite et al., 2016). On the nightside, a secondary atmosphere could be built-up through volcanic outgassing from the solid mantle (e.g., Kite and Barnett, 2020; Liggins et al., 2022).

Observations by MOST (Sulis et al., 2019), CHEOPS (Morris et al., 2021), and TESS (Valdés et al., 2022) have shown that 55 Cancri e's occultation depth and

phase curve varies with time, and the source of this variability is not known yet. As of today, 55 Cancri e is one of the only super-Earths where the thermal phase curve has been observed, with the other two being lava world K2-141b (Zieba et al., 2022) and the bare rock super-Earth LHS 3844b (Kreidberg et al., 2019). Thermal phase curve observations of super-Earth 55 Cancri e allow us to constrain the surface temperature but the dynamic and chemical state of its interior remains unknown. Its mass and radius measurements indicate that the planet's density is mostly consistent with either a dense, rocky planet that has a thick atmosphere or that has only a thin atmosphere with a less dense interior (Jindal et al., 2020). The planet could also have no core at all, with an interior that is enriched in Ca and Al minerals, which could have important consequences for the interior dynamics (Dorn et al., 2018a). Here, we model the interior dynamics of 55 Cancri e constrained by thermal phase curve observations. With the use of GCMs, we infer the type of convection inside the mantle of 55 Cancri e for different surface temperature contrasts. The atmosphere models differ in optical thickness τ and composition. We use the resulting longitudinal temperature profiles as a boundary condition for the surface temperature of our mantle convection models. We also investigate how the type of convection depends on the internal heating rate and the cooling rate of the core.

4.2 Methods

4.2.1 Planetary parameters

55 Cancri e is a super-Earth with a radius of $1.88 \pm 0.03 R_\oplus$ and a mass of $8.0 \pm 0.3 M_\oplus$ (Bourrier et al., 2018). It orbits its host star in less than 18 hours. Therefore, 55 Cancri e is most likely tidally locked, leading to a strong surface temperature contrast between the dayside and the nightside. Its thermal phase curve suggests a dayside temperature of 2700 ± 270 K and a nightside temperature of 1380 ± 400 K (Demory et al., 2016a). This super-Earth therefore most likely harbours a global magma ocean on the dayside, potentially extending towards the nightside. This could lead to global convection regimes that we have not yet captured with our studies on the rocky super-Earths LHS 3844b and GJ 486b, for which the surface temperatures are not high enough to produce global magma oceans. We assume that the core-

to-planet radius ratio is ≈ 0.4 (Crida et al., 2018), which leads to a core radius of $r_c = 5096\,\text{km}$ and a mantle thickness of $d_{\text{mantle}} = 7650\,\text{km}$. The host star 55 Cancri is an old star with an age around 8.6 ± 1 Gyrs (Bourrier et al., 2018). In order to save computation power, we only run the models up to 4.6 Gyrs (age of the Sun) or less in cases where the time step has to be drastically reduced because of high velocities. In most cases, a few billion years of runtime is enough for the model to reach a statistical steady state, regarding the location of plumes and passive downwelling flow.

4.2.2 Convection Models

We model solid mantle convection of super-Earth 55 Cancri e using the code StagYY (Tackley, 2008) in a two-dimensional (2D) spherical annulus (Hernlund and Tackley, 2008) under the infinite Prandtl number approximation (i.e., inertial forces are neglected). Compressibility is assumed by employing the truncated anelastic liquid approximation (TALA) where a reference state density profile is assumed that varies with depth. Material properties, such as thermal expansivity α and thermal conductivity k, also depend on pressure. All models have a resolution of 256 cells in the angular direction and 128 cells in the radial direction. The initial temperature field has a thermal boundary at the CMB of thickness $d_{\text{TBL}} = 160\,\text{km}$ with a potential temperature of 2750 K. We also include random Gaussian noise with an amplitude of 100 K. We run models with 3 different internal heating modes (see also Equation 1.12):

- no internal heating: $H = 0$
- (Present-day) Earth-like internal heating: $H = 5.2 \cdot 10^{-12}\,\text{W/kg}$
- High internal heating: $H = 1.4 \cdot 10^{-11}\,\text{W/kg}$

Where H is the internal heating rate. The Earth-like internal heating rate is estimated from Earth's present-day radiogenic heating power $\approx 20\,\text{TW}$ (Sammon and McDonough, 2022). For the high internal heating case, we use an estimate of Earth's primitive radiogenic heating power ($\approx$ 19–38 TW (Dye, 2012)) multiplied by a factor of 2. For some models, we also include a simple core cooling model. If the core

is allowed to cool, the temperature at the CMB is reduced considering the heat flux at the CMB and assuming the heat capacity of the core of $C_p = 750\,\mathrm{JK^{-1}kg^{-1}}$ (Labrosse, 2014; Gubbins et al., 2003).

4.2.3 Density and Thermal expansion

A third order Birch-Murnaghan equation of state is used to relate density to pressure. We use a 2-component system for olivine (including 3 solid-solid phase transitions) and molten olivine. Table 4.1 shows the parameters used for the density profiles. If the melt fraction ϕ is between 0 and 1, the average density is computed using volume-additivity. Similarly, thermal expansivity is averaged volumetrically assuming the Reuss approximation (Stacey, 1998).

Mineralogy	K_0 (GPa)	K'	ρ_s (kg/m^3)
upper mantle	163	4.0	3240
transition zone	85	4.0	3226
bridgmanite	210	3.9	3870
post-perovskite	210	3.9	3906
melt	30	6.0	2750

Table 4.1 | Birch-Murnaghan parameters for reference density profile. K_0 is the bulk modulus at pressure $P = 0$, K_0' the pressure derivative of the bulk modulus at $P = 0$, and ρ_s is the surface density.

The thermal expansivity is calculated using:

$$\alpha = \frac{\rho\gamma C_p}{K} \tag{4.1}$$

Where γ is the Grüneisen parameter, C_p is the heat capacity, ρ the density, and K the bulk modulus.

4.2.4 Rheology

Diffusion creep is the dominant deformation mechanism at higher pressures while dislocation creep is the main deformation mechanism of the upper mantle (Karato and Wu, 1993). We therefore neglect dislocation creep as the majority of mantle material is at high pressure. Adding dislocation creep would have the effect of reducing the mantle viscosity contrast that is caused by the pressure and temperature-

dependence (Christensen, 1984). We employ an Arrhenius type viscosity law for diffusion creep:

$$\eta(P,T) = \eta_0 \exp\left(\frac{E_a + PV_a(P)}{RT} - \frac{E_a}{RT_0}\right) \tag{4.2}$$

Where P is pressure, T is temperature, T_0 is the temperature at $P = 0$, E_a is the activation energy, $V_a(P)$ the activation volume and $R = 8.31445\,\mathrm{JK^{-1}mol^{-1}}$ the universal gas constant, and η_0 is a reference viscosity. The activation volume depends on pressure following the law:

$$V_a(P) = V_0 \exp\left(-\frac{P}{P_{decay}}\right) \tag{4.3}$$

Where P_{decay} is the decay pressure controlling the pressure dependence of the activation volume. The post-perovskite lower bound parameters from (Tackley et al., 2013) are used: $E_a = 162\,\mathrm{kJ/mol}$, $V_0 = 1.40\,\mathrm{cm^3/mol}$ and $p_{\mathrm{decay}} = 1610\,\mathrm{GPa}$. We use a minimum and maximum cutoff for the viscosity of $\eta_{\mathrm{min}} = 10^{18}\,\mathrm{Pa\,s}$ and $\eta_{\mathrm{min}} = 10^{28}\,\mathrm{Pa\,s}$. The outermost, rigid layer of a planet (lithosphere) is prone to failure if differential stresses are sufficiently large. We model this through a plastic yielding criteria. At low pressure, the strength of the lithosphere is related to its fracture strength or frictional sliding of faults (Byerlee's law (Byerlee, 1978)). At higher pressure, the strength is related to ductile failure caused by dislocation motion of the lattice (Kohlstedt et al., 1995). Both, the brittle and ductile components are encapsulated within a pressure-dependent yield stress σ_y:

$$\sigma_{\mathrm{y}} = \min(c_f P, \sigma_{\mathrm{duct}} + \sigma'_{\mathrm{duct}} P) \tag{4.4}$$

Where c_f is the friction coefficient and σ'_{duct} is the ductile yield stress gradient. If the stress exceeds the yield stress σ_y, the viscosity gets reduced to an effective viscosity given by:

$$\eta_{\mathrm{eff}} = \frac{\sigma_{\mathrm{y}}}{2\dot{\epsilon}_{\mathrm{II}}} \quad \text{if} \quad 2\eta\epsilon_{\mathrm{II}} > \sigma_y \tag{4.5}$$

Where $\dot{\epsilon_{\mathrm{II}}}$ is the second invariant of the strain rate tensor.

4.2.5 Boundary conditions

The surface boundary condition is free-slip and radiative. The surface temperature is determined using the following radiative equilibrium equation:

$$\sigma T_s^4 = F_{\text{top}} + \sigma T_{\text{rad}}^4 \tag{4.6}$$

Where $\sigma = 5.670 \cdot 10^{-8}\,\text{Wm}^{-2}\text{K}^{-4}$ is the Stefan-Boltzmann constant, F_{top} is the surface heat flux from the interior and T_s is the surface temperature. T_{rad} is defined as the temperature of the planet when it is in stellar equilibrium with the irradiation from the star taking into account the effects of a potential atmosphere.

We determine T_{rad} using general circulation models (GCMs) by assuming different compositions and optical depths τ of the atmosphere. Figure 4.1 shows the surface temperature profiles inferred from the GCMs. The atmospheres differ in molecular weight (dominated by hydrogen H_2 or N_2) and optical depth τ. If large portions of the surface are molten, F_{top} can be very high and the surface temperature significantly different from the radiative equilibrium temperature. If the surface is solid, F_{top} is small and $T_s \approx T_{\text{rad}}$. The initial CMB temperature for all models is $T_{\text{CMB,init}} = 9500\,\text{K}$. There is still a large uncertainty on the temperature at the CMB of super-Earths. Here, we use an estimate for the melting temperature of $MgSiO_3$ at the CMB (Fei et al., 2021; Stixrude, 2014). We use a lower-bound value in order to avoid the formation of a basal magma ocean. A basal magma ocean, whilst interesting to investigate, would add additional complexity that would require its own study. Hence, we focus on the simpler scenario of a solid mantle at the interface with the core.

4.2.6 Melting

At each time step, the melt fraction at each cell is calculated, which is given by:

$$\phi = \frac{T - T_{\text{sol}}}{T_{\text{liq}} - T_{\text{sol}}} \tag{4.7}$$

The solidus temperature T_{sol} is given by Herzberg et al. (2000) for the upper mantle, Zerr et al. (1998) for the lower mantle, and Stixrude (2014) for the post-perovskite

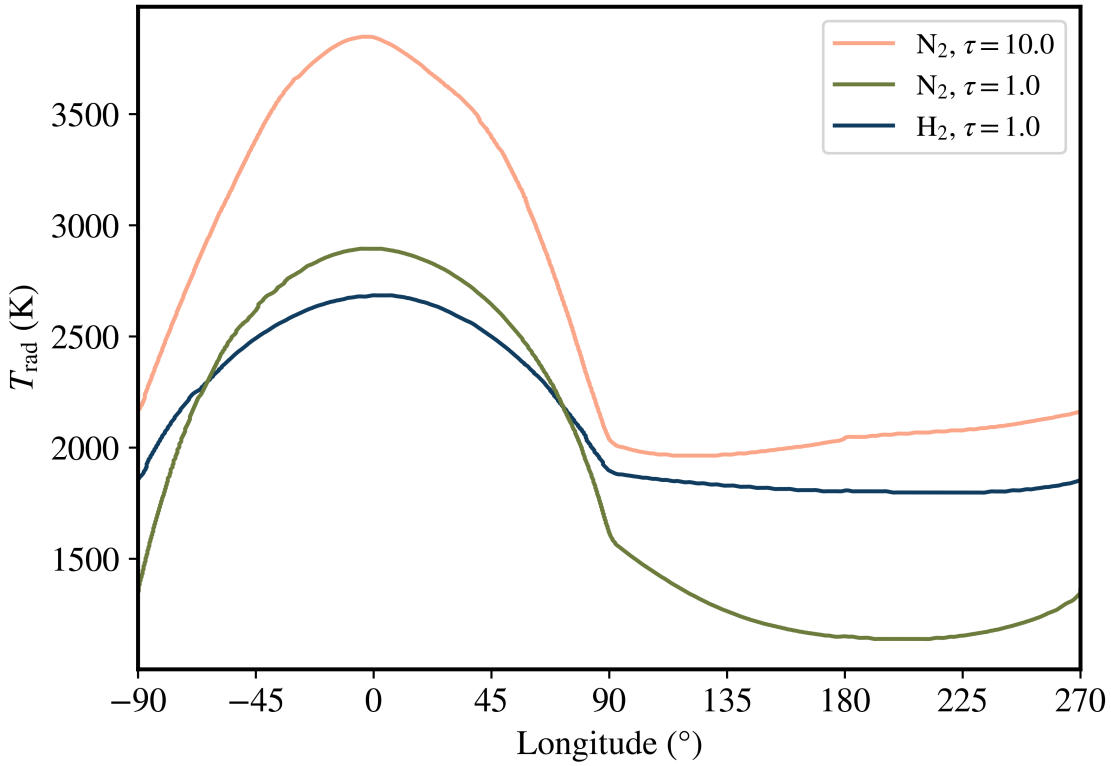

Figure 4.1 | Radiative temperatures T_{rad} that are derived from different general circulation models. T_{rad} is used to determine the surface temperature of the planet using Equation 4.6. H_2 indicates a low molecular weight atmosphere dominated by hydrogen, and N_2 indicates a high molecular weight atmosphere dominated by nitrogen. τ is the optical depth of the atmosphere.

phase. The liquidus is given by a compromise between Zerr et al. (1998), Stixrude et al. (2009), and Andrault et al. (2011).

If melt is present, we parametrise the heat flux J_{q} by assuming a very high effective thermal conductivity k_{h} (eddy diffusion) (Abe, 1997). k_{h} varies as a function of the melt fraction ϕ:

$$k_{\mathrm{h}} = \frac{k_{\mathrm{h,max}}}{2}\left(1 + \tanh\frac{\phi - \phi_c}{\Delta\phi}\right) - 1 \tag{4.8}$$

Where $\phi_{\mathrm{c}} \approx 0.35$ is the rheological front (critical melt fraction) above which the mixture of solid and melt will behave rheologically as an inviscid fluid (Abe, 1997). $\Delta\phi = 0.05$ is the width of this transition between solid- and liquid-like rheological behaviour. For the maximum effective thermal conductivity for melt, we use $k_{\mathrm{h,max}} = 10^7\,\mathrm{Wm^{-1}K^{-1}}$. This is possible under the assumption that the magma ocean is vigorously convecting. However, this depends on whether the temperature gradient inside the magma ocean is super-adiabatic ($\frac{dT}{dr} > \frac{dT_a}{dr}$) or not. If the magma ocean is sub-adiabatic, it will not be convecting and therefore heat transport is not necessarily enhanced. In this study, we will therefore investigate two cases:

- *step-mode*: The heat flux J_{q} is enhanced only if $\frac{dT}{dr} > \frac{dT_a}{dr}$.
- *constant-mode*: The heat flux J_{q} is always enhanced if melt is present ($\phi > 0$).

We include latent heating effects ($0 < \phi < 1$) by assuming an effective heat capacity C_p' and an effective thermal expansion parameter α' in the energy equation (e.g., Solomatov, 2007):

$$C_p' = C_p + \frac{\Delta H}{T_{\mathrm{liq}} - T_{\mathrm{sol}}} \tag{4.9}$$

$$\alpha' = \alpha + \frac{\Delta\rho}{\bar{\rho}(T_{\mathrm{liq}} - T_{\mathrm{sol}})} \tag{4.10}$$

Where ΔL is the latent heat of melting/freezing, $\Delta\rho$ is the density difference between the solid and melt phase and $\bar{\rho}$ is the volumetrically averaged density. In order to model latent heating/cooling self-consistently, we fix the latent heat of melting/freezing and the density difference between the melt and solid phase is determined using:

$$\Delta\rho = \frac{\Delta L\bar{\rho}^2}{\gamma T} \tag{4.11}$$

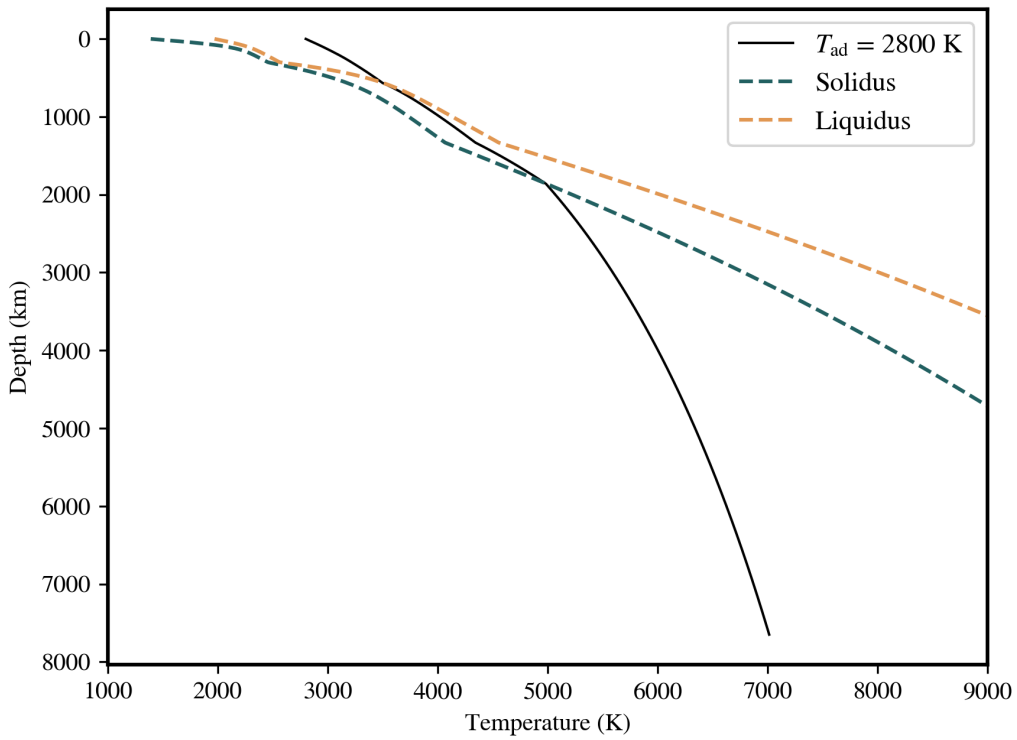

Figure 4.2 | Solidus and liquidus curves. The black line shows an adiabat with surface temperature $T_{\text{surf}} = 2800\,\text{K}$ where latent heat effects are included in the mixed phase region ($0 < \phi < 1$).

Where γ is the Clapeyron slope.

4.3 Results

4.3.1 Reference model without internal heating/core cooling

As a reference model, we use a substellar point temperature of $T_{\text{day}} = 2800\,\text{K}$ and nightside temperature of $T_{\text{night}} = 1150\,\text{K}$. The thermal conductivity for melt is only increased if the temperature gradient is super-adiabatic (*step-mode*). The potential mantle temperature is 2800 K.

Figure 4.3 shows the temperature field at 4.6 Gyrs for this reference model. A prominent plume has formed on the dayside of the planet and there is a flow of solid material from the nightside towards the dayside (indicated by the vector field). The

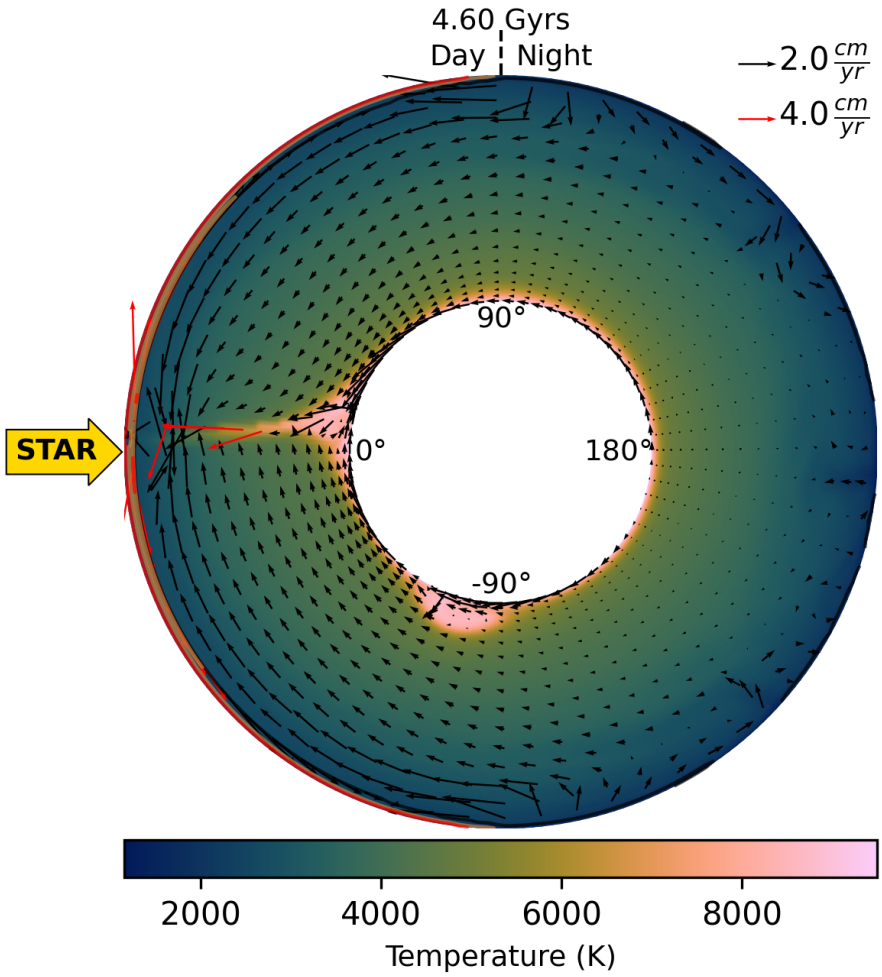

Figure 4.3 | Mantle temperature field and velocity field of super-Earth 55 Cancri e for the reference model. High velocities ($\|v(r,\phi)\| > 2\langle\|v(r,\phi)\|\rangle_{\text{mantle}}$) are plotted with a red arrow. The magma ocean is indicated in red (fully molten) and orange (partially molten).

return flow from dayside towards the nightside is accommodated inside the magma ocean and the uppermost solid part of the mantle. Velocities in the (near) magma ocean region are much higher than in the solid mantle. We therefore use a different scale for the high velocities (red arrows). At the beginning of the run, the magma ocean has a depth of around 3500 km on the dayside (fully molten) and 2700 km on the nightside (partially molten). At 4.6 Gyrs, the magma ocean has a thickness of around 437 km on the dayside (fully molten) and the nightside is mostly solid. Figure 4.6A shows the corresponding surface and CMB heat flux. The dayside is fully molten and therefore has a much greater heat flux than the nightside. The heat flux at the CMB is $\approx 375\,\text{mW/m}^2$.

4.3.2 Reference model comparison

In this section, the parameters are the same as for the reference model, but we now apply different internal heating rates, and the models use either core cooling or no core cooling. The temperature at the substellar point is $T_{day} = 2800\,K$ and the nightside temperature is $T_{night} = 1150\,K$. The internal heating rate is $H = 0$ (no internal heating), $H = 5.2 \cdot 10^{-12}\,W/kg$ (Present-day Earth-like internal heating), and $H = 1.4 \cdot 10^{-11}\,W/kg$ (high internal heating). Figure 4.5 shows the temperature and velocity field plots of the mantle of 55 Cancri e after 4.6 Gyrs (or 3.6 Gyrs for the model with high internal heating). In all cases, a prominent upwelling forms on the dayside and there is a flow of solid material from the nightside towards the dayside. Solid material on the nightside moves more slowly than it is moving on the dayside. The return flow from the dayside towards the nightside is accommodated in the near-surface layer, which is molten on the dayside for all models and partially molten on the nightside. The thickness of the partially molten magma ocean on the nightside is however very thin for the models with no internal heating ($MO_{depth} < 50\,km$).

Figure 4.7 shows the mean mantle temperature for the different reference model cases (i.e., $T_{day} = 2800\,K$ and $T_{night} = 1150\,K$). The models with high internal heating stabilise around 1 Gyr with a mantle temperature around 4200 K. There is not a big difference in the mean mantle temperature between the models with core cooling and without core cooling. With an Earth-like internal heating rate, the model is still cooling after 2 Gyrs and the temperature in the mantle is around 50 K cooler if the core is allowed to cool. As expected, the model without internal heating cools the most and will continue to cool beyond 4.6 Gyrs. The mean mantle temperature at that time is around 3627 K if core cooling is enabled, and around 3696 K if core cooling is not enabled. Physically, the core of a planet will always be cooling. The results of our models show, however, that including this effect does not change the mean mantle temperature or the mantle dynamics significantly. With a high internal heating rate, the mantle temperature remains constant after ≈ 1.2 Gyrs at around 4200 K independent of whether the core is allowed to cool or not.

Figure 4.6 shows the surface and CMB heat flux for the different models. The nightside heat flux (shown in blue dot-dashed) and the CMB heat flux (dashed lines)

are shown in $\mathrm{mW/m^2}$ (right axis). The red solid line shows the dayside surface heat flux in $\mathrm{W/m^2}$ (left axis). For the models without core cooling, the CMB heat flux after 4.6 Gyrs (or 3.6 Gyrs for the case with high internal heating) is $\approx 355\,\mathrm{mW/m^2}$, $\approx 363\,\mathrm{mW/m^2}$, and $\approx 389\,\mathrm{mW/m^2}$ for no, Earth-like, and high internal heating respectively. When the core is allowed to cool, the CMB heat flux will also steadily decrease over time. With no internal heating the flux at 4.6 Gyrs is $\approx 68\,\mathrm{mW/m^2}$, with $H = 5.2 \cdot 10^{-12}\,\mathrm{W/kg}$ it is $\approx 62\,\mathrm{mW/m^2}$ and for high internal heating it is slightly higher at $\approx 78\,\mathrm{mW/m^2}$ (at 3.6 Gyrs). The dayside surface flux is roughly 3 orders of magnitude larger than the nightside surface flux for all model cases, which is why we show it using a separate axis in $\mathrm{W/m^2}$. This is because the dayside harbours a fully molten magma ocean, whereas the nightside is only partially molten or solid.

In summary, we observe for all models that a magma ocean forms on the dayside of the planet and the nightside is partially molten. The most prominent feature is the strong upwelling that is present on the dayside for all models (i.e., independent of the amount of internal heating and whether the core is allowed to cool or not). If upwellings form around the CMB, they tend to move towards the dayside and merge with the upwelling that is already present. Solid mantle material moves passively from the nightside surface into the mantle and then towards the dayside. The return flow of material from the dayside towards the nightside is accommodated in the magma ocean and uppermost layer of the solid mantle where the viscosity is the lowest.

4.3.3 Models with different surface temperature contrasts

In this section, we show the results for the interior dynamics models of 55 Cancri e for different surface temperature contrasts. The different radiative temperature profiles are taken from the general circulation models and are shown in Figure 4.1. All models feature Earth-like internal heating ($H = 5.2 \cdot 10^{-12}\,\mathrm{W/kg}$) and include core cooling. Figure 4.8 shows snapshots of the mantle temperature and viscosity at 4.6 Gyrs. Figure 4.9 shows the corresponding evolutionary tracks. For the model with a dayside temperature of $T_{\mathrm{day}} = 2750\,\mathrm{K}$ and nightside temperature of $T_{\mathrm{night}} = 1100\,\mathrm{K}$, this model is very similar to the reference case (with the dayside temperature

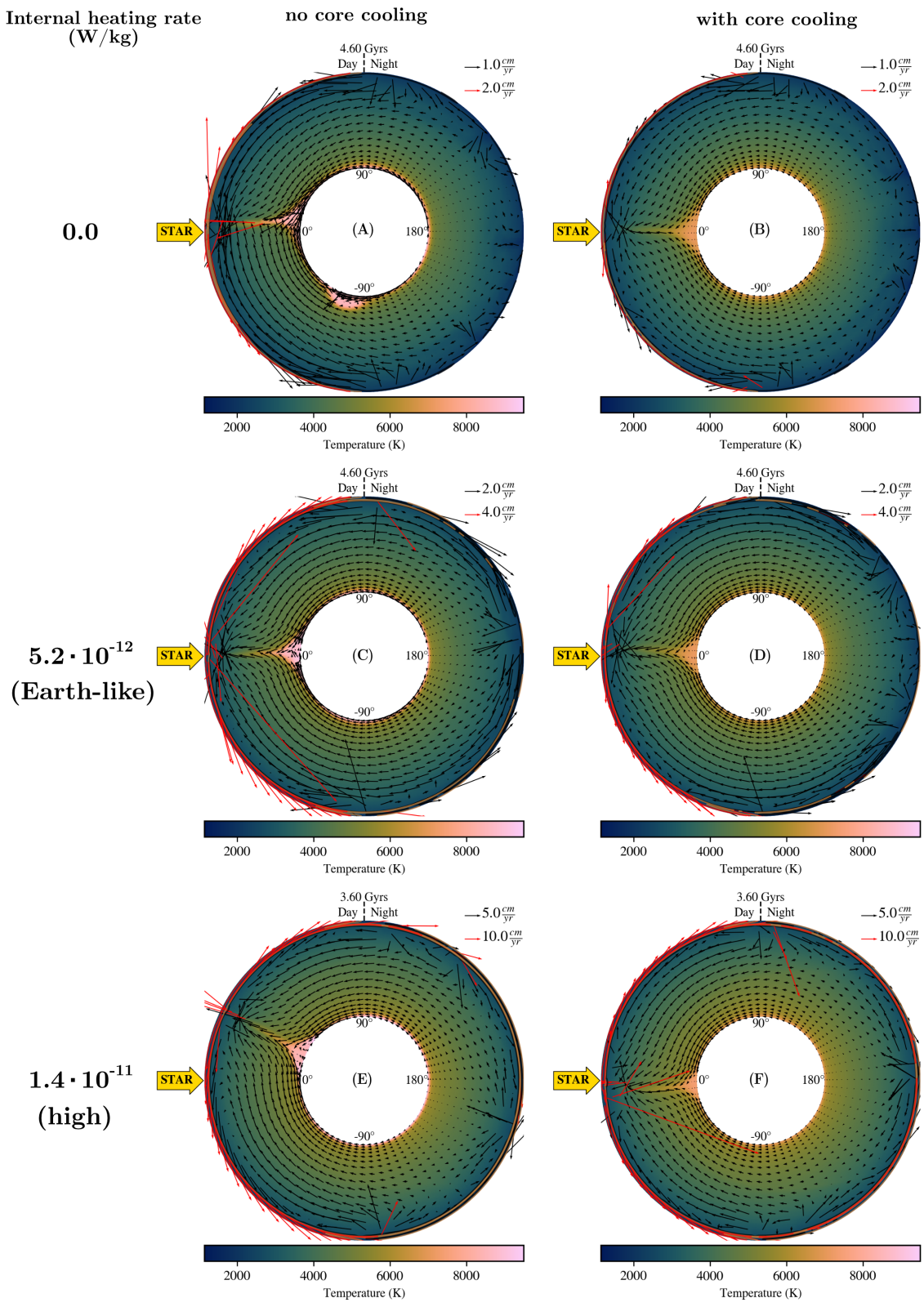

Figure 4.4 | Snapshot of mantle temperature and velocity fields for the 55 Cancri e models with $T_{\text{day}} = 2800\,\text{K}$ and $T_{\text{night}} = 1150\,\text{K}$. High velocities ($\|v(r,\phi)\| > 2\langle\|v(r,\phi)\|\rangle_{\text{mantle}}$) are indicated by red arrows. The magma ocean is indicated in red (fully molten) and orange (partially molten). Models with high internal heating have only been run up to 3.6 Gyrs, because the higher velocities require smaller time steps increasing the needed computation power drastically.

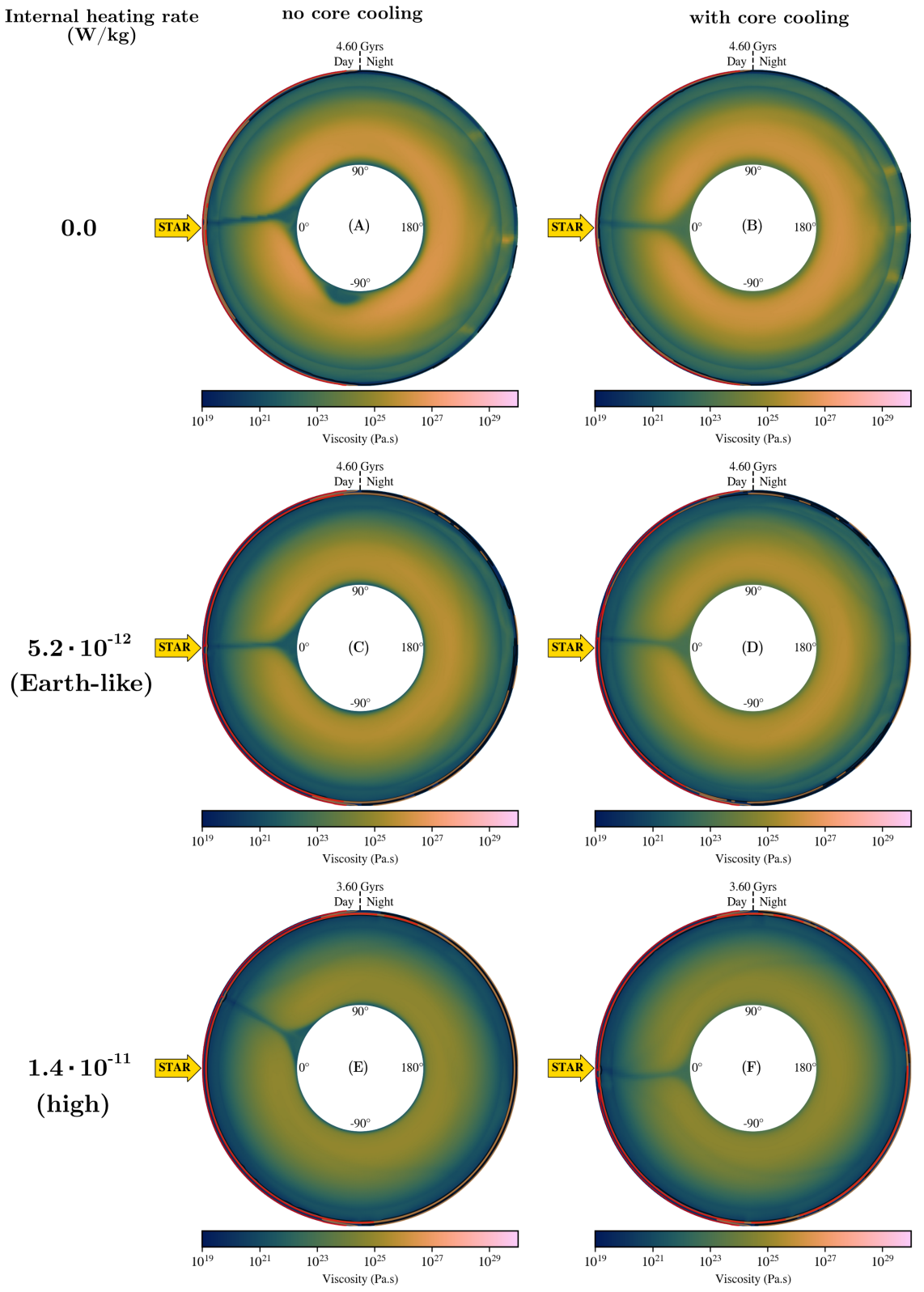

Figure 4.5 | Snapshot of mantle viscosity for the 55 Cancri e models with $T_{\mathrm{day}} = 2800\,\mathrm{K}$ and $T_{\mathrm{night}} = 1150\,\mathrm{K}$. The magma ocean is indicated in red (fully molten) and orange (partially molten). Models with high internal heating have only been run up to 3.6 Gyrs, because the higher velocities require smaller time steps increasing the needed computation power drastically.

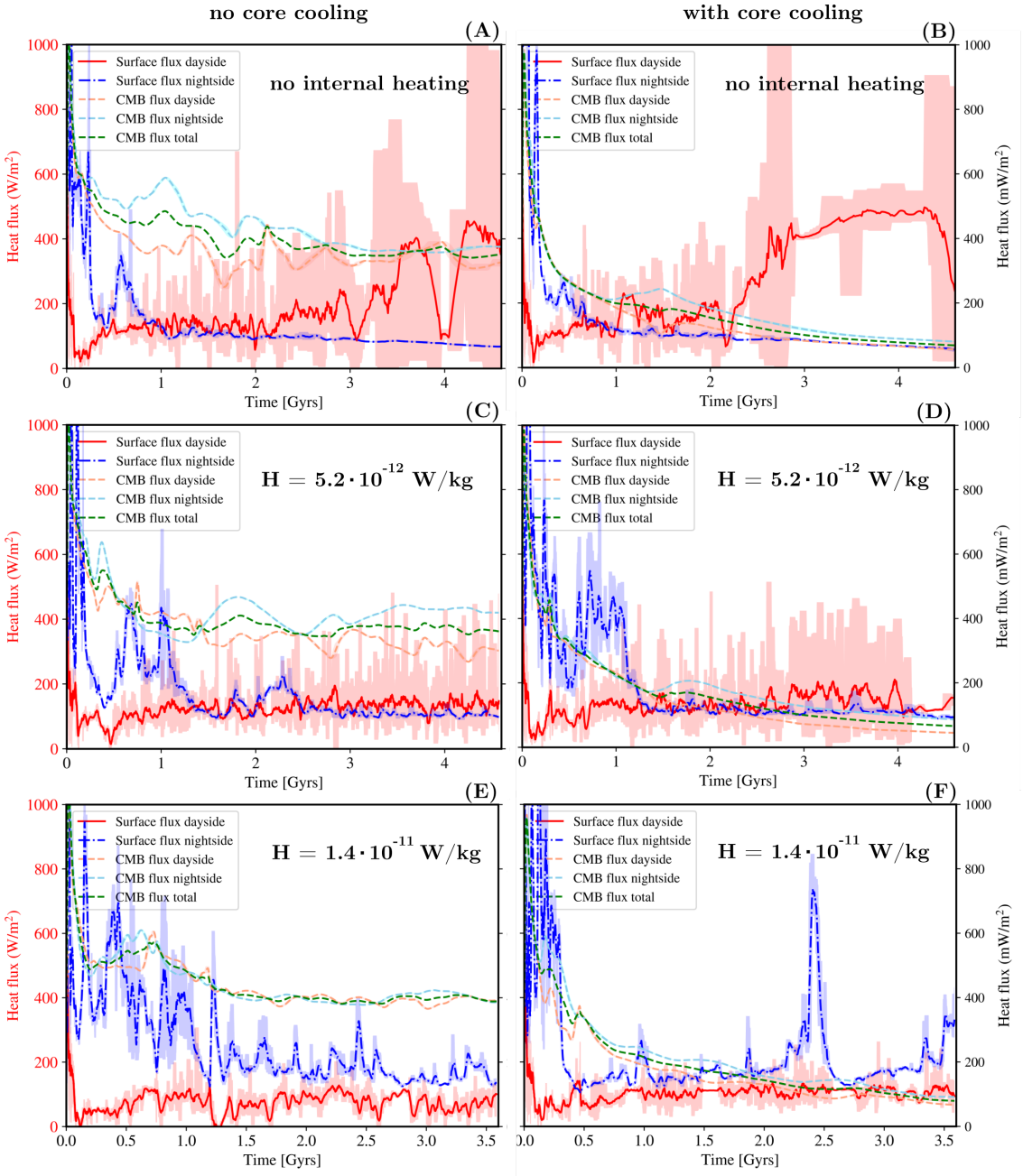

Figure 4.6 | Surface and CMB heat flux evolution (moving average value of 20 time steps) for the 55 Cancri e models with $T_{\mathrm{day}} = 2800\,\mathrm{K}$ and $T_{\mathrm{night}} = 1150\,\mathrm{K}$. Solid lines are in $\mathrm{W/m^2}$ (left axis) and dashed or semi-dashed lines are in $\mathrm{mW/m^2}$ (right axis). The shaded regions on either side of the lines represent the minimum and maximum values within the moving average window.

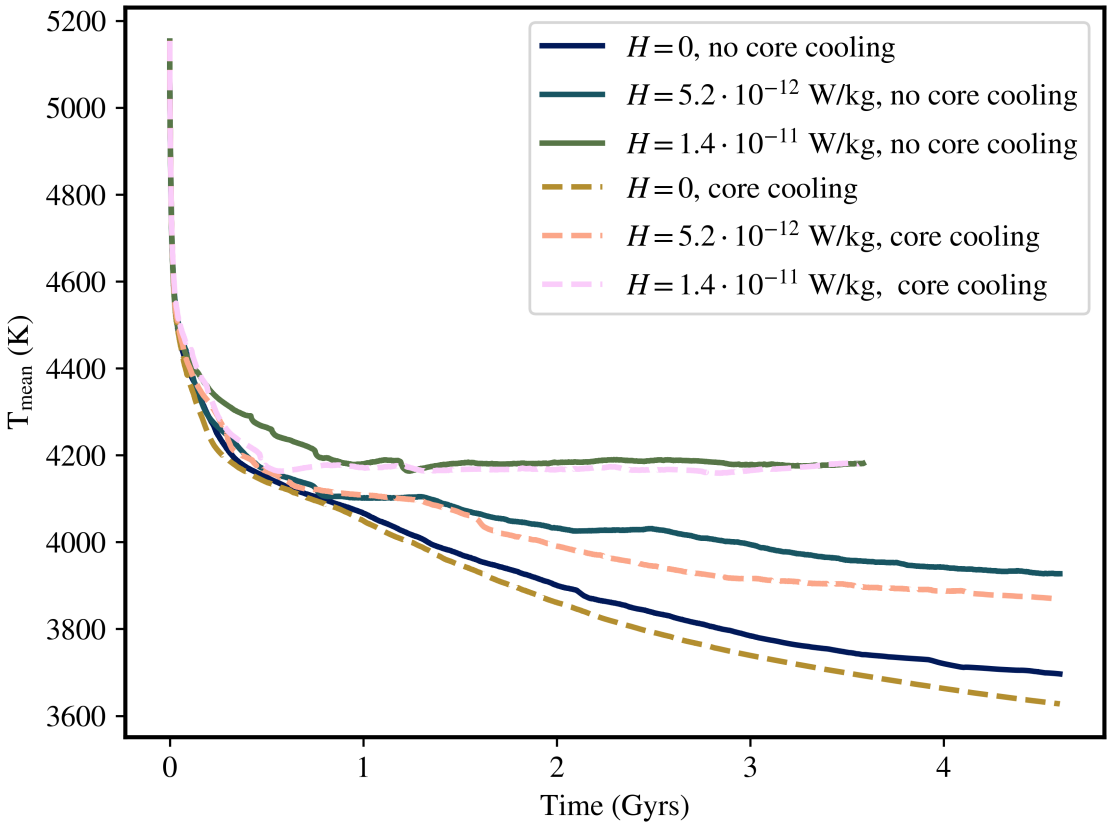

Figure 4.7 | Mean mantle temperature for different models of 55 Cancri e with different rates of internal heating and core cooling. The dashed lines indicate models that feature core cooling. Solid lines indicate models that do not feature core cooling.

being slightly cooler). A strong upwelling forms on the dayside of the planet and cold material gets passively moved inside the deep mantle on the nightside (Fig. 4.8: A1, A2). Figure 4.10A shows snapshots of the mantle temperature at different time steps. A second plume forms around 0.2 Gyrs which then moves towards the dayside and merges with the dominant plume that is already present on that side. No more plumes form after this merging, which is completed after roughly 0.8 Gyrs. The plumes that are shown in the evolutionary tracks plot between around 1 and 2 Gyrs (Fig. 4.9A) correspond only to a slightly thickened thermal boundary layer. At 4.6 Gyrs, the magma ocean on the dayside has a thickness of around 437 km and the nightside surface is mostly solid. The mean mantle temperature after 4.6 Gyrs is around 3822 K and the mantle is still continuing to cool (Fig. 4.11).

For the model with a dayside temperature of $T_{\mathrm{day}} = 2600\,\mathrm{K}$ and nightside temperature of $T_{\mathrm{night}} = 1800\,\mathrm{K}$, an upwelling also forms on the dayside and cold, solid material passively moves into the deep mantle on the nightside (Fig. 4.8: B1, B2). The plume on the dayside is stable over several Gyrs (Fig. 4.10B). No additional plumes form once the dominant plume on the dayside has formed; rather, the lower boundary layer continuously drains through the established plume (Fig. 4.9B). At 4.6 Gyrs, the magma ocean on the dayside has a thickness of around 495 km and around 380 km on the nightside. Although the surface is only partially molten on the nightside. The mean mantle temperature after 4.6 Gyrs is stable at around 4090 K. This temperature is reached after roughly 0.6 Gyrs (Fig. 4.11).

The model with a dayside temperature of $T_{\mathrm{day}} = 3900\,\mathrm{K}$ and nightside temperature of $T_{\mathrm{night}} = 2000\,\mathrm{K}$ is the model with the hottest dayside temperature that we investigated and also features the strongest temperature contrast. The magma ocean will cover the whole planet in this case, equilibrating the temperatures between the interface of the magma ocean and the underlying solid mantle. Consequently, the plumes now form uniformly around the CMB and do not tend to move towards the dayside anymore. At 4.6 Gyrs, a prominent plume is present on the nightside (Fig. 4.8: C1, C2). However, this plume is not as stable as in the cases where the nightside is cool enough to be solid or partially molten with a prominent plume that forms on the dayside. One can see on Figure 4.9 that the dominant plume on the dayside starts to move towards the nightside at around 2.5 Gyrs. Figure 4.10C

shows the mantle temperature at 4 different time steps: At 0.5 Gyrs, two plumes have formed on the dayside and nightside. At around 1.5 Gyrs, two more plumes are forming on the nightside which will then merge with the already present plume on that side. At 2.5 Gyrs, the plume on the dayside starts to move towards the nightside and merges with the plume on the nightside at around 3 Gyrs. The mantle temperature reaches a stable state after roughly 0.6 Gyrs. The mean mantle temperature after 4.6 Gyrs is around 4382 K.

Figure 4.12 shows the surface and CMB heat flux for the different models. For the model with $T_{\text{day}} = 2750\,\text{K}$ and $T_{\text{night}} = 1100\,\text{K}$, the heat flux on the dayside varies between 50 to 200 W/m^2 and the nightside heat flux is steadily decreasing reaching roughly 100 mW/m^2 after 4.6 Gyrs. The CMB heat flux after 4.6 Gyrs is around 68 mW/m^2. For the model with $T_{\text{day}} = 2600\,\text{K}$ and $T_{\text{night}} = 1800\,\text{K}$, the dayside heat flux is around 50 W/m^2 and the nightside heat flux around 25 W/m^2 for most of the time, but increases to around 100 W/m^2 after 3.6 Gyrs. The CMB heat flux after 4.6 Gyrs is around 73 mW/m^2. For the model with $T_{\text{day}} = 3900\,\text{K}$ and $T_{\text{night}} = 2000\,\text{K}$, the dayside heat flux varies from 0 to $-200\,\text{W/m}^2$. A negative heat flux means that heat is flowing into the mantle. From Figure 4.11, we can however see that there is no significant heating of the mantle. Heat flowing into the mantle through a temperature inversion is most likely not very efficient compared to the heat that is immediately radiated away from the surface. The nightside heat flux is around 1–4 W/m^2. The CMB heat flux after 4.6 Gyrs is approximately 51 mW/m^2.

In summary, we find that a large super-plume forms on the dayside of the planet if the dayside harbours a magma ocean and the nightside remains solid or is partially molten. Cold material moves passively into the interior on the nightside and towards the dayside. If the nightside also harbours a magma ocean, the temperature at the interface between the magma ocean and the underlying solid mantle equilibrates, so that plumes and passive downwellings do not have a preferred location anymore.

4.3.4 Models with constant high eddy diffusivity

In this section, we show the results for the same models as in 4.3.3, but where the eddy diffusivity is always increased in the melt relative to the solid, regardless of whether the temperature gradient is super-adiabatic or not (*constant-mode*).

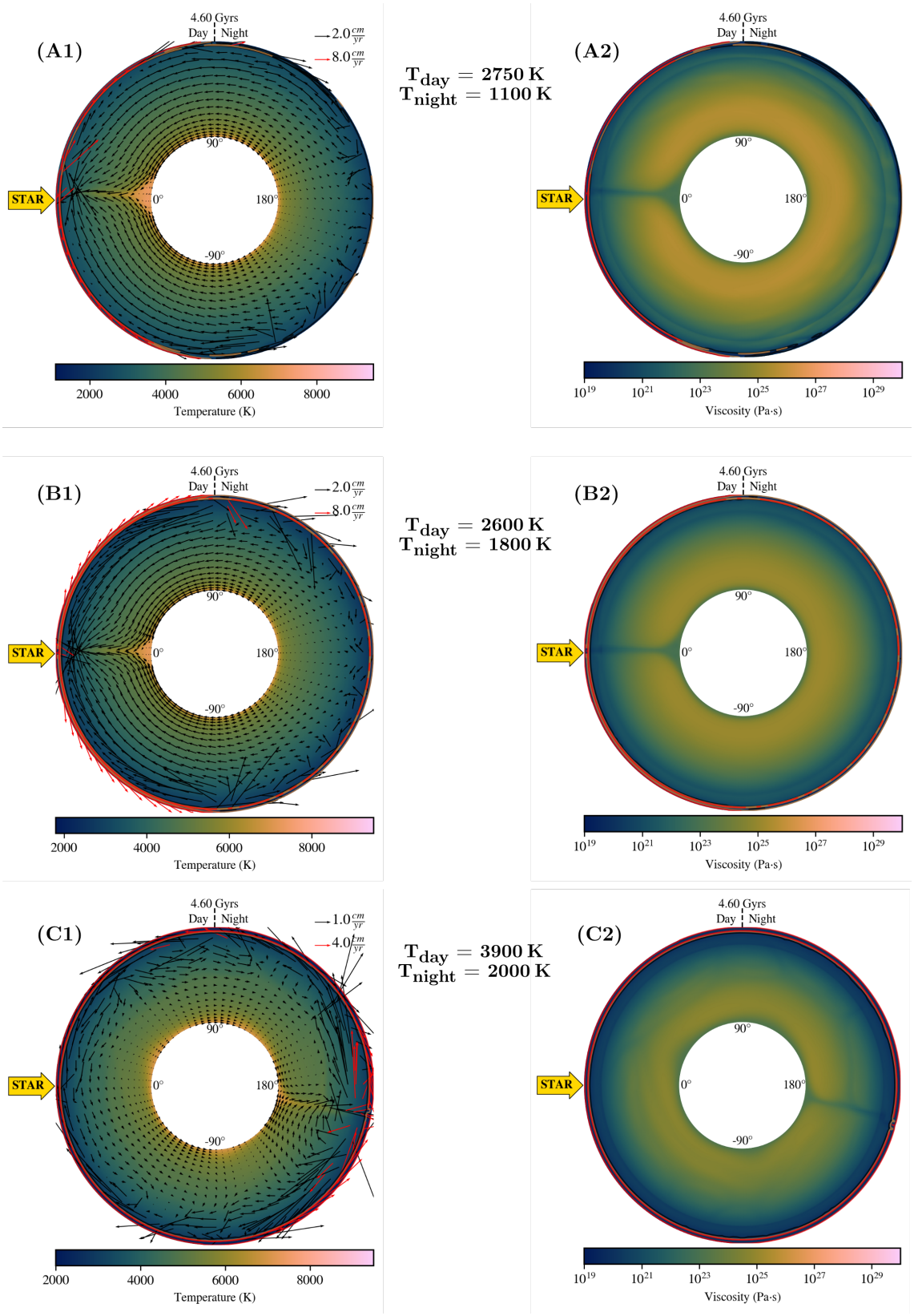

Figure 4.8 | Snapshots of mantle temperature (left column) and viscosity (right column) for different models of 55 Cancri e with different surface temperature contrasts. High velocities ($\|v(r,\phi)\| > 2\langle\|v(r,\phi)\|\rangle_{\text{mantle}}$) are indicated by red arrows. The magma ocean is indicated in red (fully molten) and orange (partially molten).

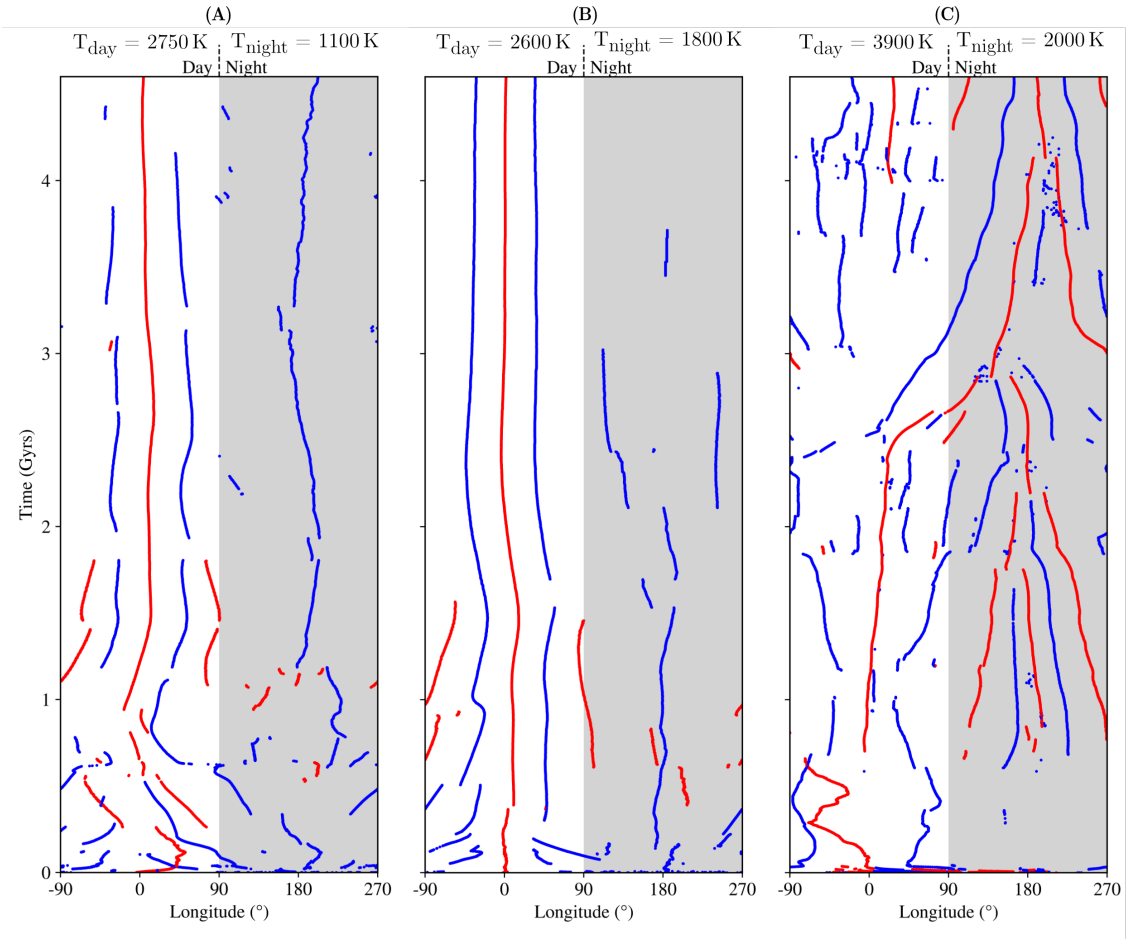

Figure 4.9 | Evolutionary tracks of upwellings (red) and (passive) downwellings (blue) for the models with different surface temperature contrasts.

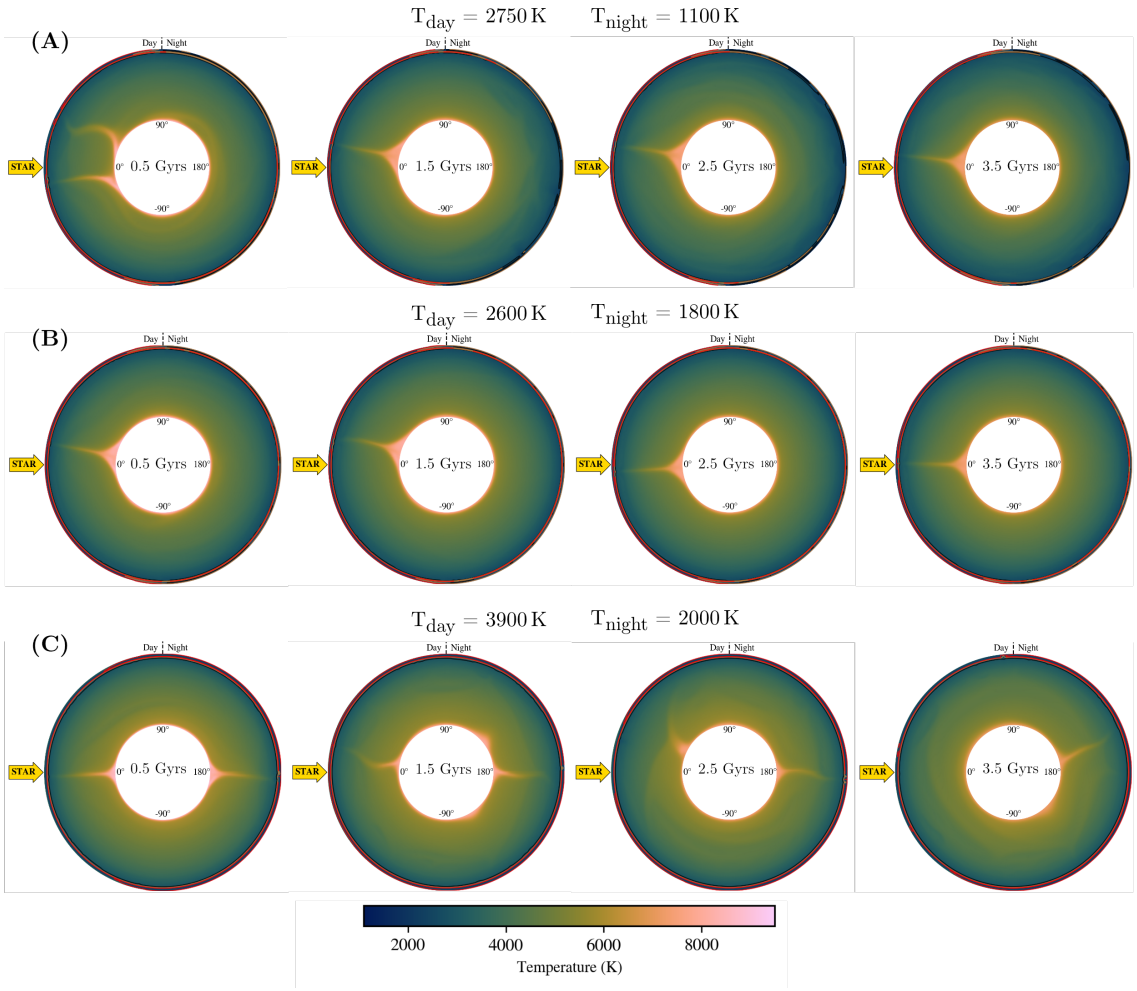

Figure 4.10 | Snapshots of mantle temperature of 55 Cancri e at different time steps for the models with different surface temperature contrasts. The magma ocean is indicated in red (fully molten) and orange (partially molten).

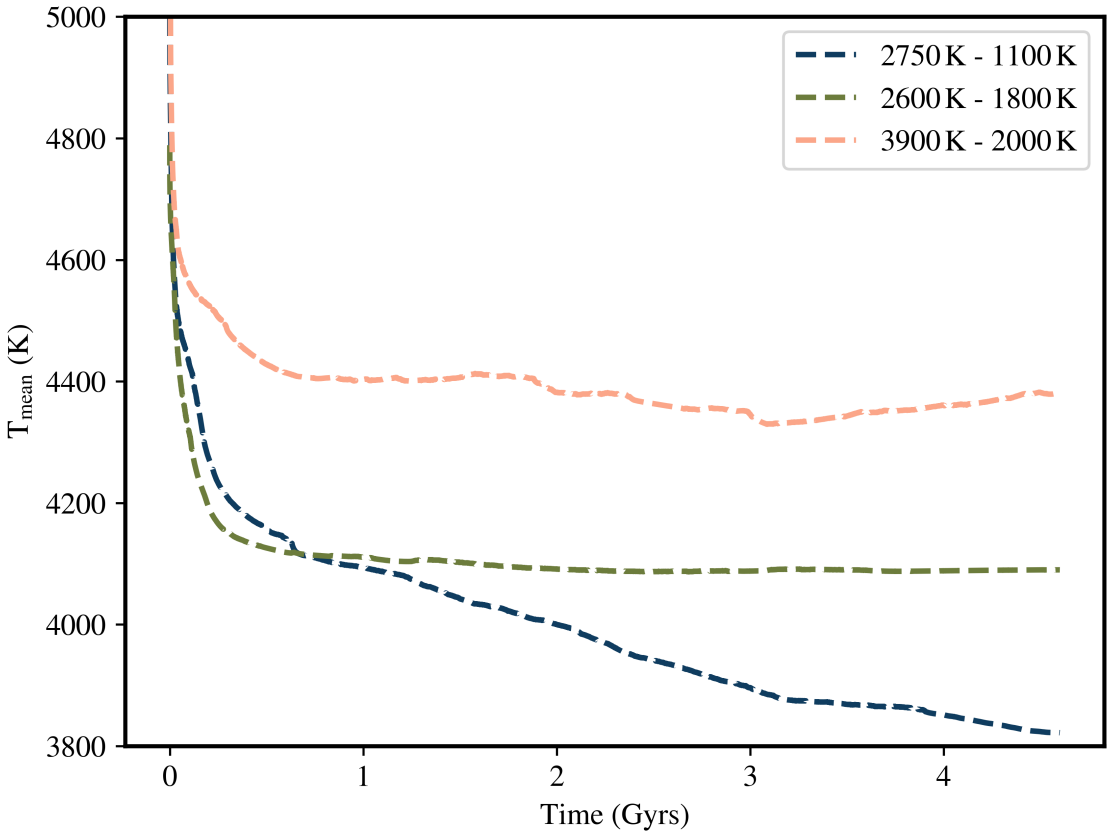

Figure 4.11 | Mean temperature of the mantle of 55 Cancri e for models with different surface temperature contrasts.

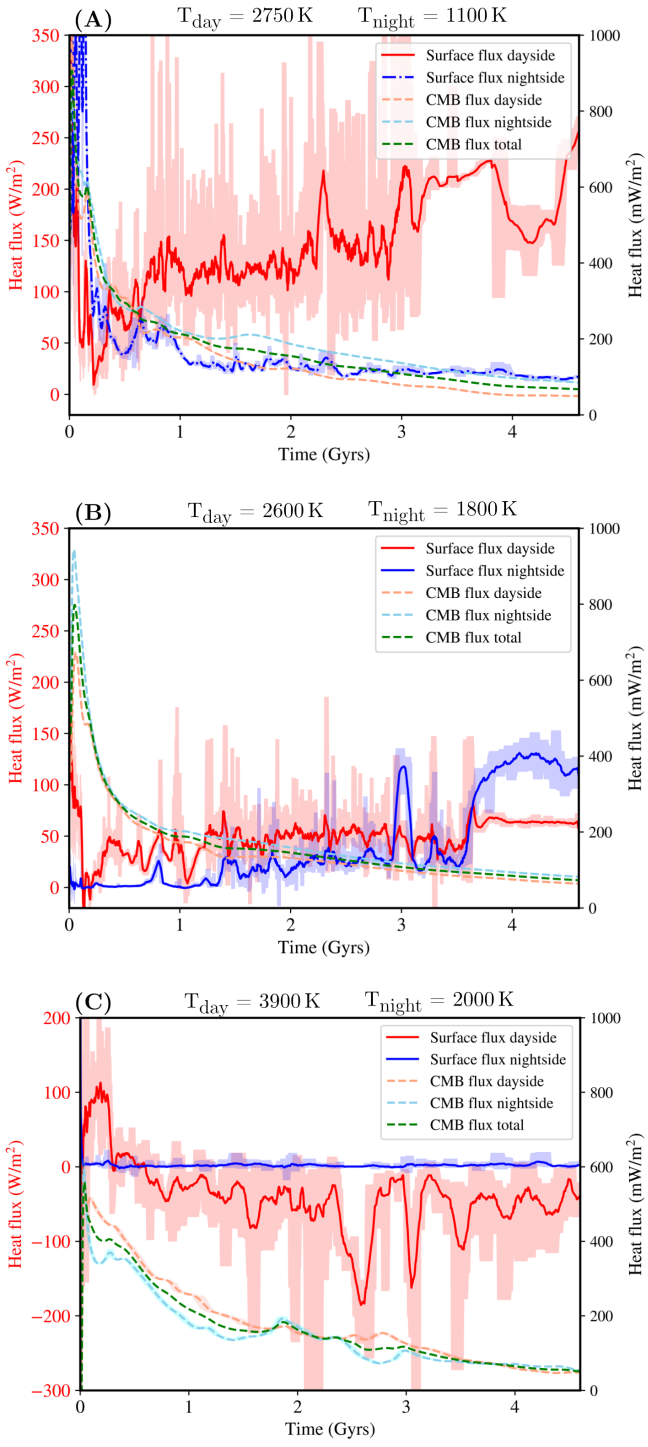

Figure 4.12 | Surface and CMB heat flux for models with different surface temperature contrasts. The dashed lines are in mW/m^2 (right axis) and the solid lines in W/m^2 (left axis). The shaded regions on either side of the lines represent the minimum and maximum values within the moving average window (20 time steps).

Figure 4.13 shows snapshots of the mantle temperature and viscosity for the different models. The vector plot shows the velocity field and the contour plot shows the melt fraction ϕ ($\phi = 1$ in red, $\phi = 0.5$ in orange, and $\phi = 0.0$ in black). The temperatures are higher than in the case where only super-adiabatic cells have an enhanced eddy diffusivity. This leads to lower viscosities and higher velocities, which is why we did not run the models up to 4.6 Gyrs. However, the models have reached a steady state after around 100–200 Myrs.

For all models, we see a significant increase in the depth of the dayside magma ocean. The depth of the magma ocean varies between 3000 to 4000 km. This is because the magma ocean in the *step-mode* is mostly sub-adiabatic and therefore not vigorously convecting. It can therefore not efficiently transport heat into the deep mantle. If we allow the magma ocean to always be vigorously convecting (even if it is sub-adiabatic) the magma ocean will subsequently transport heat efficiently in the interior and increase in thickness until its temperature profile crosses the liquidus and solidus profiles of the mantle.

4.4 Discussion and Implications

4.4.1 Tectonic regime

Our results show that a degree-1 pattern convection is established if the dayside is molten and the nightside is solid (or only partially molten). A super-plume (also called mega-plume; see section 4.4.2) preferentially forms on the dayside and cold material passively moves into the interior on the nightside and then gets moved towards the dayside. The return of flow of material from the dayside towards the nightside is accommodated in the magma ocean and the near-magma ocean solid mantle. For models with higher nightside temperatures, where the nightside also becomes fully molten, we find that the convection pattern is now more similar to a regime with a uniform surface temperature with plumes forming all around the core mantle boundary layer. These plumes do not have a preferred location anymore and a degree-2 convection pattern is also a stable regime (Figure 4.10: C). A (super-adiabatic) magma ocean that covers the whole planet will be very efficient in redistributing heat. This will equilibrate the temperatures at the interface between

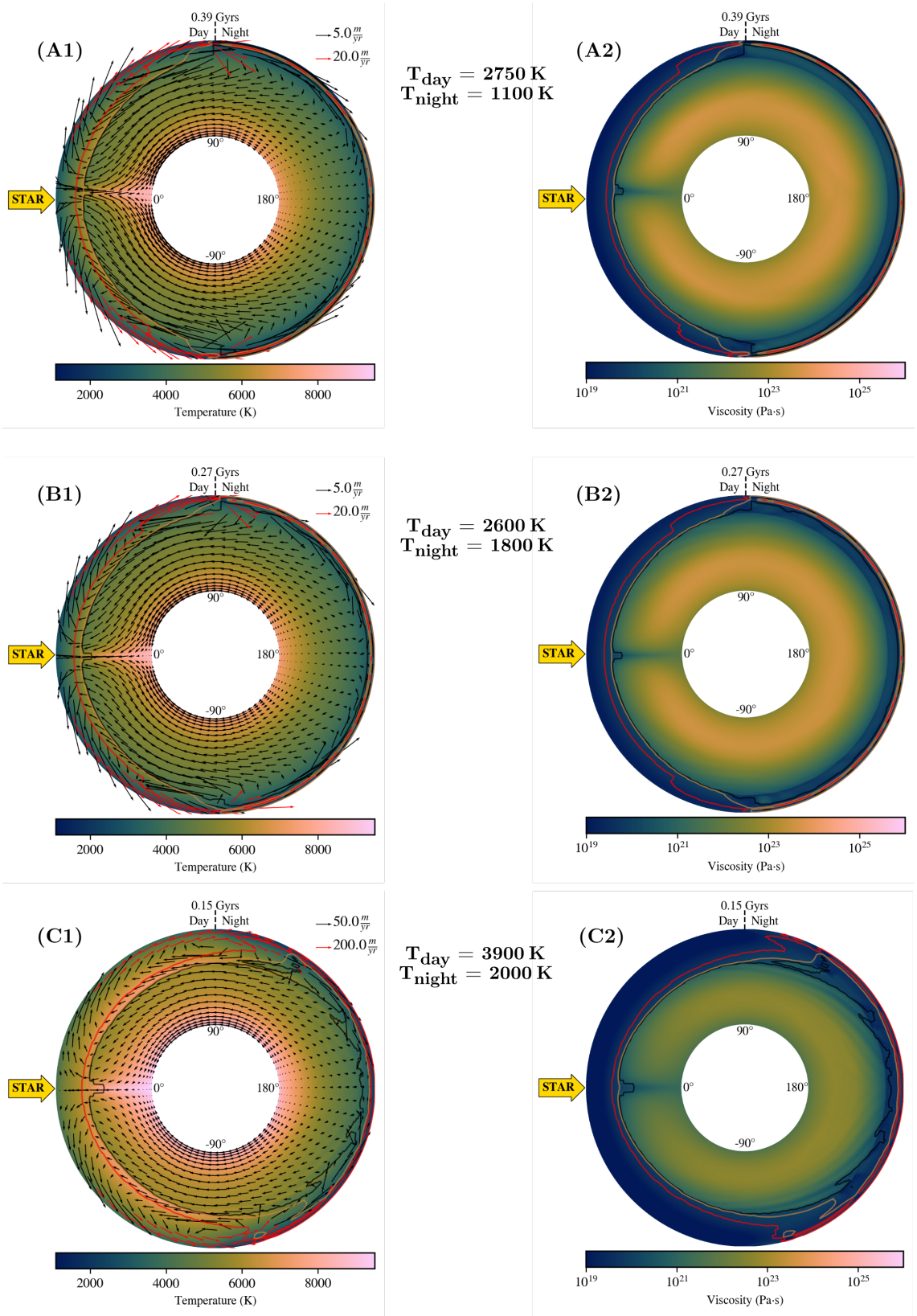

Figure 4.13 | Snapshots of mantle temperature (left column) and viscosity (right column) for different models of 55 Cancri e with different surface temperature contrasts and where k_h does not depend on the adiabatic temperature gradient. High velocities ($\|v(r,\phi)\| > 2\langle\|v(r,\phi)\|\rangle_\mathrm{mantle}$) are indicated by red arrows. The contour plot shows the melt fraction ($\phi = 1$ in red, $\phi = 0.5$ in orange, and $\phi = 0.0$ in black).

the magma ocean and the underlying solid mantle, thereby creating a boundary condition for the underlying solid mantle that is basically uniform.

4.4.2 Super-Plume

Our models show that so-called super-plumes can form in the interior mantle of 55 Cancri e. If the dayside harbours a magma ocean and the nightside is solid or partially molten, this super-plume will preferentially be on the dayside. The plume is rather stable located at the substellar point (0°), although some of the models show that it can move up to 30° east or west within approximately 1 Gyr (e.g. Fig. 4.9A). For most models, the formation and location of the super-plume does not depend on whether the *constant-mode* or the *step-mode* is used for the eddy diffusivity. Therefore, the formation of a super-plume on the dayside hemisphere seems to be a robust result. On Earth, volcanic hotspots, such as Hawaii or Iceland are believed to originate from deep mantle plumes (Morgan, 1971). Because Earth's plates move over the relatively immobile mantle plume, the volcanoes will drift away from their plume origin, become inactive and this will then lead to volcanic island chains. 55 Cancri e, however, has a molten (dayside) surface, and it is unclear how the underlying mantle plume on that side would interact with the magma ocean. For this, our simplified approach of modelling the magma ocean by assuming enhanced heat transport through a very high eddy diffusivity becomes limited. At the interface where the solid plume is in contact with the liquid magma ocean, the heat carried by the plume will heat the magma ocean, but on the other hand latent heat will be absorbed when the solids start melting. However, since we do not model in detail the solid-liquid interactions between the magma ocean and the plume, our models do not inform us how for example volcanism on a magma ocean world could look like. A future study could therefore focus on the more local interactions between the solid plume and the magma ocean.

The mega-plume in our model has its origins in the deep interior of the mantle and it forms because of the lower thermal boundary layer instability at the core mantle boundary. The plume will therefore flush the chemical contents of the lower hot thermal boundary layer into the magma ocean (Thompson and Tackley, 1998). If this planet has an enriched reservoir of highly volatile elements (e.g., water, carbon,

nitrogen, sulfur) similar to Earth (e.g., Marty, 2012), then the super-plume would act as a funnel to transport these volatiles into the magma ocean where they would subsequently be outgassed into the atmosphere (e.g., Sossi et al., 2020; Gaillard et al., 2021a).

4.4.3 Convection: Active and passive upwelling

It is still debated, whether plate tectonics on super-Earths is more likely (e.g., Valencia et al., 2007a; van Heck and Tackley, 2011) or less likely (e.g., O'Neill et al., 2007). Here we find that convection is rather sluggish and that convective vigour is greatly reduced by the pressure-dependence of viscosity (Stamenković et al., 2012). On Earth, upwellings can be active or passive. Upwellings below mid-ocean ridges are passive and form because of the pressure decrease when plates are diverging (Schubert et al., 1969). On the other hand, active upwellings (mantle plumes) are rising *actively* once they have accumulated enough buoyancy. On Earth these are expected to be localised beneath volcanic hot spots, such as Hawaii or Iceland. However, they are not actively part of plate tectonics, as opposed to the cold downwellings or slabs which are an integral part of Earth's mantle convection (Bercovici et al., 1989). This means that on Earth, downwellings are active (driven by their own negative buyoancy) and most upwellings are of passive origin. For 55 Cancri e, we find that this pattern is reversed; convection in the mantle of 55 Cancri e is driven by an active mega-plume that rises on the dayside of the planet and cold material is passively subducting on the nightside. The cold material on the nightside is not able however, to accumulate enough buoyancy such that an active downwelling forms. Small-scale downwellings might form on the nightside, but they would not subduct into the deep interior of the mantle.

4.4.4 Observations

The thermal phase curve of 55 Cancri e shows a large offset of the hot spot 41° east of the substellar point (Demory et al., 2016a). For some of our models, (e.g. Fig. 4.8: C1), we see that the super-plume is considerably shifted towards the day-night terminator over the course of several Gyrs. Whether or not this could cause a signal in the thermal phase curve observations (and thereby explain the observed hot

spot shift) is however difficult to say. As soon as the plume interacts with the magma ocean, the temperature inside the magma ocean will equilibrate very quickly on a timescale that is much faster than the dynamics of the plume. Also, the heat flux from the plume will most likely be much smaller than the heat flux that is radiated into space by the dayside magma ocean (a few tens of $\mathrm{mW/m^2}$ vs. $\approx 10^6$ $\mathrm{W/m^2}$). The super-plume will also lose some of its heat before it reaches the magma ocean because of adiabatic decompression and because heat diffuses into the surrounding mantle. Most importantly, however, if the super-plume is able to sample a deep reservoir of 55 Cancri e's mantle, it will transport this material towards the upper layer of the mantle and into the magma ocean, from which it could be outgassed into the atmosphere. For the models where the nightside is not fully molten, the super-plume is preferentially on the dayside of the mantle, and this could therefore lead to a dayside atmosphere that is chemically distinct from the nightside. It has been proposed that SiO that gets outgassed from a magma ocean on the dayside could lead to heterogeneous formation of clouds between the dayside and nightside, possibly explaining the observed hot-spot shift. SiO is expected to be the major Si-bearing gas in the atmospheres of hot volatile-free super-Earths (Schaefer and Fegley, 2009). Schaefer and Fegley (2009) also show that titanium (Ti) and possibly iron (Fe) might be depleted on the dayside because their condensates might be deposited on the nightside, removing them from the magma ocean reservoir. This process is also called trans-atmospheric distillation (Kite et al., 2016): Volatile rock-forming components partition into the atmosphere on the dayside and then get moved towards the nightside through winds, where they condense. Our results show that a super-plume could act as mechanism to re-enrich the magma ocean with species that condensed on the nightside. Whether this process is efficient enough to create a dayside and nightside surface and atmospheric composition that is similar will depend on whether mass recycling between the solid interior and overlaying magma ocean is more efficient than trans-atmospheric distillation (Kite et al., 2016).

For the model with $T_{\mathrm{day}} = 2750\,\mathrm{K}$ and $T_{\mathrm{night}} = 1100\,\mathrm{K}$, the solid mantle on the nightside flows with a velocity $\approx 0.2 - 1\,\mathrm{cm/year}$ and the plume rises with $\approx 2{-}5\,\mathrm{cm/year}$ (rough estimates). Hence, material needs around 1.5 Gyrs to descend into the deep mantle and another 200 Myrs to rise towards the dayside surface.

The timescale for material to get transported from the surface of the nightside towards the dayside surface is therefore on the order of magnitude of Gyrs. This is approximately an order of magnitude higher than for Earth, where the overturn time scale is on the order of 100 Myrs. For 55 Cancri e, trans-atmospheric distillation is expected to be dominant compared to the exchange between the solid mantle and magma ocean (Kite et al., 2016). It is therefore unlikely that the super-plume is able to replenish the dayside surface with material from the nightside if it takes Gyrs to move material from the nightside towards the dayside. For the models with *constant-mode*, where the magma ocean is much thicker on the dayside and the velocities larger because of the higher mantle temperature and lower viscosities, the overturn timescale would only be around $\approx$ 8 Myrs. In this case, the the magma ocean could therefore be efficiently replenished with material from the nightside. However, the models were only run to 15 to 40 Myrs (due to computational resource limits). The models would need to be run for longer to see if the mantle reaches it steady state at this high temperature or if it will be able to cool down more, which would increase viscosity and decrease the mantle velocities.

If the nightside is molten, material can also be transported through horizontal flow from the dayside towards the nightside (Nguyen et al., 2020). In our models, we find that the super-plume does not have a preferred location if the magma ocean covers the whole planet. Therefore, the composition of the atmosphere would be mostly dictated by magma ocean and atmospheric dynamics, because the material that gets advected by the super-plume into the magma ocean will be transported towards the dayside by the magma ocean on timescales that are much faster than the solid dynamics (e.g., Boukaré et al., 2022).

4.4.5 Magma Ocean thickness

Our models show that the magma ocean is not very thick on the dayside (or nightside) if heat transport is only enhanced if the temperature profile inside the magma ocean is super-adiabatic. For these models, the magma ocean thickness on the dayside is around 500 km and 150 to 500 km on the nightside (although for the models with a nightside temperature of 1100 K and dayside temperature of 2600 K it is only partially molten on that side) (Fig. 4.14). The dayside magma ocean becomes much

thicker if heat transport is enhanced regardless of the temperature gradient inside the magma ocean. In that case, the magma ocean has a thickness of roughly 3000 km to 4000 km. K2-141b is a super-Earth ($1.51 R_{\oplus}$, $5.08 M_{\oplus}$, (Malavolta et al., 2018)) that also falls into the category of lava planets. The thermal phase curve observation suggests a day-side temperature around 2050 K and there is no indication of thermal emission from the nightside (Zieba et al., 2022). Boukaré et al. (2022) used thermochemical models to show that the magma ocean depth of this lava planet could extend down to the core-mantle boundary. In our models, we do not observe such deep magma oceans if heat transport is only enhanced if the magma ocean is super-adiabatic. For the case, however, where heat transport is always enhanced, the magma ocean also extends to very large depths. For 55 Cancri e, a magma ocean that extends all the way to the CMB is however unlikely without any other (external or internal) sources of heat. A possible additional heat sources is for example tidal dissipation (Bolmont et al., 2013). Heat dissipation due to induction heating can most likely be excluded for 55 Cancri e as the host star 55 Cancri is a slow rotator with a period around 39 days (Bourrier et al., 2018; Folsom et al., 2020) and therefore most likely does not produce a strong enough magnetic field, thus induction heating is significant (Kislyakova et al., 2017; Kislyakova and Noack, 2020).

4.5 Conclusion

In this study, we used 2D spherical annulus interior convection models to investigate the possible tectonic regimes of super-Earth 55 Cancri e. The thermal phase curve observations of 55 Cancri e suggest that the dayside and possibly even the nightside could harbour a magma ocean. We constrained the surface temperature using the results of general circulation models. We parametrised the magma ocean by enhancing heat transport inside the melt region assuming a very high eddy diffusivity.

Our models show that if the dayside harbours a magma ocean and the nightside is solid or only partially molten, a degree-one convection pattern is established with a super-plume preferentially rising on the dayside and cold material is passively moving into the mantle on the nightside. The return flow of material from the

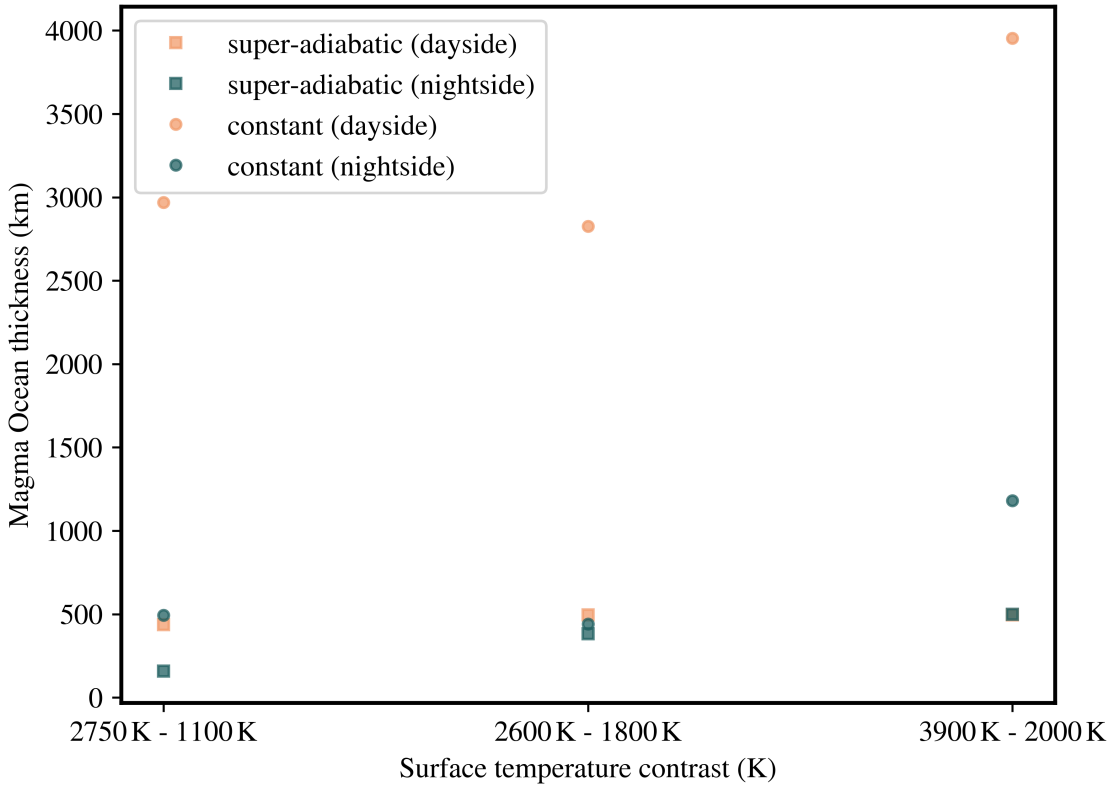

Figure 4.14 | Magma ocean thickness for models with different surface temperature contrasts. The box markers show the thickness for models where heat transport is only enhanced if the temperature gradient inside the magma ocean is super-adiabatic. The round markers show the depth for models where heat transport is always enhanced inside the magma ocean. The magma ocean thickness was determined at 4.6 Gyrs (or at the end of run if the model did not reach that time).

dayside towards the nightside is accommodated in the magma ocean. If both the dayside and nightside are molten, the global magma ocean will tend to equilibrate the temperatures at the interface between the magma ocean and the underlying solid mantle. Therefore, the solid mantle flow is unaffected by the surface temperature contrast and upwellings do not have a preferred location anymore. A degree-2 pattern of flow is also a possible stable convection regime in that case.

We have found that the intense solar insolation from the star leads to a temperature profile inside the magma ocean that is mostly sub-adiabatic. In this case, the magma ocean is most likely not vigorously convecting and is not able to transport heat efficiently into the deep interior. In this case, the (dayside) magma ocean is rather thin ($\approx 500\,\mathrm{km}$). For the models where heat transport is enhanced even if the temperature gradient is not super-adiabatic, the dayside magma ocean thickness can increase significantly (≈ 3000–$4000\,\mathrm{km}$).

If the dayside harbours a magma ocean, the composition of the atmosphere on that hemisphere would be dictated by outgassing from the magma ocean. Atmospheric circulation could transport volatiles from the dayside to the nightside where they could condense (Kite et al., 2016). This could lead to dayside and nightside atmospheres that are chemically distinct. Whether or not the rising plume is able to replenish the magma ocean with material from the nightside depends on the timescales of material transport between the hemispheres and how efficient mass gets recycled between the solid and molten interior.

Chapter 5

Conclusion

5.1 Thesis summary

In this thesis, we used 2D spherical annulus mantle convection models to investigate the interior dynamics of tidally locked super-Earths. More specifically, we investigated the different convection regimes of the bare-rock super-Earth LHS 3844b (Chapter 2), its 'twin-planet' GJ 486b for which it is unknown whether it has an atmosphere or not (Chapter 3), and the lava planet 55 Cancri e (Chapter 4). In the following, we summarise our findings for the different chapters:

5.1.1 Chapter 2: LHS 3844b (page 43)

In this chapter, we investigated the different hemispheric tectonic regimes of super-Earth LHS 3844b which has a radius of approximately 1.3 Earth radii. The thermal phase curve of this planet suggests that the planet is devoid of an atmosphere and tidally locked (Kreidberg et al., 2019). We use the corresponding surface temperature as a boundary condition to model the different convection regimes of LHS 3844b. Our models are either basally heated or include mixed heating (basal + internal heating) and we vary the strength of the lithosphere by employing a plastic yielding criteria. For models with a weak lithosphere, we find that hot plumes are evenly distributed between the dayside and nightside, albeit strong cold downwellings form on the nightside. In contrast, for models with a strong lithosphere we find that a hemispheric tectonic regime is established: The interior dynamics are mostly driven by a prominent downwelling on the dayside which flushes hot material

from the lower thermal boundary layer around the core towards the nightside where plumes preferentially rise. Such a regime is currently absent in the Solar System and our study is the first observationally constrained indication that such a regime could operate on rocky exoplanets.

5.1.2 Chapter 3: GJ 486b (page 63)

Here, we take a closer look at hemispheric tectonics. For this, we investigate the case of super-Earth GJ 486b. This planet can be seen as a 'twin-planet' of LHS 3844b as it has the same radius within the error bounds as LHS 3844b (Trifonov et al., 2021). For this planet, it is not known whether it was able to retain an atmosphere, but it might be the target of future transit and emission spectroscopy. We determine the longitudinal surface temperature for this planet by assuming different efficiencies of heat circulation and using the results of general circulation models. We find that degree-1 convection regimes are possible if the planet has a strong lithosphere independent of the temperature contrast. A strong temperature contrast between the dayside and nightside and overall higher temperatures make hemispheric tectonic more likely. We define hemispheric tectonics as a special case of degree-1 convection, where the cold and viscous downwelling is preferentially pinned to one hemisphere and upwellings are prevalent on the opposite hemisphere.

5.1.3 Chapter 4: 55 Cancri e (page 97)

Here, we examine the possible convection regimes of super-Earth 55 Cancri e that has a radius of approximately 1.8 Earth radii. This planet receives such intense insolation from its host star so that its dayside (and potentially even the nightside) harbours a magma ocean. We parametrise the magma ocean by assuming a very high eddy diffusivity and constrain the surface temperature again with the use of GCMs. For the case where the dayside is molten and the nightside is rocky or partially molten, a degree-1 convection pattern is established with a mega-plume on the dayside and cold material that is passively moving into the interior through mass conservation on the nightside. If both hemispheres are hot enough to harbour a magma ocean, this will tend to equilibrate the temperatures at the interface between the magma ocean and the underlying solid mantle and the plumes do not have a

preferred location anymore. We also show that the temperature profile in the magma ocean is mostly sub-adiabatic and therefore the magma ocean is less likely to be vigorously convecting with limited transport of heat deep into the interior leading to a thin magma ocean.

5.1.4 Overview tectonic regimes

The results of these different studies help us to better understand the different tectonic regimes of rocky super-Earths that are on ultra-short or short period orbits around their host star. We have shown that tidally locked super-Earths could exhibit tectonic regimes that are unlike anything we observe currently in the Solar System. The different regimes that we found are:

- **Uniform regime** with downwellings and upwellings uniformly distributed. Downwellings on the nightside can be stronger (colder and more viscous) if the planet has a strong surface temperature contrast between the dayside and nightside.

- **Hemispheric tectonics**: The interior mantle flow is dominated by a strong cold downwelling on one hemisphere and upwellings are getting flushed around the CMB towards the other side where they rise towards the surface. The downwelling that is dominating this flow pattern has a preferred location.

- **Degree-1 convection**: The mantle flow is also dominated by a strong cold downwelling which pushes upwellings towards the other side, but contrary to a hemispheric tectonic regime, the downwelling does not have a preferred location.

- **Degree-1 convection with dayside magma ocean**: In this regime, the dayside of the planet harbours a magma ocean and the mantle flow is dominated by a mega-plume on the dayside. Cold material is moving passively into the mantle on the nightside.

- **Uniform regime with global magma ocean**: In this regime, both the dayside and nightside surface are molten. Therefore, temperatures at the interface between the magma ocean and the underlying solid mantle get equilibrated

and the solid mantle flow is unaffected by a possible strong surface temperature contrast. Plumes in the mantle have no preferred location and a degree-2 pattern of flow (with plumes located at the substellar and antistellar point) is also a stable configuration.

5.2 Outlook

Our models suggest a range of different tectonic regimes that could operate on (tidally locked) rocky exoplanets and the goal of future studies should now be to understand how we can distinguish between these different tectonic regimes by means of astronomical observations.

For our models of LHS 3844b and 55 Cancri e we constrained the surface or radiative temperature of a planet through thermal phase curve observations. For LHS 3844b, we found that the thermal contribution from the interior on the nightside will not lead to detectable spectral signatures in the thermal phase curve (see Section 2.4.2), and on the dayside it would be extremely challenging to differentiate the thermal contribution from the reflected, and absorbed and re-radiated light. On the nightside, upwellings could lead to massive outpourings of melt that could potentially imprint themselves in the observed transit depth (Kipping and Tinetti, 2010) or multi-wavelength phase curve observations. Melting processes can be modelled using tracers in the flow field that track the evolving melt and solid composition. This could provide insights into the longitudinal variation of melt generation and crustal production at the surface of rocky tidally locked super-Earths, which will help to understand future observations.

To investigate this, a future study could include (tracer-based) melting to the models we have run for LHS 3844b and examine the longitudinal variation of melt generation at the surface of LHS 3844b or other rocky tidally locked super-Earths.

For 55 Cancri e, recent observations suggest phase modulations in its phase curve observations, and an explanation for this is still lacking (e.g. Sulis et al., 2019; Morris et al., 2021; Valdés et al., 2022). An interesting study direction could therefore also be to investigate whether hemispheric tectonics or degree-1 convection could lead to time-dependent variability in the phase curve observations. For this, it is also

important to investigate how the interior interacts with a potential atmosphere on rocky exoplanets. A planet's atmosphere is inherently related to its interior through long-term volatile cycling. Previous studies have focussed on modelling volcanism and outgassing on stagnant lid planets and found that outgassing rates can depend on several factors such as planet size, core-mass-fraction (Noack et al., 2017), thermodynamic parameters such as radioactive heating (Dorn et al., 2018b) or the redox state the mantle (Ortenzi et al., 2020; Guimond et al., 2021). (Liggins et al., 2022) have shown that observations of the chemical speciation of volcanic atmospheres of rocky exoplanets can give insights into the redox state of the mantle (oxidised, reduced or intermediate state).

Outgassing and volcanism on rocky exoplanets with possible hemispheric tectonics has not yet been explored. By combining interior dynamics with an outgassing model, one could investigate potential atmospheres on rocky exoplanets in terms of their composition, thickness, and evolution. This could also help to understand future observations that aim to probe the atmospheres of rocky exoplanets through transit, reflection or emission spectroscopy. In fact, JWST will target LHS 3844b in order to search for trace amounts of sulfur dioxide that could arise from volcanic outgassing (Kreidberg et al., 2021). JWST will also target super-Earth 55 Cancri e, in order to examine whether this planet has a thick volatile-rich atmosphere or a molten surface with a thin silicate vapour atmosphere (Hu et al., 2021). 55 Cancri e will likely also be the target of future CHEOPS observations (Morris et al., 2021). It is therefore timely to study the coupling between interior dynamics and atmospheres of tidally locked super-Earths, as this will help us understand future astronomical observations.

So far, the thermal phase curves of 3 different rocky super-Earths have been observed. Namely, those of 55 Cancri e (Demory et al., 2016a), LHS 3844b (Kreidberg et al., 2019), and K2-141b (Zieba et al., 2022). In Chapter 4, we have addressed the interior dynamics of 55 Cancri e, and in Chapter 2 the case of super-Earth LHS 3844b. Super-Earth K2-141b is also a promising target for a future study investigating its interior dynamics. K2-141b is an ultra-short-period super-Earth that also falls into the category of lava planets. It has a radius of $1.51 R_{\oplus}$ and a mass of $5.08 M_{\oplus}$ (Malavolta et al., 2018). Its thermal phase curve observation suggests a

dayside temperature of 2049 K and a nightside temperature that is consistent with zero (Zieba et al., 2022). It is therefore likely that K2-141b harbours a magma ocean on the dayside and has a rocky nightside surface with only a thin atmosphere. This could lead to tectonic regimes that we have not captured yet with our studies of LHS 3844b, Gliese 486b, and 55 Cancri e. A study of K2-141b's interior is also timely as upcoming JWST observations will search for signatures of volcanism and/or vaporised rock such as SiO on this super-Earth (Dang et al., 2021; Espinoza et al., 2021).

If the magma ocean remains molten over extended periods of time because of solar insolation, there will be chemical equilibrium between the planet's atmosphere and magma ocean and the redox conditions of the planet will control the composition of the outgassed atmosphere (e.g., Hirschmann, 2012; Sossi et al., 2020; Gaillard et al., 2021b). Observations of exoplanet atmospheres can therefore inform us about the oxidation state of the magma ocean. It has also been shown that the speciation of the atmosphere depends on the convective vigour of the magma ocean, and atmospheric observations can therefore be used to constrain magma ocean dynamics (Lichtenberg, 2021).

At greater depths, the magma ocean will solidify and there will be (chemical and physical) interactions with the underlying solid mantle. This is where our approximation of modelling the magma ocean by assuming a very high Eddy diffusivity becomes limited. In the mixed phase region, our model is not able to capture all the complexity of a multiphase system consisting of solid, liquid and gas. At this interface, material (e.g., FeO) will be exchanged because of fractional crystallisation, which can have important consequences for mantle and magma ocean evolution (e.g., Bolrão et al., 2021). Also, at intermediate melt fractions ($0.2 < \phi < 0.4$), the heat flux caused by rapid gravitational separation between the melt and solid could also play an important role (Abe, 1997). This effect could be captured with the help of a semi-analytical model where the heat flow due to gravitational separation is parametrised depending on the melt fraction (Bower et al., 2018). However, this is most likely more important for transient magma ocean stages where the rheological front is continuously changing and therefore causes solid-melt separation. In our work, where we look at steady state magma oceans, it is therefore reasonable to

neglect this effect as a first approximation since the mixed phase region does not change significantly over time. A future study could also look into the dynamic effects of plumes (or super-plumes) that impinge into an overlying magma ocean. At the CMB, deviatoric stresses caused by cold mantle downwellings could cause a suction effect that can also lead to an exchange of material between the mantle and the core (Kanda and Stevenson, 2006).

In this work, we used 2D numerical models to investigate the interior dynamics of rocky super-Earths. However, rocky super-Earths are inherently 3D objects. 3D features of mantle convection, such as linear slabs or quasi-cylindrical plumes can therefore not be captured by running 2D models (e.g., Bercovici et al., 1989). 3D models at high Rayleigh number that are heated from below or that include internal heating will become time dependent and might lead to asymmetric modes of convection (e.g., Schubert et al., 2001; Travis et al., 1990; Bercovici et al., 1989). A future study could therefore investigate whether the different convection patterns that we found for tidally locked super-Earths are affected by 3D geometry.

Last but not least, there are still large uncertainties regarding the rheology of super-Earths. In this work, we used the lower-bound post-perovskite rheology from (Tackley et al., 2013). As a follow-up study, one could investigate the case of the higher-bound post-perovskite. Umemoto et al. (2006) have run first-principle computations to show that post-perovskite could dissociate into MgO + SiO_2 at pressures above 1000 GPa and therefore also influence the convection inside super-Earths. Coppari et al. (2021) investigated the atomic structure and density of FeO up to 700 GPa and reveal complex stratification and rheology. The B1-FeO to B2-FeO phase transition might lead to an important viscosity reduction that could have consequences for deep mantle dynamics. The influence of such stratifications and complex rheology on the possible convection regimes inside super-Earths has not yet been studied. Also, many super-Earths might have interiors that are not Earth-like. For example, it has been shown that 55 Cancri e might have no core and be enriched in Ca and Al rich minerals (Dorn et al., 2018a). Future studies could therefore look into how such interior compositions affect the interior dynamics. More recent high-pressure and high-temperature experiments, will also help in further improving the melting curves and density profiles for super-Earth planets (e.g., Duffy and Smith,

2019; Fei et al., 2021).

In this thesis, we were able—for the first time—to use astronomical observations to constrain geodynamic models of mantle flow of rocky exoplanets and our work therefore presents an important step towards unravelling the interior dynamics of rocky exoplanets. Current and near-future space observations such as CHEOPS, JWST, ARIEL and many more will revolutionise our understanding of rocky exoplanets. A major objective of exoplanet science is to detect habitability on a planet outside of our Solar System, and it is therefore important to understand what tectonic regimes such planets might exhibit, as these will influence potential atmospheres and the surface conditions on these distant worlds.

Acknowledgements

This thesis would not have been possible without the support of many people. Here, I would like to use the opportunity to thank them.

To Dan J. Bower, for supporting and guiding me during the last 4 years. You shaped me as a scientist, and always had an open door (or zoom call) if I was stuck on a problem. I am extremely grateful to have had you as my PhD supervisor.

To Gregor Golabek, for evaluating my thesis and providing invaluable feedback.

To Christoph Mordasini, for chairing my PhD defence.

To Paul J. Tackley, for your invaluable support and help with StagYY and helping me with my geodynamics questions.

To Tim Lichtenberg, for the great collaboration, exciting project ideas, and help with paper and proposal writing during the last few years.

To Brice-Olivier Demory, for all the help with linking my thesis to observations.

To Danielle Zemp and Irene Leder, for your help with all the administrative paperwork and reimbursements.

To the whole Geonode, Dan, Kausthubh, Paolo, Meng, and Noah. For all the inspiring scientific (and non-scientific) discussions. For teaching me a lot of useful trivia knowledge about the Bremgarten F1 loop on a three hour walk. Who knew how exciting a walk along the industrial road of Bern could be.

To the TAPS and EXOCLIME groups, for inviting me to your group meetings.

To Office202, Beatrice, Harry, Erik and Marko. It was an honour to share an office with all of you. Thank you Marko for not leaving us without coffee after you left the office. Thank you, Beatrice, for being such a great desk neighbour. Thank you, Harry, for regularly kicking me with your very long feet. Thank you, Erik, for showing me how nice Tequila and Whiskey can actually be.

To Iris, for convincing me to become a part of the great blog editing team.

To Kar Wai, for the help and support with all the melting and time step problems.

To Thibaut, for creating an amazing illustration and for the car rides and ice tea discussions.

To the Tödi-Cup committee, Raffael, Stefan and Kevin. For always making sure we had a fantastic start to the New Year.

To the Spass-Group, Rhea, Valentin, Mario and Kevin, for fantastic Spass-evenings. Looking forward to preparing a risotto for you in Oxford!

To Silvan and Isabella, for inviting me every year to an amazing week of skiing in Adelboden.

To Marius, for enduring my Kafi am Pischterand and for constantly reminding me that I haven't detected an exoplanet yet.

To Igor, for the amazing arena sessions, and the great ping pong matches.

To all the Triple-T hikers. The real treasure was the friends we made along all these hikes.

To Nicolas, for organising many flunky-ball games.

To Andrin, for your dedication at the Triple-T party.

To Daniel, for being the best Triple-T hiker and the Kitzking. Your cakes are amazing.

To Hugh and Maeva, for the amazing boat trip.

To Jesse, for maybe taking over the heavy duty of being a Triple-T (JWST) leader.

To Matthew, for reminding me I should do the right thing. Next time, choose the right arena.

To Beatrice, for the memorable Octoberfest and concert evenings.

To Marit, for the many flat evenings, balkonien and introducing me to Sinter-Klaas. For a memorable documentary of Falera.

To Sabina, for always making sure I don't forget again my keys, bag, and phone after your flat parties.

To Oli and Jo Ann, for helping me in defending the great canton of Aargau.

To Erik, for our shared love for 55 Cancri e.

To Anna and Manuel, for inspiring house Ascendor with your hiking speed.

To Marko, for all the memorable Marko-moments.

To Clémence, for reading through my proposal, and the intense tennis matches. One day, I hope to be as good in tennis as you are.

To Chloe, for helping me with my proposal, all the PhD registration stuff, and so much more. Looking forward to many more hikes, ski trips, boat trips and pub crawls.

To Harry, for always flipping the coin in your favour. It was an honour to share many conference accommodations with you and to take care of your snake and cat. Also thank you for inspiring me to use Copernicus and many more famous citations in my thesis introduction.

To Kathryn, no words needed. Thank you for always being there for me.

To my parents, my brother Felix, and my sister Regula, for your endless support and love. Without you, I would never be where I am now and for this, I will be forever grateful.

Bibliography

Y. Abe. Physical state of the very early Earth. *Lithos*, 30(3):223–235, Sept. 1993. ISSN 0024-4937. doi: 10.1016/0024-4937(93)90037-D. URL https://www.sciencedirect.com/science/article/pii/002449379390037D.

Y. Abe. Thermal and chemical evolution of the terrestrial magma ocean. *Physics of the Earth and Planetary Interiors*, 1:41–54, 1997.

C. Alcock, W. H. Allen, R. A. Allsman, D. Alves, T. S. Axelrod, T. S. Banks, S. F. Beaulieu, A. C. Becker, R. H. Becker, D. P. Bennett, I. A. Bond, B. S. Carter, K. H. Cook, R. J. Dodd, K. C. Freeman, M. D. Gregg, K. Griest, J. B. Hearnshaw, A. Heller, M. Honda, J. Jugaku, S. Kabe, S. Kaspi, P. M. Kilmartin, A. Kitamura, O. Kovo, M. J. Lehner, T. E. Love, D. Maoz, S. L. Marshall, Y. Matsubara, D. Minniti, M. Miyamoto, J. A. Morse, Y. Muraki, T. Nakamura, B. A. Peterson, M. M. Phillips, M. R. Pratt, P. J. Quinn, I. N. Reid, M. Reid, D. Reiss, A. Retter, A. W. Rodgers, W. L. W. Sargent, H. Sato, M. Sekiguchi, P. B. Stetson, C. W. Stubbs, D. J. Sullivan, W. Sutherland, A. Tomaney, T. Vandehei, Y. Watase, D. L. Welch, T. Yanagisawa, M. Yoshizawa, and P. C. M. Y. and. MACHO Alert 95-30: First Real-Time Observation of Extended Source Effects in Gravitational Microlensing. *The Astrophysical Journal*, 491(2):436–450, Dec. 1997. ISSN 0004-637X. doi: 10.1086/304974. URL https://doi.org/10.1086/304974.

M. W. Ammann, J. P. Brodholt, and D. P. Dobson. DFT study of migration enthalpies in $MgSiO_3$ perovskite. *Physics and Chemistry of Minerals*, 36(3):151–158, 2009. ISSN 03421791. doi: 10.1007/s00269-008-0265-z.

D. L. Anderson. Earth's Viscosity. *Science*, 151(3708):321–322, Jan. 1966. doi: 10.1126/science.151.3708.321. URL https://www.science.org/doi/10.1126/science.151.3708.321.

D. Andrault, N. Bolfan-Casanova, G. L. Nigro, M. A. Bouhifd, G. Garbarino, and M. Mezouar. Solidus and liquidus profiles of chondritic mantle: Implication for melting of the Earth across its history. *Earth and Planetary Science Letters*, 304(1):251–259, Apr. 2011. ISSN 0012-821X. doi: 10.1016/j.epsl.2011.02.006. URL https://www.sciencedirect.com/science/article/pii/S0012821X1100077X.

W. Benz, W. L. Slattery, and A. G. W. Cameron. Collisional stripping of Mercury's mantle. *Icarus*, 74(3):516–528, June 1988. ISSN 0019-1035. doi: 10.1016/0019-1035(88)90118-2. URL https://www.sciencedirect.com/science/article/pii/0019103588901182.

D. Bercovici, G. Schubert, and G. A. Glatzmaier. Three-Dimensional Spherical Models of Convection in the Earth's Mantle. *Science (New York, N.Y.)*, 244 (4907):950–955, May 1989. ISSN 0036-8075. doi: 10.1126/science.244.4907.950.

F. Birch. Energetics of core formation. *Journal of Geophysical Research (1896-1977)*, 70(24):6217–6221, 1965. ISSN 2156-2202. doi: 10.1029/JZ070i024p06217. URL https://onlinelibrary.wiley.com/doi/abs/10.1029/JZ070i024p06217.

B. A. Black and S. A. Gibson. Deep Carbon and the Life Cycle of Large Igneous Provinces. *Elements*, 15(5):319–324, Oct. 2019. ISSN 1811-5209. doi: 10.2138/gselements.15.5.319. URL https://doi.org/10.2138/gselements.15.5.319.

E. Bolmont, F. Selsis, S. N. Raymond, J. Leconte, F. Hersant, A.-S. Maurin, and J. Pericaud. Tidal dissipation and eccentricity pumping: Implications for the depth of the secondary eclipse of 55 cancri e. *Astronomy and Astrophysics*, 556: A17, Aug. 2013. ISSN 0004-6361. doi: 10.1051/0004-6361/201220837. URL https://ui.adsabs.harvard.edu/abs/2013A&A...556A..17B.

E. Bolmont, S. N. Breton, G. Tobie, C. Dumoulin, S. Mathis, and O. Grasset. Solid tidal friction in multi-layer planets: Application to Earth, Venus, a Super Earth and the TRAPPIST-1 planets. Can a multi-layer planet be approximated as a homogeneous planet? *Astronomy and Astrophysics*, Oct. 2020. URL http://arxiv.org/abs/2010.04587. arXiv: 2010.04587.

D. P. Bolrão, M. D. Ballmer, A. Morison, A. B. Rozel, P. Sanan, S. Labrosse, and P. J. Tackley. Timescales of chemical equilibrium between the convecting solid mantle and over- and underlying magma oceans. *Solid Earth*, 12(2):421–437, Feb. 2021. ISSN 1869-9510. doi: 10.5194/se-12-421-2021. URL https://se.copernicus.org/articles/12/421/2021/.

I. A. Bond. The first extrasolar planet detected via gravitational microlensing. *New Astronomy Reviews*, 56(1):25–32, Jan. 2012. ISSN 1387-6473. doi: 10.1016/j.newar.2011.06.004. URL https://www.sciencedirect.com/science/article/pii/S1387647311000431.

Y. Bottinga and C. J. Allegre. Thermal aspects of sea-floor spreading and the nature of the oceanic crust. *Tectonophysics*, 18(1):1–17, June 1973. ISSN 0040-1951. doi: 10.1016/0040-1951(73)90075-9. URL https://www.sciencedirect.com/science/article/pii/0040195173900759.

C.-É. Boukaré, N. B. Cowan, and J. Badro. Deep two-phase, hemispherical magma oceans on lava planets. May 2022. doi: 10.48550/arXiv.2205.02864. URL http://arxiv.org/abs/2205.02864. arXiv:2205.02864 [astro-ph, physics:physics] type: article.

V. Bourrier, X. Dumusque, C. Dorn, G. W. Henry, N. Astudillo-Defru, J. Rey, B. Benneke, G. Hébrard, C. Lovis, B. O. Demory, C. Moutou, and D. Ehrenreich. The 55 Cancri system reassessed. *Astronomy & Astrophysics*, 619:A1, Nov. 2018. ISSN 0004-6361, 1432-0746. doi: 10.1051/0004-6361/201833154. URL https://www.aanda.org/articles/aa/abs/2018/11/aa33154-18/aa33154-18.html.

D. J. Bower, P. Sanan, and A. S. Wolf. Numerical solution of a non-linear conservation law applicable to the interior dynamics of partially molten planets. *Physics of the Earth and Planetary Interiors*, 274(November 2017):49–62, 2018. ISSN 00319201. doi: 10.1016/j.pepi.2017.11.004.

D. J. Bower, D. Kitzmann, A. S. Wolf, P. Sanan, C. Dorn, and A. V. Oza. Linking the evolution of terrestrial interiors and an early outgassed atmosphere to astrophysical observations. *Astronomy and Astrophysics*, 631:A103, Nov. 2019. ISSN 0004-6361. URL https://ui.adsabs.harvard.edu/abs/2019A&A...631A.103B.

B. A. Buffett. Earth's core and the geodynamo. *Science*, 288(5473):2007–2012, 2000. doi: 10.1126/science.288.5473.2007. URL https://www.science.org/doi/abs/10.1126/science.288.5473.2007.

J. Byerlee. Friction of rocks. *pure and applied geophysics*, 116(4):615–626, July 1978. ISSN 1420-9136. doi: 10.1007/BF00876528. URL https://doi.org/10.1007/BF00876528.

P. K. Byrne, C. Klimczak, A. M. Celâl Şengör, S. C. Solomon, T. R. Watters, and I. I. Hauck. Mercury's global contraction much greater than earlier estimates. *Nature Geoscience*, 7(4):301–307, Apr. 2014. ISSN 1752-0908. doi: 10.1038/ngeo2097. URL https://www.nature.com/articles/ngeo2097.

P. K. Byrne, J. L. Whitten, C. Klimczak, F. M. McCubbin, and L. R. Ostrach. The Volcanic Character of Mercury. Cambridge Planetary Science, pages 287–323. Cambridge University Press, Cambridge, 2018. ISBN 9781107154452. doi: 10.1017/9781316650684.012. URL https://www.cambridge.org/core/books/mercury/volcanic-character-of-mercury/48272AE42A06B8D501057C10CC3890EE.

P. K. Byrne, B. J. Foley, M. E. S. Violay, M. J. Heap, and S. Mikhail. The Effects of Planetary and Stellar Parameters on Brittle Lithospheric Thickness. *Journal of Geophysical Research: Planets*, 126(11):e2021JE006952, 2021. ISSN 2169-9100. doi: 10.1029/2021JE006952. URL https://onlinelibrary.wiley.com/doi/abs/10.1029/2021JE006952.

R. M. Canup and E. Asphaug. Origin of the Moon in a giant impact near the end of the Earth's formation. *Nature*, 412(6848):708–712, Aug. 2001. ISSN 0028-0836. doi: 10.1038/35089010.

L. Caricchi, L. Burlini, P. Ulmer, T. Gerya, M. Vassalli, and P. Papale. Non-Newtonian rheology of crystal-bearing magmas and implications for magma ascent dynamics. *Earth and Planetary Science Letters*, 264(3):402–419, Dec. 2007. ISSN 0012-821X. doi: 10.1016/j.epsl.2007.09.032. URL https://www.sciencedirect.com/science/article/pii/S0012821X07005985.

M. H. Carr, H. Masursky, R. G. Strom, and R. J. Terrile. Volcanic features of Io. *Nature*, 280(5725):729–733, Aug. 1979. ISSN 1476-4687. doi: 10.1038/280729a0. URL https://www.nature.com/articles/280729a0.

M. H. Carr, M. J. S. Belton, C. R. Chapman, M. E. Davies, P. Geissler, R. Greenberg, A. S. McEwen, B. R. Tufts, R. Greeley, R. Sullivan, J. W. Head, R. T. Pappalardo, K. P. Klaasen, T. V. Johnson, J. Kaufman, D. Senske, J. Moore, G. Neukum, G. Schubert, J. A. Burns, P. Thomas, and J. Veverka. Evidence for a subsurface ocean on Europa. *Nature*, 391(6665):363–365, Jan. 1998. ISSN 1476-4687. doi: 10.1038/34857. URL https://www.nature.com/articles/34857.

K.-H. Chao, R. deGraffenried, M. Lach, W. Nelson, K. Truax, and E. Gaidos. Lava Worlds: From Early Earth to Exoplanets. *Geochemistry*, page 125735, Jan. 2021. ISSN 0009-2819. doi: 10.1016/j.chemer.2020.125735. URL http://www.sciencedirect.com/science/article/pii/S000928192030146X.

D. Charbonneau, T. M. Brown, D. W. Latham, and M. Mayor. Detection of Planetary Transits Across a Sun-like Star. *The Astrophysical Journal*, 529 (1):L45–L48, Jan. 2000. ISSN 0004637X. doi: 10.1086/312457. URL http://arxiv.org/abs/astro-ph/9911436. arXiv:astro-ph/9911436.

D. Charbonneau, T. M. Brown, R. W. Noyes, and R. L. Gilliland. Detection of an extrasolar planet atmosphere. *The Astrophysical Journal*, 568(1):377–384, mar 2002. doi: 10.1086/338770. URL https://doi.org/10.1086/338770.

D. Charbonneau, L. E. Allen, S. T. Megeath, G. Torres, R. Alonso, T. M. Brown, R. L. Gilliland, D. W. Latham, G. Mandushev, F. T. O'Donovan, and A. Sozzetti. Detection of Thermal Emission from an Extrasolar Planet. *The Astrophysical Journal*, 626(1):523, June 2005. ISSN 0004-637X. doi: 10.1086/429991. URL https://iopscience.iop.org/article/10.1086/429991/meta.

G. Chauvin, A.-M. Lagrange, B. Zuckerman, C. Dumas, D. Mouillet, I. Song, J.-L. Beuzit, P. Lowrance, and M. S. Bessell. A companion to AB Pic at the planet/brown dwarf boundary. *Astronomy & Astrophysics*, 438(3):L29–L32, Aug. 2005. ISSN 0004-6361, 1432-0746. doi: 10.1051/0004-6361:200500111. URL http://arxiv.org/abs/astro-ph/0504658. arXiv:astro-ph/0504658.

J. Y.-K. Cho, K. Menou, B. M. S. Hansen, and S. Seager. The Changing Face of the Extrasolar Giant Planet HD 209458b. *The Astrophysical Journal*, 587(2):L117, Mar. 2003. ISSN 0004-637X. doi: 10.1086/375016. URL https://iopscience.iop.org/article/10.1086/375016/meta.

U. Christensen. Convection with pressure- and temperature-dependent non-Newtonian rheology. *Geophysical Journal International*, 77(2):343–384, May 1984. ISSN 0956-540X. doi: 10.1111/j.1365-246X.1984.tb01939.x. URL https://doi.org/10.1111/j.1365-246X.1984.tb01939.x.

R. I. Citron, M. Manga, and E. Tan. A hybrid origin of the Martian crustal dichotomy: Degree-1 convection antipodal to a giant impact. *Earth and Planetary Science Letters*, 491:58–66, June 2018. ISSN 0012-821X. doi: 10.1016/j.epsl.2018.03.031. URL https://www.sciencedirect.com/science/article/pii/S0012821X18301559.

M. F. Coffin and O. Eldholm. Large igneous provinces: Crustal structure, dimensions, and external consequences. *Reviews of Geophysics*, 32(1):1–36, 1994. ISSN 1944-9208. doi: 10.1029/93RG02508. URL https://onlinelibrary.wiley.com/doi/abs/10.1029/93RG02508.

C. P. Conrad and C. Lithgow-Bertelloni. How Mantle Slabs Drive Plate Tectonics. *Science*, 298(5591):207–209, Oct. 2002. doi: 10.1126/science.1074161. URL https://www.science.org/doi/10.1126/science.1074161.

N. Copernicus. De revolutionibus orbium coelestium. 1543. doi: 10.1515/9783486776515.

F. Coppari, R. F. Smith, J. Wang, M. Millot, D. Kim, J. R. Rygg, S. Hamel, J. H. Eggert, and T. S. Duffy. Implications of the iron oxide phase transition on the interiors of rocky exoplanets. *Nature Geoscience*, 14(3):121–126, Mar. 2021. ISSN 1752-0908. doi: 10.1038/s41561-020-00684-y. URL https://www.nature.com/articles/s41561-020-00684-y.

A. Costa, L. Caricchi, and N. Bagdassar. A model for rheology of particle-bearing suspensions and partially molten rocks. *Geochemistry Geophysics Geosystems - GEOCHEM GEOPHYS GEOSYST*, 10, Mar. 2009. doi: 10.1029/2008GC002138.

A. Crida, R. Ligi, C. Dorn, F. Borsa, and Y. Lebreton. Mass, radius, and composition of the transiting planet 55 Cnc e : using interferometry and correlations — A quick update. *Research Notes of the AAS*, 2(3):172, Sept. 2018. ISSN 2515-5172. doi: 10.3847/2515-5172/aae1f6. URL http://arxiv.org/abs/1809.08008. arXiv: 1809.08008.

T. Currie, B. Biller, A.-M. Lagrange, C. Marois, O. Guyon, E. Nielsen, M. Bonnefoy, and R. De Rosa. Direct Imaging and Spectroscopy of Extrasolar Planets. Technical report, May 2022. URL http://arxiv.org/abs/2205.05696. arXiv:2205.05696 [astro-ph] type: article.

L. Dang, N. B. Cowan, L. Kreidberg, S. Zieba, R. Pierrehumbert, M. Hammond, G. Nguyen, R. Lupu, Y. Miguel, and M. Zilinskas. Jwst proposal 2347: A hell of a phase curve: Mapping the surface and atmosphere of a lava planet k2-141. JWST Proposal, Cycle 1, 2021. URL https://www.stsci.edu/jwst/science-execution/program-information.html?id=2347.

V. Dehant, V. Debaille, V. Dobos, F. Gaillard, C. Gillmann, S. Goderis, J. L. Grenfell, D. Höning, E. J. Javaux, Ö. Karatekin, A. Morbidelli, L. Noack, H. Rauer, M. Scherf, T. Spohn, P. Tackley, T. Van Hoolst, and K. Wünnemann. Geoscience for understanding habitability in the solar system and beyond. *Space Science Reviews*, 215(6):42, 2019. ISSN 1572-9672. doi: 10.1007/s11214-019-0608-8. URL https://doi.org/10.1007/s11214-019-0608-8.

B.-O. Demory, M. Gillon, S. Seager, B. Benneke, D. Deming, and B. Jackson. Detection of thermal emission from a super-earth. *The Astrophysical Journal*, 751 (2):L28, May 2012. ISSN 2041-8205. doi: 10.1088/2041-8205/751/2/L28. URL https://doi.org/10.1088/2041-8205/751/2/l28.

B.-O. Demory, J. d. Wit, N. Lewis, J. Fortney, A. Zsom, S. Seager, H. Knutson, K. Heng, N. Madhusudhan, M. Gillon, T. Barclay, J.-M. Desert, V. Parmentier, and N. B. Cowan. Inference of inhomogeneous clouds in an exoplanet atmosphere. *The Astrophysical Journal*, 776(2):L25, Oct. 2013. ISSN 2041-8205. doi: 10.1088/2041-8205/776/2/L25. URL https://doi.org/10.1088/2041-8205/776/2/l25.

B. O. Demory, M. Gillon, J. De Wit, N. Madhusudhan, E. Bolmont, K. Heng,

T. Kataria, N. Lewis, R. Hu, J. Krick, V. Stamenković, B. Benneke, S. Kane, and D. Queloz. A map of the large day-night temperature gradient of a super-Earth exoplanet. *Nature*, 532(7598):207–209, 2016a. ISSN 14764687. doi: 10.1038/nature17169. URL http://dx.doi.org/10.1038/nature17169.

B. O. Demory, M. Gillon, N. Madhusudhan, and D. Queloz. Variability in the super-Earth 55 Cnc e. *Monthly Notices of the Royal Astronomical Society*, 455 (2):2018–2027, 2016b. ISSN 13652966. doi: 10.1093/mnras/stv2239.

J. DePaolo Donald and M. Michael. Deep origin of hotspots–the mantle plume model. *Science*, 300(5621):920–921, May 2003. doi: 10.1126/science.1083623. URL https://doi.org/10.1126/science.1083623.

C. Dorn, J. H. D. Harrison, A. Bonsor, and T. Hands. A new class of Super-Earths formed from high-temperature condensates : HD219134 b , 55 Cnc e , WASP-47 e. *Monthly Notices of the Royal Astronomical Society*, 16(October):1–16, 2018a. doi: 10.1093/mnras/sty3435.

C. Dorn, L. Noack, and A. Rozel. Outgassing on stagnant-lid super-Earths. *Astronomy & Astrophysics*, 614:A18, June 2018b. ISSN 0004-6361, 1432-0746. doi: 10.1051/0004-6361/201731513. URL http://arxiv.org/abs/1802.09264. arXiv: 1802.09264.

T. S. Duffy and R. F. Smith. Ultra-High Pressure Dynamic Compression of Geological Materials. *Frontiers in Earth Science*, 7, 2019. ISSN 2296-6463. URL https://www.frontiersin.org/articles/10.3389/feart.2019.00023.

S. T. Dye. Geoneutrinos and the radioactive power of the Earth. *Reviews of Geophysics*, 50(3), 2012. ISSN 1944-9208. doi: 10.1029/2012RG000400. URL https://onlinelibrary.wiley.com/doi/abs/10.1029/2012RG000400.

A. Einstein. Lens-like action of a star by the deviation of light in the gravitational field. *Science*, 84(2188):506–507, 1936. doi: 10.1126/science.84.2188.506. URL https://www.science.org/doi/abs/10.1126/science.84.2188.506.

L. T. Elkins-Tanton. Magma Oceans in the Inner Solar System. *Annual Review of Earth and Planetary Sciences*, 40(1):113–139, 2012. ISSN 0084-6597. doi:

10.1146/annurev-earth-042711-105503. URL http://www.annualreviews.org/doi/10.1146/annurev-earth-042711-105503.

N. Espinoza and K. Jones. Constraining mornings & evenings on distant worlds: a new semi-analytical approach and prospects with transmission spectroscopy. *The Astronomical Journal*, 162(4):165, Oct. 2021. ISSN 0004-6256, 1538-3881. doi: 10.3847/1538-3881/ac134d. URL http://arxiv.org/abs/2106.15687. arXiv:2106.15687 [astro-ph].

N. Espinoza, M. Malik, L. A. Buchhave, J. Hoeijmakers, M. Lopez-Morales, J. M. Mendonca, A. Bello-Arufe, H. Diamond-Lowe, N. Gibson, A. Rathcke, A. Mesa Guzman, D. Kitzmann, M. Hooton, B. M. Morris, C. Fisher, A. J. Burgasser, T. Kozakis, K. Heng, B.-O. Demory, Y. Miguel, and R. Hu. Jwst proposal 2159: The first near-infrared spectroscopic phase-curve of a super-earth. JWST Prposal, Cycle 1, 2021. URL https://www.stsci.edu/jwst/science-execution/program-information.html?id=2159.

Y. Fei, C. T. Seagle, J. P. Townsend, C. A. McCoy, A. Boujibar, P. Driscoll, L. Shulenburger, and M. D. Furnish. Melting and density of MgSiO3 determined by shock compression of bridgmanite to 1254GPa. *Nature Communications*, 12 (1):876, Feb. 2021. ISSN 2041-1723. doi: 10.1038/s41467-021-21170-y. URL https://www.nature.com/articles/s41467-021-21170-y.

B. J. Foley and P. E. Driscoll. Whole planet coupling between climate, mantle, and core: Implications for the evolution of rocky planets. *Geochemistry, Geophysics, Geosystems*, 17(5):1885–1914, May 2016. ISSN 15252027. doi: 10.1002/2015GC006210. URL http://arxiv.org/abs/1711.06801. arXiv: 1711.06801.

C. P. Folsom, D. Ó Fionnagáin, L. Fossati, A. A. Vidotto, C. Moutou, P. Petit, D. Dragomir, and J. F. Donati. Circumstellar environment of 55 Cancri. The super-Earth 55 Cnc e as a primary target for star-planet interactions. *Astronomy & Astrophysics*, 633:A48, Jan. 2020. doi: 10.1051/0004-6361/201937186.

F. Forget and R. T. Pierrehumbert. Warming Early Mars with Carbon Dioxide Clouds That Scatter Infrared Radiation. *Science*, 278(5341):1273–1276, Nov.

1997. doi: 10.1126/science.278.5341.1273. URL https://www.science.org/doi/10.1126/science.278.5341.1273.

D. Forsyth and S. Uyeda. On the Relative Importance of the Driving Forces of Plate Motion*. *Geophysical Journal International*, 43(1):163–200, Oct. 1975. ISSN 0956-540X. doi: 10.1111/j.1365-246X.1975.tb00631.x. URL https://doi.org/10.1111/j.1365-246X.1975.tb00631.x.

F. Fressin, G. Torres, D. Charbonneau, S. T. Bryson, J. Christiansen, C. D. Dressing, J. M. Jenkins, L. M. Walkowicz, and N. M. Batalha. The false positive rate of Kepler and the occurrence of planets. *The Astrophysical Journal*, 766(2):81, Mar. 2013. ISSN 0004-637X, 1538-4357. doi: 10.1088/0004-637X/766/2/81. URL http://arxiv.org/abs/1301.0842. arXiv:1301.0842 [astro-ph].

S. Friedlander and D. Serre. *Handbook of Mathematical Fluid Dynamics*. Gulf Professional Publishing, Mar. 2003. ISBN 9780080533544. Google-Books-ID: _LU53Q3A27MC.

B. J. Fulton, E. A. Petigura, A. W. Howard, H. Isaacson, G. W. Marcy, P. A. Cargile, L. Hebb, L. M. Weiss, J. A. Johnson, T. D. Morton, E. Sinukoff, I. J. M. Crossfield, and L. A. Hirsch. The California-Kepler Survey. III. A Gap in the Radius Distribution of Small Planets. *The Astronomical Journal*, 154(3):109, Sept. 2017. doi: 10.3847/1538-3881/aa80eb.

E. Gaidos, N. Haghighipour, E. Agol, D. Latham, S. Raymond, and J. Rayner. New worlds on the horizon: Earth-sized planets close to other stars. *Science*, 318(5848): 210–213, 2007. doi: 10.1126/science.1144358. URL https://www.science.org/doi/abs/10.1126/science.1144358.

F. Gaillard, F. Bernadou, M. Roskosz, M. A. Bouhifd, Y. Marrocchi, G. Iacono-Marziano, M. Moreira, B. Scaillet, and G. Rogerie. Redox controls during magma ocean degassing. *Earth and Planetary Science Letters*, 577:117255, Jan. 2021a. ISSN 0012-821X. doi: 10.1016/j.epsl.2021.117255. URL https://www.sciencedirect.com/science/article/pii/S0012821X21005112.

F. Gaillard, M. A. Bouhifd, E. Füri, V. Malavergne, Y. Marrocchi, L. Noack, G. Ortenzi, M. Roskosz, and S. Vulpius. The Diverse Planetary Ingassing/Outgassing

Paths Produced over Billions of Years of Magmatic Activity. *Space Science Reviews*, 217(1):22, Feb. 2021b. ISSN 1572-9672. doi: 10.1007/s11214-021-00802-1. URL https://doi.org/10.1007/s11214-021-00802-1.

.-. Galilei, Galileo. *Sidereus nuncius : Venice, 1610.* Octavo edition. Palo Alto, CA : Octavo, [1998] ©1998, 1610. URL https://search.library.wisc.edu/catalog/999877167302121.

S. E. Gelman, L. T. Elkins-Tanton, and S. Seager. Effects of stellar flux on tidally locked terrestrial planets: Degree-1 mantle convection and local magma ponds. *The Astrophysical Journal*, 735(2):72, June 2011. ISSN 0004-637X. doi: 10.1088/0004-637X/735/2/72. URL https://doi.org/10.1088%2F0004-637x%2F735%2F2%2F72.

C. Gillmann, M. J. Way, G. Avice, D. Breuer, G. J. Golabek, D. Honing, J. Krissansen-Totton, H. Lammer, A.-C. Plesa, M. Persson, J. G. O'Rourke, A. Salvador, M. Scherf, and M. Y. Zolotov. The long-term evolution of the atmosphere of Venus: processes and feedback mechanisms. *arXiv:2204.08540 [astro-ph, physics:physics]*, Apr. 2022. URL http://arxiv.org/abs/2204.08540. arXiv: 2204.08540.

B. Gladman, D. D. Quinn, P. Nicholson, and R. Rand. Synchronous Locking of Tidally Evolving Satellites. *Icarus*, 122(1):166–192, July 1996. ISSN 0019-1035. doi: 10.1006/icar.1996.0117. URL https://www.sciencedirect.com/science/article/pii/S0019103596901177.

G. J. Golabek, T. Keller, T. V. Gerya, G. Zhu, P. J. Tackley, and J. A. D. Connolly. Origin of the martian dichotomy and Tharsis from a giant impact causing massive magmatism. *Icarus*, 215(1):346–357, Sept. 2011. ISSN 0019-1035. doi: 10.1016/j.icarus.2011.06.012. URL https://www.sciencedirect.com/science/article/pii/S0019103511002211.

G. J. Golabek, A. Emsenhuber, M. Jutzi, E. I. Asphaug, and T. V. Gerya. Coupling SPH and thermochemical models of planets: Methodology and example of a Mars-sized body. *Icarus*, 301:235–246, Feb. 2018. ISSN 0019-1035. doi: 10.1016/j.

icarus.2017.10.003. URL https://www.sciencedirect.com/science/article/pii/S0019103517302385.

M. P. Golombek and R. J. Phillips. Mars tectonics. Cambridge Planetary Science, pages 183–232. Cambridge University Press, Cambridge, 2009. ISBN 9780521765732. doi: 10.1017/CBO9780511691645.006. URL https://www.cambridge.org/core/books/planetary-tectonics/mars-tectonics/FA7571F0ED8FE114F4AED3C3722507F2.

D. Gubbins, D. Alfè, G. Masters, G. D. Price, and M. J. Gillan. Can the earth's dynamo run on heat alone? *Geophys J Int*, 155(2):609–622, Nov. 2003. ISSN 0956-540X. doi: 10.1046/j.1365-246X.2003.02064.x. URL https://doi.org/10.1046/j.1365-246X.2003.02064.x.

C. M. Guimond, L. Noack, G. Ortenzi, and F. Sohl. Low volcanic outgassing rates for a stagnant lid Archean Earth with graphite-saturated magmas. *Physics of the Earth and Planetary Interiors*, 320:106788, Nov. 2021. ISSN 00319201. doi: 10.1016/j.pepi.2021.106788. URL http://arxiv.org/abs/2108.13438. arXiv: 2108.13438.

Gunell, Herbert, Maggiolo, Romain, Nilsson, Hans, Stenberg Wieser, Gabriella, Slapak, Rikard, Lindkvist, Jesper, Hamrin, Maria, and De Keyser, Johan. Why an intrinsic magnetic field does not protect a planet against atmospheric escape. *A&A*, 614:L3, 2018. doi: 10.1051/0004-6361/201832934. URL https://doi.org/10.1051/0004-6361/201832934.

A. J. P. Gülcher, T. V. Gerya, L. G. J. Montési, and J. Munch. Corona structures driven by plume–lithosphere interactions and evidence for ongoing plume activity on Venus. *Nature Geoscience*, 13(8):547–554, Aug. 2020. ISSN 1752-0908. doi: 10.1038/s41561-020-0606-1. URL https://www.nature.com/articles/s41561-020-0606-1.

M. Hammond and R. Pierrehumbert. Linking the Climate and Thermal Phase Curve of 55 Cancri e. *The Astrophysical Journal*, 2017. ISSN 15384357. doi: 10.3847/1538-4357/aa9328. URL http://arxiv.org/abs/1710.03556{%}0Ahttp://dx.doi.org/10.3847/1538-4357/aa9328.

L. N. Hansen, K. M. Kumamoto, C. A. Thom, D. Wallis, W. B. Durham, D. L. Goldsby, T. Breithaupt, C. D. Meyers, and D. L. Kohlstedt. Low-Temperature Plasticity in Olivine: Grain Size, Strain Hardening, and the Strength of the Lithosphere. *Journal of Geophysical Research: Solid Earth*, 124(6):5427–5449, 2019. ISSN 2169-9356. doi: https://doi.org/10.1029/2018JB016736. URL https://agupubs.onlinelibrary.wiley.com/doi/abs/10.1029/2018JB016736.

J. Head, L. Wilson, M. Ivanov, and R. Wordsworth. Contributions of Volatiles to the Venus Atmosphere from the Observed Extrusive Volcanic Record: Implications for the History of the Venus Atmosphere. pages EGU21–13030, Apr. 2021. doi: 10.5194/egusphere-egu21-13030. URL https://ui.adsabs.harvard.edu/abs/2021EGUGA..2313030H. ADS Bibcode: 2021EGUGA..2313030H.

T. L. Heath and o. S. Aristarchus. *Aristarchus of Samos, the ancient Copernicus ; a history of Greek astronomy to Aristarchus, together with Aristarchus's Treatise on the sizes and distances of the sun and moon : a new Greek text with translation and notes*. Oxford : Clarendon Press, 1913. URL http://archive.org/details/aristarchusofsam00heatuoft.

K. Heng and A. P. Showman. Atmospheric Dynamics of Hot Exoplanets. *Annual Review of Earth and Planetary Sciences*, 43(1):509–540, May 2015. ISSN 0084-6597, 1545-4495. doi: 10.1146/annurev-earth-060614-105146. URL http://arxiv.org/abs/1407.4150. arXiv:1407.4150 [astro-ph].

K. Heng, K. Menou, and P. J. Phillipps. Atmospheric circulation of tidally locked exoplanets: a suite of benchmark tests for dynamical solvers. *Monthly Notices of the Royal Astronomical Society*, 413(4):2380–2402, June 2011. ISSN 0035-8711. doi: 10.1111/j.1365-2966.2011.18315.x. URL https://doi.org/10.1111/j.1365-2966.2011.18315.x.

J. W. Hernlund and P. J. Tackley. Modeling mantle convection in the spherical annulus. *Physics of the Earth and Planetary Interiors*, 171(1-4):48–54, 2008. ISSN 00319201. doi: 10.1016/j.pepi.2008.07.037.

C. Herzberg, P. Raterron, and J. Zhang. New experimental observations on the

anhydrous solidus for peridotite KLB1. *Geochemistry Geophysics Geosystems - GEOCHEM GEOPHYS GEOSYST*, 1, Nov. 2000. doi: 10.1029/2000GC000089.

M. M. Hirschmann. Magma ocean influence on early atmosphere mass and composition. *Earth and Planetary Science Letters*, 341-344:48–57, Aug. 2012. ISSN 0012-821X. doi: 10.1016/j.epsl.2012.06.015. URL https://www.sciencedirect.com/science/article/pii/S0012821X12002993.

A. W. Howard, G. W. Marcy, S. T. Bryson, J. M. Jenkins, J. F. Rowe, N. M. Batalha, W. J. Borucki, D. G. Koch, E. W. Dunham, T. N. Gautier, J. V. Cleve, W. D. Cochran, D. W. Latham, J. J. Lissauer, G. Torres, T. M. Brown, R. L. Gilliland, L. A. Buchhave, D. A. Caldwell, J. Christensen-Dalsgaard, D. Ciardi, F. Fressin, M. R. Haas, S. B. Howell, H. Kjeldsen, S. Seager, L. Rogers, D. D. Sasselov, J. H. Steffen, G. S. Basri, D. Charbonneau, J. Christiansen, B. Clarke, A. Dupree, D. C. Fabrycky, D. A. Fischer, E. B. Ford, J. J. Fortney, J. Tarter, F. R. Girouard, M. J. Holman, J. A. Johnson, T. C. Klaus, P. Machalek, A. V. Moorhead, R. C. Morehead, D. Ragozzine, P. Tenenbaum, J. D. Twicken, S. N. Quinn, H. Isaacson, A. Shporer, P. W. Lucas, L. M. Walkowicz, W. F. Welsh, A. Boss, E. Devore, A. Gould, J. C. Smith, R. L. Morris, A. Prsa, T. D. Morton, M. Still, S. E. Thompson, F. Mullally, M. Endl, and P. J. MacQueen. Planet occurrence within 0.25 au of solar-type stars from kepler. *The Astrophysical Journal Supplement Series*, 201(2):15, June 2012. ISSN 0067-0049. doi: 10.1088/0067-0049/201/2/15. URL https://doi.org/10.1088/0067-0049/201/2/15.

R. Hu, B. L. Ehlmann, and S. Seager. Theoretical Spectra of Terrestrial Exoplanet Surfaces. *The Astrophysical Journal*, 752(1):7, June 2012. ISSN 0004-637X, 1538-4357. doi: 10.1088/0004-637X/752/1/7. URL http://arxiv.org/abs/1204.1544. arXiv: 1204.1544.

R. Hu, A. Brandeker, M. Damiano, B.-O. Demory, D. Dragomir, Y. Ito, H. A. Knutson, Y. Miguel, and M. Zhang. Jwst proposal 1952 - determining the atmospheric composition of the super-earth 55 cancri e, 2021. URL https://www.stsci.edu/jwst/science-execution/program-information.html?id=1952.

A. Ismail-Zadeh and P. Tackley. *Computational Methods for Geo-*

dynamics. Cambridge University Press, Cambridge, 2010. ISBN 9780521867672. doi: 10.1017/CBO9780511780820. URL https://www.cambridge.org/core/books/computational-methods-for-geodynamics/D5F735F7A1549CA11A14C3AF9D6428DA.

G. T. Jarvis and D. P. McKenzie. Convection in a compressible fluid with infinite Prandtl number. *Journal of Fluid Mechanics*, 96(3):515–583, 1980.

A. M. Jellinek and M. G. Jackson. Connections between the bulk composition, geodynamics and habitability of Earth. *Nature Geoscience*, 8(8):587–593, Aug. 2015. ISSN 1752-0908. doi: 10.1038/ngeo2488. URL https://www.nature.com/articles/ngeo2488.

A. Jindal, E. J. W. de Mooij, R. Jayawardhana, E. K. Deibert, M. Brogi, Z. Rustamkulov, J. J. Fortney, C. E. Hood, and C. V. Morley. Arid or Cloudy: Characterizing the Atmosphere of the super-Earth 55 Cancri e using High-Resolution Spectroscopy. *The Astronomical Journal*, 160(3):101, Aug. 2020. ISSN 1538-3881. doi: 10.3847/1538-3881/aba1eb. URL http://arxiv.org/abs/2007.03115. arXiv: 2007.03115.

M. M. Joshi, R. M. Haberle, and R. T. Reynolds. Simulations of the Atmospheres of Synchronously Rotating Terrestrial Planets Orbiting M Dwarfs: Conditions for Atmospheric Collapse and the Implications for Habitability. *Icarus*, 129(2): 450–465, Oct. 1997. ISSN 0019-1035. doi: 10.1006/icar.1997.5793. URL https://www.sciencedirect.com/science/article/pii/S0019103597957936.

R. V. S. Kanda and D. J. Stevenson. Suction mechanism for iron entrainment into the lower mantle. *Geophysical Research Letters*, 33(2), 2006. ISSN 1944-8007. doi: 10.1029/2005GL025009. URL https://onlinelibrary.wiley.com/doi/abs/10.1029/2005GL025009.

S. R. Kane, R. M. Roettenbacher, C. T. Unterborn, B. J. Foley, and M. L. Hill. A volatile-poor formation of lhs 3844b based on its lack of significant atmosphere, July 2020. URL https://ui.adsabs.harvard.edu/abs/2020arXiv200714493K.

S.-i. Karato and P. Wu. Rheology of the Upper Mantle: A Synthesis. *Science*, 260

(5109):771–778, 1993. ISSN 0036-8075. URL https://www.jstor.org/stable/2881160.

J. F. Kasting. Runaway and moist greenhouse atmospheres and the evolution of Earth and Venus. *Icarus*, 74(3):472–494, June 1988. ISSN 0019-1035. doi: 10.1016/0019-1035(88)90116-9. URL https://www.sciencedirect.com/science/article/pii/0019103588901169.

J. F. Kasting, D. P. Whitmire, and R. T. Reynolds. Habitable Zones around Main Sequence Stars. *Icarus*, 101(1):108–128, Jan. 1993. ISSN 0019-1035. doi: 10.1006/icar.1993.1010. URL https://www.sciencedirect.com/science/article/pii/S0019103583710109.

T. Keller and P. J. Tackley. Towards self-consistent modeling of the martian dichotomy: The influence of one-ridge convection on crustal thickness distribution. *Icarus*, 202(2):429–443, Aug. 2009. ISSN 0019-1035. doi: 10.1016/j.icarus.2009.03.029. URL https://www.sciencedirect.com/science/article/pii/S0019103509001377.

J. Kepler. *Astronomia nova.* (Pragae, 1609. OCLC: 82733804.

D. M. Kipping and G. Tinetti. Nightside Pollution of Exoplanet Transit Depths. *Monthly Notices of the Royal Astronomical Society*, 407(4):2589–2598, Aug. 2010. ISSN 00358711. doi: 10.1111/j.1365-2966.2010.17094.x. URL http://arxiv.org/abs/0912.1133. arXiv: 0912.1133.

K. Kislyakova and L. Noack. Electromagnetic induction heating as a driver of volcanic activity on massive rocky planets. *Astronomy & Astrophysics*, 636:L10, Apr. 2020. ISSN 0004-6361, 1432-0746. doi: 10.1051/0004-6361/202037924. URL http://arxiv.org/abs/2004.14041. arXiv:2004.14041 [astro-ph].

K. G. Kislyakova, L. Noack, C. P. Johnstone, V. V. Zaitsev, L. Fossati, H. Lammer, M. L. Khodachenko, P. Odert, and M. Güdel. Magma oceans and enhanced volcanism on trappist-1 planets due to induction heating. *Nature Astronomy*, 1(12):878–885, 2017. ISSN 2397-3366. doi: 10.1038/s41550-017-0284-0. URL https://doi.org/10.1038/s41550-017-0284-0.

E. S. Kite and M. N. Barnett. Exoplanet secondary atmosphere loss and revival. *Proceedings of the National Academy of Sciences*, 117(31):18264–18271, Aug. 2020. ISSN 0027-8424, 1091-6490. doi: 10.1073/pnas.2006177117. URL https://www.pnas.org/content/117/31/18264.

E. S. Kite, B. Fegley, L. Schaefer, and E. Gaidos. Atmosphere-interior exchange on hot rocky exoplanets. *The Astrophysical Journal*, 828, 2016. ISSN 1538-4357. doi: 10.3847/0004-637X/828/2/80. URL http://arxiv.org/abs/1606.06740{%}0Ahttp://dx.doi.org/10.3847/0004-637X/828/2/80.

D. L. Kohlstedt, B. Evans, and S. J. Mackwell. Strength of the lithosphere: Constraints imposed by laboratory experiments. *Journal of Geophysical Research: Solid Earth*, 100(B9):17587–17602, 1995. ISSN 2156-2202. doi: 10.1029/95JB01460. URL https://agupubs.onlinelibrary.wiley.com/doi/abs/10.1029/95JB01460.

J. Korenaga. Pitfalls in modeling mantle convection with internal heat production. *Journal of Geophysical Research: Solid Earth*, 122(5):4064–4085, 2017. ISSN 2169-9356. doi: 10.1002/2016JB013850. URL https://agupubs.onlinelibrary.wiley.com/doi/abs/10.1002/2016JB013850.

L. Kreidberg. Exoplanet Atmosphere Measurements from Transmission Spectroscopy and other Planet-Star Combined Light Observations. *arXiv:1709.05941 [astro-ph]*, pages 2083–2105, 2018. doi: 10.1007/978-3-319-55333-7_100. URL http://arxiv.org/abs/1709.05941. arXiv: 1709.05941.

L. Kreidberg, D. D. B. Koll, C. Morley, R. Hu, L. Schaefer, D. Deming, K. B. Stevenson, J. Dittmann, A. Vanderburg, D. Berardo, X. Guo, K. Stassun, I. Crossfield, D. Charbonneau, D. W. Latham, A. Loeb, G. Ricker, S. Seager, and R. Vanderspek. Absence of a thick atmosphere on the terrestrial exoplanet lhs 3844b. *Nature*, 573(7772):87–90, Sept. 2019. ISSN 1476-4687. URL https://doi.org/10.1038/s41586-019-1497-4.

L. Kreidberg, M. Malik, R. Hu, E. S. Kite, C. Morley, L. Schaefer, D. Koll, and E. Whittaker. Jwst proposal 1846: A search for signatures of volcanism and geodynamics on the hot rocky exoplanet lhs 3844b. JWST Pro-

posal, Cycle 1, 2021. URL https://www.stsci.edu/jwst/science-execution/program-information.html?id=1846.

S. Labrosse. Hotspots, mantle plumes and core heat loss. *Earth and Planetary Science Letters*, 199(1-2):147–156, 2002. ISSN 0012821X. doi: 10.1016/S0012-821X(02)00537-X.

S. Labrosse. Thermal and compositional stratification of the inner core. *Comptes Rendus Geoscience*, 346(5):119–129, May 2014. ISSN 1631-0713. doi: 10.1016/j.crte.2014.04.005. URL https://www.sciencedirect.com/science/article/pii/S1631071314000546.

S. Labrosse, J. W. Hernlund, and N. Coltice. A crystallizing dense magma ocean at the base of the Earth's mantle. *Nature*, 450(7171):866–869, Dec. 2007. ISSN 1476-4687. doi: 10.1038/nature06355. URL https://www.nature.com/articles/nature06355.

A. H. Lachenbruch. Dynamics of a passive spreading center. *Journal of Geophysical Research (1896-1977)*, 81(11):1883–1902, 1976. ISSN 2156-2202. doi: 10.1029/JB081i011p01883. URL https://onlinelibrary.wiley.com/doi/abs/10.1029/JB081i011p01883.

M. G. Langseth, S. J. Keihm, and K. Peters. Revised lunar heat-flow values. *Lunar and Planetary Science Conference Proceedings*, 3:3143–3171, Apr. 1976. URL https://ui.adsabs.harvard.edu/abs/1976LPSC....7.3143L. ADS Bibcode: 1976LPSC....7.3143L.

A. Léger, O. Grasset, B. Fegley, F. Codron, A. F. Albarede, P. Barge, R. Barnes, P. Cance, S. Carpy, F. Catalano, C. Cavarroc, O. Demangeon, S. Ferraz-Mello, P. Gabor, J. M. Grießmeier, J. Leibacher, G. Libourel, A. S. Maurin, S. N. Raymond, D. Rouan, B. Samuel, L. Schaefer, J. Schneider, P. A. Schuller, F. Selsis, and C. Sotin. The extreme physical properties of the CoRoT-7b super-Earth. *Icarus*, 213(1):1–11, May 2011. doi: 10.1016/j.icarus.2011.02.004. URL https://www.sciencedirect.com/science/article/pii/S0019103511000534.

A. Lenardic. The diversity of tectonic modes and thoughts about transitions between them. *Philosophical transactions. Series A, Mathematical, physical, and engineer-*

ing sciences, 376(2132):20170416, Nov. 2018. ISSN 1364-503X. doi: 10.1098/rsta.2017.0416. URL https://www.ncbi.nlm.nih.gov/pmc/articles/PMC6189555/.

A. Lenardic, A. M. Jellinek, and L.-N. Moresi. A climate induced transition in the tectonic style of a terrestrial planet. *Earth and Planetary Science Letters*, 271(1): 34–42, 2008. ISSN 0012-821X. URL http://www.sciencedirect.com/science/article/pii/S0012821X08001878.

T. Lichtenberg. Redox Hysteresis of Super-Earth Exoplanets from Magma Ocean Circulation. *The Astrophysical Journal Letters*, 914(1):L4, June 2021. ISSN 2041-8205. doi: 10.3847/2041-8213/ac0146. URL https://doi.org/10.3847/2041-8213/ac0146.

P. Liggins, S. Jordan, P. B. Rimmer, and O. Shorttle. Growth and evolution of secondary volcanic atmospheres: I. Identifying the geological character of hot rocky planets. *Journal of Geophysical Research: Planets*, July 2022. ISSN 2169-9097, 2169-9100. doi: 10.1029/2021JE007123. URL http://arxiv.org/abs/2111.05161. arXiv:2111.05161 [astro-ph, physics:physics].

D. L. Lourenço, A. Rozel, and P. J. Tackley. Melting-induced crustal production helps plate tectonics on earth-like planets. *Earth and Planetary Science Letters*, 439:18–28, Apr. 2016. ISSN 0012-821X. URL http://www.sciencedirect.com/science/article/pii/S0012821X16000467.

D. L. Lourenço, A. B. Rozel, M. D. Ballmer, and P. J. Tackley. Plutonic-Squishy Lid: A New Global Tectonic Regime Generated by Intrusive Magmatism on Earth-Like Planets. *Geochemistry, Geophysics, Geosystems*, 21(4): e2019GC008756, 2020. ISSN 1525-2027. doi: 10.1029/2019GC008756. URL https://onlinelibrary.wiley.com/doi/abs/10.1029/2019GC008756.

N. Madhusudhan. Exoplanetary atmospheres: Key insights, challenges, and prospects. *Annu. Rev. Astron. Astrophys.*, 57(1):617–663, Aug. 2019. ISSN 0066-4146. doi: 10.1146/annurev-astro-081817-051846. URL https://doi.org/10.1146/annurev-astro-081817-051846.

L. Malavolta, A. W. Mayo, T. Louden, V. M. Rajpaul, A. S. Bonomo, L. A. Buchhave, L. Kreidberg, M. H. Kristiansen, M. Lopez-Morales, A. Mortier, A. Van-

derburg, A. Coffinet, D. Ehrenreich, C. Lovis, F. Bouchy, D. Charbonneau, D. R. Ciardi, A. C. Cameron, R. Cosentino, I. J. M. Crossfield, M. Damasso, C. D. Dressing, X. Dumusque, M. E. Everett, P. Figueira, A. F. M. Fiorenzano, E. J. Gonzales, R. D. Haywood, A. Harutyunyan, L. Hirsch, S. B. Howell, J. A. Johnson, D. W. Latham, E. Lopez, M. Mayor, G. Micela, E. Molinari, V. Nascimbeni, F. Pepe, D. F. Phillips, G. Piotto, K. Rice, D. Sasselov, D. Ségransan, A. Sozzetti, S. Udry, and C. Watson. An ultra-short period rocky super-Earth with a secondary eclipse and a Neptune-like companion around K2-141. *The Astronomical Journal*, 155(3):107, Feb. 2018. ISSN 1538-3881. doi: 10.3847/1538-3881/aaa5b5. URL http://arxiv.org/abs/1801.03502. arXiv: 1801.03502.

M. M. Marinova, O. Aharonson, and E. Asphaug. Mega-impact formation of the Mars hemispheric dichotomy. *Nature*, 453(7199):1216–1219, June 2008. ISSN 1476-4687. doi: 10.1038/nature07070.

B. Marty. The origins and concentrations of water, carbon, nitrogen and noble gases on Earth. *Earth and Planetary Science Letters*, 313-314:56–66, Jan. 2012. ISSN 0012-821X. doi: 10.1016/j.epsl.2011.10.040. URL https://www.sciencedirect.com/science/article/pii/S0012821X11006388.

M. Mayor and D. Queloz. A Jupiter-mass companion to a solar-type star. *Nature*, 378(6555):355–359, Nov. 1995. ISSN 1476-4687. doi: 10.1038/378355a0. URL https://www.nature.com/articles/378355a0.

B. E. McArthur, M. Endl, W. D. Cochran, G. F. Benedict, D. A. Fischer, G. W. Marcy, R. P. Butler, D. Naef, M. Mayor, D. Queloz, S. Udry, and T. E. Harrison. Detection of a neptune-mass planet in the ρ^1 cancri system using the hobby-eberly telescope. *Astrophys. J. Lett.*, 614:L81–L84, Oct. 2004. doi: 10.1086/425561.

D. P. McKenzie. Speculations on the Consequences and Causes of Plate Motions*. *Geophysical Journal International*, 18(1):1–32, 09 1969. ISSN 0956-540X. doi: 10.1111/j.1365-246X.1969.tb00259.x. URL https://doi.org/10.1111/j.1365-246X.1969.tb00259.x.

A. K. McNamara and S. Zhong. Degree-one mantle convection: Dependence on internal heating and temperature-dependent rheology. *Geophysical Research*

Letters, 32(1), 2005. ISSN 1944-8007. doi: 10.1029/2004GL021082. URL https://onlinelibrary.wiley.com/doi/abs/10.1029/2004GL021082.

T. G. Meier, D. J. Bower, T. Lichtenberg, P. J. Tackley, and B.-O. Demory. Hemispheric Tectonics on LHS 3844b. *The Astrophysical Journal*, 908(2):L48, Feb. 2021. ISSN 2041-8205. doi: 10.3847/2041-8213/abe400. URL https://doi.org/10.3847/2041-8213/abe400.

L. Moresi and V. Solomatov. Mantle convection with a brittle lithosphere: thoughts on the global tectonic styles of the earth and venus. *Geophys J Int*, 133(3):669–682, June 1998. ISSN 0956-540X. URL https://doi.org/10.1046/j.1365-246X.1998.00521.x.

W. J. Morgan. Rises, trenches, great faults, and crustal blocks. *Journal of Geophysical Research (1896-1977)*, 73(6):1959–1982, 1968. ISSN 2156-2202. doi: 10.1029/JB073i006p01959. URL https://onlinelibrary.wiley.com/doi/abs/10.1029/JB073i006p01959.

W. J. Morgan. Convection Plumes in the Lower Mantle. *Nature*, 230(5288):42–43, Mar. 1971. ISSN 1476-4687. doi: 10.1038/230042a0. URL https://www.nature.com/articles/230042a0.

C. V. Morley, L. Kreidberg, Z. Rustamkulov, T. Robinson, and J. J. Fortney. Observing the Atmospheres of Known Temperate Earth-sized Planets with JWST. *The Astrophysical Journal*, 850(2):121, Nov. 2017. ISSN 1538-4357. doi: 10.3847/1538-4357/aa927b. URL http://arxiv.org/abs/1708.04239. arXiv: 1708.04239.

B. M. Morris, L. Delrez, A. Brandeker, A. C. Cameron, A. E. Simon, D. Futyan, G. Olofsson, S. Hoyer, A. Fortier, B.-O. Demory, M. Lendl, T. G. Wilson, M. Oshagh, K. Heng, D. Ehrenreich, S. Sulis, Y. Alibert, R. Alonso, G. A. Escudé, D. Barrado, S. C. C. Barros, W. Baumjohann, M. Beck, T. Beck, A. Bekkelien, W. Benz, M. Bergomi, N. Billot, X. Bonfils, V. Bourrier, C. Broeg, T. Bárczy, J. Cabrera, S. Charnoz, M. B. Davies, D. D. M. Ferreras, M. Deleuil, A. Deline, O. D. S. Demangeon, A. Erikson, H. G. Floren, L. Fossati, M. Fridlund, D. Gandolfi, A. G. Muñoz, M. Gillon, M. Guedel, P. Guterman, K. Isaak,

L. Kiss, J. Laskar, A. L. d. Etangs, M. Lieder, C. Lovis, D. Magrin, P. F. L. Maxted, V. Nascimbeni, R. Ottensamer, I. Pagano, E. Pallé, G. Peter, G. Piotto, A. P. Rubio, D. Pollacco, F. J. Pozuelos, D. Queloz, R. Ragazzoni, N. Rando, H. Rauer, I. Ribas, N. C. Santos, G. Scandariato, A. M. S. Smith, S. G. Sousa, M. Steller, G. M. Szabó, D. Ségransan, N. Thomas, S. Udry, B. Ulmer, V. Van Grootel, and N. A. Walton. CHEOPS Precision Phase Curve of the Super-Earth 55 Cnc e. *arXiv:2106.07443 [astro-ph]*, June 2021. URL http://arxiv.org/abs/2106.07443. arXiv: 2106.07443.

G. D. Mulders, I. Pascucci, D. Apai, and F. J. Ciesla. The Exoplanet Population Observation Simulator. I. The Inner Edges of Planetary Systems. *The Astronomical Journal*, 156(1):24, June 2018. ISSN 1538-3881. doi: 10.3847/1538-3881/aac5ea. URL https://doi.org/10.3847/1538-3881/aac5ea.

M. Murakami, K. Hirose, K. Kawamura, N. Sata, and Y. Ohishi. Post-perovskite phase transition in mgsio3. *Science*, 304(5672):855, May 2004. URL http://science.sciencemag.org/content/304/5672/855.abstract.

A. Méndez and E. G. Rivera-Valentín. The Equilibrium Temperature of Planets in Elliptical Orbits. *The Astrophysical Journal*, 837(1):L1, Feb. 2017. ISSN 2041-8205. doi: 10.3847/2041-8213/aa5f13. URL https://doi.org/10.3847/2041-8213/aa5f13.

I. Newton. *Philosophia naturalis principia mathematica*. 1687. OCLC: 15629050.

T. G. Nguyen, N. B. Cowan, A. Banerjee, and J. E. Moores. Modelling the atmosphere of lava planet K2-141b: implications for low and high resolution spectroscopy. *Monthly Notices of the Royal Astronomical Society*, 499(4):4605–4612, Dec. 2020. ISSN 0035-8711, 1365-2966. doi: 10.1093/mnras/staa2487. URL http://arxiv.org/abs/2010.14101. arXiv: 2010.14101.

L. Noack, A. Rivoldini, and T. Van Hoolst. Volcanism and outgassing of stagnant-lid planets: Implications for the habitable zone. *Physics of the Earth and Planetary Interiors*, 269, May 2017. URL https://www.sciencedirect.com/science/article/pii/S0031920116301509.

L. Noack, K. G. Kislyakova, C. P. Johnstone, M. Güdel, and L. Fossati. Interior heating and outgassing of Proxima Centauri b: Identifying critical parameters. *Astronomy & Astrophysics*, 651:A103, July 2021. doi: 10.1051/0004-6361/202040176.

C. O'Neill and A. Lenardic. Geological consequences of super-sized Earths. *Geophysical Research Letters*, 34(19), 2007. ISSN 1944-8007. doi: https://doi.org/10.1029/2007GL030598. URL https://agupubs.onlinelibrary.wiley.com/doi/abs/10.1029/2007GL030598.

C. O'Neill, A. M. Jellinek, and A. Lenardic. Conditions for the onset of plate tectonics on terrestrial planets and moons. *Earth and Planetary Science Letters*, 261(1): 20–32, Sept. 2007. ISSN 0012-821X. doi: 10.1016/j.epsl.2007.05.038. URL https://www.sciencedirect.com/science/article/pii/S0012821X07003457.

J. G. O'Rourke. Venus: A Thick Basal Magma Ocean May Exist Today. *Geophysical Research Letters*, 47(4):e2019GL086126, 2020. ISSN 1944-8007. doi: 10.1029/2019GL086126. URL https://onlinelibrary.wiley.com/doi/abs/10.1029/2019GL086126.

A. Ortelius. *Abrahami Ortelii Antverpiani thesaurus geographicus: in quo omnium totius terrae regionum, montium ...* Plantin, Antverpia//Antwerpen/, 1596. OCLC: 214324616.

G. Ortenzi, L. Noack, F. Sohl, C. M. Guimond, J. L. Grenfell, C. Dorn, J. M. Schmidt, S. Vulpius, N. Katyal, D. Kitzmann, and H. Rauer. Mantle redox state drives outgassing chemistry and atmospheric composition of rocky planets. *Scientific Reports*, 10(1):10907, July 2020. ISSN 2045-2322. doi: 10.1038/s41598-020-67751-7. URL https://www.nature.com/articles/s41598-020-67751-7.

J. E. Owen and Y. Wu. The Evaporation Valley in the Kepler Planets. *The Astrophysical Journal*, 847(1):29, Sept. 2017. ISSN 0004-637X. doi: 10.3847/1538-4357/aa890a. URL https://doi.org/10.3847/1538-4357/aa890a.

V. Parmentier and I. Crossfield. Exoplanet phase curves: observations and theory. *arXiv:1711.07696 [astro-ph]*, pages 1419–1440, 2018. doi: 10.1007/

978-3-319-55333-7_116. URL http://arxiv.org/abs/1711.07696. arXiv: 1711.07696.

S. J. Peale. *Rotation Histories of the Natural Satellites*. Jan. 1977. URL https://ui.adsabs.harvard.edu/abs/1977plsa.conf...87P. ADS Bibcode: 1977plsa.conf...87P.

S. J. Peale, P. Cassen, and T. Reynolds R. Melting of io by tidal dissipation. *Science*, 203(4383):892–894, Mar. 1979. doi: 10.1126/science.203.4383.892. URL https://doi.org/10.1126/science.203.4383.892.

F. Pepe, C. Lovis, D. Ségransan, W. Benz, F. Bouchy, X. Dumusque, M. Mayor, D. Queloz, N. C. Santos, and S. Udry. The HARPS search for Earth-like planets in the habitable zone: I – Very low-mass planets around HD20794, HD85512 and HD192310. *Astronomy & Astrophysics*, 534:A58, Oct. 2011. ISSN 0004-6361, 1432-0746. doi: 10.1051/0004-6361/201117055. URL http://arxiv.org/abs/1108.3447. arXiv:1108.3447 [astro-ph].

M. Perryman. *The Exoplanet Handbook*. Cambridge University Press, Cambridge, 2 edition, 2018. ISBN 9781108419772. doi: 10.1017/9781108304160. URL https://www.cambridge.org/core/books/exoplanet-handbook/750759E015FDCF469D141F0046198519.

N. A. Phillips. The general circulation of the atmosphere: A numerical experiment. *Quarterly Journal of the Royal Meteorological Society*, 82(352):123–164, 1956. ISSN 1477-870X. doi: 10.1002/qj.49708235202. URL https://onlinelibrary.wiley.com/doi/abs/10.1002/qj.49708235202.

R. T. Pierrehumbert. A palette of climates for gliese 581g. *The Astrophysical Journal*, 726(1):L8, Dec. 2010. ISSN 2041-8205. doi: 10.1088/2041-8205/726/1/L8. URL https://doi.org/10.1088/2041-8205/726/1/l8.

R. Ramstad and S. Barabash. Do intrinsic magnetic fields protect planetary atmospheres from stellar winds? *Space Science Reviews*, 217(2):36, 2021. ISSN 1572-9672. doi: 10.1007/s11214-021-00791-1. URL https://doi.org/10.1007/s11214-021-00791-1.

S. I. Rasool and C. De Bergh. The Runaway Greenhouse and the Accumulation of CO_2 in the Venus Atmosphere. *Nature*, 226(5250):1037–1039, June 1970. ISSN 1476-4687. doi: 10.1038/2261037a0. URL https://www.nature.com/articles/2261037a0.

S. N. Raymond, R. Barnes, and A. M. Mandell. Observable consequences of planet formation models in systems with close-in terrestrial planets. *Monthly Notices of the Royal Astronomical Society*, 384(2):663–674, Feb. 2008. ISSN 0035-8711. doi: 10.1111/j.1365-2966.2007.12712.x. URL https://doi.org/10.1111/j.1365-2966.2007.12712.x.

H. H. Read and J. Watson. *Introduction to geology,*. Macmillan; St. Martin's Press, London; New York, 1962. ISBN 9780333176696 9780333116937 9780333176672 9780333176689 9780333112854 9780470711651 9780470711668. OCLC: 1452295.

J. H. Roberts and S. Zhong. Degree-1 convection in the Martian mantle and the origin of the hemispheric dichotomy. *Journal of Geophysical Research: Planets*, 111(E6), 2006. ISSN 2156-2202. doi: 10.1029/2005JE002668. URL https://onlinelibrary.wiley.com/doi/abs/10.1029/2005JE002668.

T. Rolf, B. Steinberger, U. Sruthi, and S. C. Werner. Inferences on the mantle viscosity structure and the post-overturn evolutionary state of Venus. *Icarus*, 313:107–123, 2018. ISSN 10902643. doi: 10.1016/j.icarus.2018.05.014.

A. Rozel, G. J. Golabek, R. Näf, and P. J. Tackley. Formation of ridges in a stable lithosphere in mantle convection models with a viscoplastic rheology. *Geophysical Research Letters*, 42(12):4770–4777, June 2015. ISSN 0094-8276. doi: 10.1002/2015GL063483. URL https://www.ncbi.nlm.nih.gov/pmc/articles/PMC5012122/.

L. G. Sammon and W. F. McDonough. Quantifying Earth's radiogenic heat budget. *Earth and Planetary Science Letters*, 593:117684, Sept. 2022. ISSN 0012-821X. doi: 10.1016/j.epsl.2022.117684. URL https://www.sciencedirect.com/science/article/pii/S0012821X2200320X.

L. Schaefer and L. T. Elkins-Tanton. Magma oceans as a critical stage in the tectonic development of rocky planets. *Philosophical Transactions of the Royal Society*

A: Mathematical, Physical and Engineering Sciences, 376(2132):20180109, Nov. 2018. doi: 10.1098/rsta.2018.0109. URL https://royalsocietypublishing.org/doi/10.1098/rsta.2018.0109.

L. Schaefer and B. Fegley. Chemistry of silicate atmospheres of evaporating super-earths. *The Astrophysical Journal*, 703(2):L113–L117, Sept. 2009. ISSN 0004-637X. doi: 10.1088/0004-637X/703/2/L113. URL https://doi.org/10.1088/0004-637x/703/2/l113.

G. Schubert, D. L. Turcotte, and E. R. Oxburgh. Stability of planetary interiors. *Geophysical Journal of the Royal Astronomical Society*, 18(5):441–460, Nov. 1969. ISSN 0016-8009. doi: 10.1111/j.1365-246x.1969.tb03370.x. URL https://doi.org/10.1111/j.1365-246X.1969.tb03370.x.

G. Schubert, D. L. Turcotte, and P. Olson. *Mantle Convection in the Earth and Planets*. Cambridge University Press, Cambridge, 2001. doi: 10.1017/CBO9780511612879. URL https://www.cambridge.org/core/books/mantle-convection-in-the-earth-and-planets/F87593774E3E50FCFC7C451F05254C2C.

S. Seager. Exoplanet Habitability. *Science*, May 2013. doi: 10.1126/science.1232226. URL https://www.science.org/doi/abs/10.1126/science.1232226.

A. P. Showman and T. Guillot. Atmospheric circulation and tides of "51 Pegasus b-like" planets. *Astronomy & Astrophysics*, 385(1):166–180, Apr. 2002. ISSN 0004-6361, 1432-0746. doi: 10.1051/0004-6361:20020101. URL https://www.aanda.org/articles/aa/abs/2002/13/aa1885/aa1885.html.

V. S. Solomatov. *Fluid Dynamics of a Terrestrial Magma Ocean*. Jan. 2000. URL https://ui.adsabs.harvard.edu/abs/2000orem.book..323S. ADS Bibcode: 2000orem.book..323S.

V. S. Solomatov. Magma oceans and primordial mantle differentiation. volume 9 of *Treatise on Geophysics*, pages 91–119. Dec. 2007.

P. A. Sossi, A. D. Burnham, J. Badro, A. Lanzirotti, M. Newville, and H. S. O'Neill. Redox state of Earth's magma ocean and its Venus-like early atmosphere. *Science*

Advances, 6(48):eabd1387, 2020. doi: 10.1126/sciadv.abd1387. URL https://www.science.org/doi/10.1126/sciadv.abd1387.

F. D. Stacey. Thermoelasticity of a mineral composite and a reconsideration of lower mantle properties. *Physics of the Earth and Planetary Interiors*, 106(3):219–236, Apr. 1998. ISSN 0031-9201. doi: 10.1016/S0031-9201(98)00084-3. URL https://www.sciencedirect.com/science/article/pii/S0031920198000843.

V. Stamenković, L. Noack, D. Breuer, and T. Spohn. The influence of pressure-dependent viscosity on the thermal evolution of super-earths. *The Astrophysical Journal*, 748(1):41, mar 2012. doi: 10.1088/0004-637x/748/1/41. URL https://doi.org/10.1088/0004-637x/748/1/41.

D. J. Stevenson. Origin of the Moon-The Collision Hypothesis. *Annual Review of Earth and Planetary Sciences*, 15:271, Jan. 1987. ISSN 0084-6597. doi: 10.1146/annurev.ea.15.050187.001415. URL https://ui.adsabs.harvard.edu/abs/1987AREPS..15..271S. ADS Bibcode: 1987AREPS..15..271S.

K. B. Stevenson, J.-M. Désert, M. R. Line, J. L. Bean, J. J. Fortney, A. P. Showman, T. Kataria, L. Kreidberg, P. R. McCullough, G. W. Henry, D. Charbonneau, A. Burrows, S. Seager, N. Madhusudhan, M. H. Williamson, and D. Homeier. Thermal structure of an exoplanet atmosphere from phase-resolved emission spectroscopy. *Science*, 346(6211):838–841, 2014. doi: 10.1126/science.1256758. URL https://www.science.org/doi/abs/10.1126/science.1256758.

L. Stixrude. Melting in super-earths. *Philosophical Transactions. Series A, Mathematical, Physical, and Engineering Sciences*, 372(2014):20130076, Apr. 2014. ISSN 1364-503X. doi: 10.1098/rsta.2013.0076. URL https://royalsocietypublishing.org/doi/10.1098/rsta.2013.0076.

L. Stixrude, N. de Koker, N. Sun, M. Mookherjee, and B. B. Karki. Thermodynamics of silicate liquids in the deep Earth. *Earth and Planetary Science Letters*, 278(3):226–232, Feb. 2009. ISSN 0012-821X. doi: 10.1016/j.epsl.2008.12.006. URL https://www.sciencedirect.com/science/article/pii/S0012821X08007565.

S. Sulis, D. Dragomir, M. Lendl, V. Bourrier, B. O. Demory, L. Fossati, P. E. Cubillos, D. B. Guenther, S. R. Kane, R. Kuschnig, J. M. Matthews, A. F. J. Moffat, J. F. Rowe, D. Sasselov, W. W. Weiss, and J. N. Winn. Multi-season optical modulation phased with the orbit of the super-Earth 55 Cancri e. *Astronomy & Astrophysics*, 631:A129, Nov. 2019. ISSN 0004-6361, 1432-0746. doi: 10.1051/0004-6361/201936066. URL https://www.aanda.org/articles/aa/abs/2019/11/aa36066-19/aa36066-19.html.

M. R. Swain, R. Estrela, G. M. Roudier, C. Sotin, P. B. Rimmer, A. Valio, R. West, K. Pearson, N. Huber-Feely, and R. T. Zellem. Detection of an Atmosphere on a Rocky Exoplanet. *The Astronomical Journal*, 161(5):213, Apr. 2021. ISSN 1538-3881. doi: 10.3847/1538-3881/abe879. URL https://doi.org/10.3847/1538-3881/abe879.

P. J. Tackley. Self-consistent generation of tectonic plates in time-dependent, three-dimensional mantle convection simulations. *Geochemistry, Geophysics, Geosystems*, 1(8), 2000. ISSN 1525-2027. doi: https://doi.org/10.1029/2000GC000036. URL https://agupubs.onlinelibrary.wiley.com/doi/abs/10.1029/2000GC000036.

P. J. Tackley. Modelling compressible mantle convection with large viscosity contrasts in a three-dimensional spherical shell using the yin-yang grid. *Physics of the Earth and Planetary Interiors*, 171(1-4):7–18, 2008. ISSN 00319201. doi: 10.1016/j.pepi.2008.08.005. URL https://www.sciencedirect.com/science/article/pii/S0031920108002276.

P. J. Tackley, D. J. Stevenson, G. A. Glatzmaier, and G. Schubert. Effects of an endothermic phase transition at 670 km depth in a spherical model of convection in the Earth's mantle. *Nature*, 361(6414):699–704, Feb. 1993. ISSN 1476-4687. doi: 10.1038/361699a0. URL https://www.nature.com/articles/361699a0.

P. J. Tackley, M. Ammann, J. P. Brodholt, D. P. Dobson, and D. Valencia. Mantle dynamics in super-Earths: Post-perovskite rheology and self-regulation of viscosity. *Icarus*, 225(1):50–61, 2013. ISSN 00191035. doi: 10.1016/j.icarus.2013.03.013. URL http://dx.doi.org/10.1016/j.icarus.2013.03.013.

E. Tan, M. Gurnis, and L. Han. Slabs in the lower mantle and their modulation of plume formation. *Geochemistry, Geophysics, Geosystems*, 3(11):1–24, 2002. ISSN 15252027. doi: 10.1029/2001GC000238. URL http://doi.wiley.com/10.1029/2001GC000238.

P. F. Thompson and P. J. Tackley. Generation of mega-plumes from the core-mantle boundary in a compressible mantle with temperature-dependent viscosity. *Geophysical Research Letters*, 25:1999–2002, 1998. doi: 10.1029/98GL01228.

G. Tobie, A. Mocquet, and C. Sotin. Tidal dissipation within large icy satellites: Applications to Europa and Titan. *Icarus*, 177(2):534–549, Oct. 2005. ISSN 0019-1035. doi: 10.1016/j.icarus.2005.04.006. URL https://www.sciencedirect.com/science/article/pii/S0019103505001582.

M. N. Toksőz and S. C. Solomon. Thermal History and Evolution of the Moon. *Moon*, 7:251–278, Sept. 1973. ISSN 0165-0807. doi: 10.1007/BF00564634. URL https://ui.adsabs.harvard.edu/abs/1973Moon....7..251T. ADS Bibcode: 1973Moon....7..251T.

B. Travis, P. Olson, and G. Schubert. The transition from two-dimensional to three-dimensional planforms in infinite-prandtl-number thermal convection. *Journal of Fluid Mechanics*, 216:71–91, 1990. doi: 10.1017/S0022112090000349.

T. Trifonov, J. A. Caballero, J. C. Morales, A. Seifahrt, I. Ribas, A. Reiners, J. L. Bean, R. Luque, H. Parviainen, E. Pallé, S. Stock, M. Zechmeister, P. J. Amado, G. Anglada-Escudé, M. Azzaro, T. Barclay, V. J. S. Béjar, P. Bluhm, N. Casasayas-Barris, C. Cifuentes, K. A. Collins, K. I. Collins, M. Cortés-Contreras, J. d. Leon, S. Dreizler, C. D. Dressing, E. Esparza-Borges, N. Espinoza, M. Fausnaugh, A. Fukui, A. P. Hatzes, C. Hellier, T. Henning, C. E. Henze, E. Herrero, S. V. Jeffers, J. M. Jenkins, E. L. N. Jensen, A. Kaminski, D. Kasper, D. Kossakowski, M. Kürster, M. Lafarga, D. W. Latham, A. W. Mann, K. Molaverdikhani, D. Montes, B. T. Montet, F. Murgas, N. Narita, M. Oshagh, V. M. Passegger, D. Pollacco, S. N. Quinn, A. Quirrenbach, G. R. Ricker, C. R. López, J. Sanz-Forcada, R. P. Schwarz, A. Schweitzer, S. Seager, A. Shporer, M. Stangret, J. Stürmer, T. G. Tan, P. Tenenbaum, J. D.

Twicken, R. Vanderspek, and J. N. Winn. A nearby transiting rocky exoplanet that is suitable for atmospheric investigation. *Science*, 371(6533):1038–1041, Mar. 2021. ISSN 0036-8075, 1095-9203. doi: 10.1126/science.abd7645. URL https://science.sciencemag.org/content/371/6533/1038.

D. L. Turcotte. An episodic hypothesis for venusian tectonics. *Journal of Geophysical Research*, 98:17061–17068, Sept. 1993. ISSN 0148-0227. doi: 10.1029/93JE01775. URL https://ui.adsabs.harvard.edu/abs/1993JGR....9817061T. ADS Bibcode: 1993JGR....9817061T.

K. Umemoto, R. M. Wentzcovitch, and P. B. Allen. Dissociation of $MgSiO_3$ in the cores of gas giants and terrestrial exoplanets. *Science*, 311(5763):983–986, Feb. 2006. ISSN 0036-8075. doi: 10.1126/science.1120865. URL http://www.scopus.com/inward/record.url?scp=33144463123&partnerID=8YFLogxK.

C. T. Unterborn, J. A. Johnson, and W. R. Panero. Thorium abundances in solar twins and analogs: Implications for the habitability of extrasolar planetary systems. *The Astrophysical Journal*, 806(1):139, June 2015. ISSN 0004-637X. doi: 10.1088/0004-637X/806/1/139. URL https://doi.org/10.1088/0004-637x/806/1/139.

H. C. Urey. The origin and development of the earth and other terrestrial planets. *Geochimica et Cosmochimica Acta*, 1(4):209–277, Jan. 1951. ISSN 0016-7037. doi: 10.1016/0016-7037(51)90001-4. URL https://www.sciencedirect.com/science/article/pii/0016703751900014.

E. A. M. Valdés, B. M. Morris, R. D. Wells, N. Schanche, and B.-O. Demory. Weak evidence for variable occultation depth of 55 Cnc e with TESS. *Astronomy & Astrophysics*, 663:A95, July 2022. ISSN 0004-6361, 1432-0746. doi: 10.1051/0004-6361/202243768. URL http://arxiv.org/abs/2205.08560. arXiv:2205.08560 [astro-ph].

D. Valencia, R. J. O'Connell, and D. Sasselov. Internal structure of massive terrestrial planets. *Icarus*, 181(2):545–554, Apr. 2006. ISSN 0019-1035. doi: 10.1016/j.icarus.2005.11.021. URL https://www.sciencedirect.com/science/article/pii/S0019103505004574.

D. Valencia, R. J. O'Connell, and D. D. Sasselov. Inevitability of Plate Tectonics on Super-Earths. *The Astrophysical Journal*, 670(1):L45, Oct. 2007a. ISSN 0004-637X. doi: 10.1086/524012. URL https://iopscience.iop.org/article/10.1086/524012/meta.

D. Valencia, D. D. Sasselov, and R. J. O'Connell. Radius and Structure Models of the First Super-Earth Planet. *The Astrophysical Journal*, 656(1):545–551, Feb. 2007b. ISSN 0004-637X. doi: 10.1086/509800. URL https://doi.org/10.1086/509800.

D. Valencia, M. Ikoma, T. Guillot, and N. Nettelmann. Composition and fate of short-period super-Earths - The case of CoRoT-7b. *Astronomy & Astrophysics*, 516:A20, June 2010. ISSN 0004-6361, 1432-0746. doi: 10.1051/0004-6361/200912839. URL https://www.aanda.org/articles/aa/abs/2010/08/aa12839-09/aa12839-09.html.

H. van Heck and P. Tackley. Plate tectonics on super-earths: Equally or more likely than on earth. *Earth and Planetary Science Letters*, 310(3):252 – 261, 2011. ISSN 0012-821X. doi: https://doi.org/10.1016/j.epsl.2011.07.029. URL http://www.sciencedirect.com/science/article/pii/S0012821X11004559.

J. Van Summeren, C. P. Conrad, and E. Gaidos. Mantle convection, plate tectonics, and volcanism on hot exo-earths. *Astrophysical Journal Letters*, 736(1):2–7, 2011. ISSN 20418205. doi: 10.1088/2041-8205/736/1/L15.

R. Vanderspek, C. X. Huang, A. Vanderburg, G. R. Ricker, D. W. Latham, S. Seager, J. N. Winn, J. M. Jenkins, J. Burt, J. Dittmann, E. Newton, S. N. Quinn, A. Shporer, D. Charbonneau, J. Irwin, K. Ment, J. G. Winters, K. A. Collins, P. Evans, T. Gan, R. Hart, E. L. N. Jensen, J. Kielkopf, S. Mao, W. Waalkes, F. Bouchy, M. Marmier, L. D. Nielsen, G. Ottoni, F. Pepe, D. Ségransan, S. Udry, T. Henry, L. A. Paredes, H.-S. James, R. H. Hinojosa, M. L. Silverstein, E. Palle, Z. Berta-Thompson, I. Crossfield, M. D. Davies, D. Dragomir, M. Fausnaugh, A. Glidden, J. Pepper, E. H. Morgan, M. Rose, J. D. Twicken, J. N. S. Villaseñor, L. Yu, G. Bakos, J. Bean, L. A. Buchhave, J. Christensen-Dalsgaard, J. L. Christiansen, D. R. Ciardi, M. Clampin, N. D. Lee, D. Deming, J. Doty, J. G. Jernigan, L. Kaltenegger, J. J. Lissauer, P. R. McCullough, N. Narita, M. Paegert, A. Pal,

S. Rinehart, D. Sasselov, B. Sato, A. Sozzetti, K. G. Stassun, and G. Torres. TESS discovery of an ultra-short-period planet around the nearby m dwarf LHS 3844. *The Astrophysical Journal*, 871(2):L24, jan 2019. doi: 10.3847/2041-8213/aafb7a. URL https://doi.org/10.3847%2F2041-8213%2Faafb7a.

J. C. G. Walker, P. B. Hays, and J. F. Kasting. A negative feedback mechanism for the long-term stabilization of Earth's surface temperature. *Journal of Geophysical Research: Oceans*, 86(C10):9776–9782, 1981. ISSN 2156-2202. doi: 10.1029/JC086iC10p09776. URL https://onlinelibrary.wiley.com/doi/abs/10.1029/JC086iC10p09776.

J. Wang, D. A. Fischer, E. P. Horch, and X. Huang. On the occurrence rate of hot jupiters in different stellar environments. *The Astrophysical Journal*, 799 (2):229, Jan. 2015. ISSN 0004-637X. doi: 10.1088/0004-637X/799/2/229. URL https://doi.org/10.1088/0004-637x/799/2/229.

T. R. Watters. A case for limited global contraction of Mercury. *Communications Earth & Environment*, 2(1):1–9, Jan. 2021. ISSN 2662-4435. doi: 10.1038/s43247-020-00076-5. URL https://www.nature.com/articles/s43247-020-00076-5.

T. R. Watters, K. Daud, M. E. Banks, M. M. Selvans, C. R. Chapman, and C. M. Ernst. Recent tectonic activity on Mercury revealed by small thrust fault scarps. *Nature Geoscience*, 9(10):743–747, Oct. 2016. ISSN 1752-0908. doi: 10.1038/ngeo2814. URL https://www.nature.com/articles/ngeo2814.

M. J. Way and A. D. Del Genio. Venusian Habitable Climate Scenarios: Modeling Venus Through Time and Applications to Slowly Rotating Venus-Like Exoplanets. *Journal of Geophysical Research: Planets*, 125(5):e2019JE006276, 2020. ISSN 2169-9100. doi: 10.1029/2019JE006276. URL https://onlinelibrary.wiley.com/doi/abs/10.1029/2019JE006276.

M. J. Way, A. D. Del Genio, N. Y. Kiang, L. E. Sohl, D. H. Grinspoon, I. Aleinov, M. Kelley, and T. Clune. Was Venus the first habitable world of our solar system? *Geophysical Research Letters*, 43(16):8376–8383, 2016. ISSN 1944-8007. doi: 10.

1002/2016GL069790. URL https://onlinelibrary.wiley.com/doi/abs/10.1002/2016GL069790.

A. Wegener. *Die Entstehung der Kontinente und Ozeane*. Druck und Verlag von Friedr. Vieweg & Sohn, Braunschweig, 1915. OCLC: 6827249.

G. W. Wetherill. *Accumulation of Mercury from planetesimals*. Jan. 1988. URL https://ui.adsabs.harvard.edu/abs/1988merc.book..670W. ADS Bibcode: 1988merc.book..670W.

J. N. Winn, R. Sanchis-Ojeda, and S. Rappaport. Kepler-78 and the Ultra-Short-Period planets. *New Astronomy Reviews*, 83:37–48, Nov. 2018. ISSN 1387-6473. doi: 10.1016/j.newar.2019.03.006. URL https://www.sciencedirect.com/science/article/pii/S1387647318300046.

J. T. Wright and B. S. Gaudi. Exoplanet Detection Methods. Technical report, Oct. 2012. URL http://arxiv.org/abs/1210.2471. arXiv:1210.2471 [astro-ph].

M. Yoshida and A. Kageyama. Low-degree mantle convection with strongly temperature- and depth-dependent viscosity in a three-dimensional spherical shell. *Journal of Geophysical Research: Solid Earth*, 111(B3), 2006. ISSN 2156-2202. doi: 10.1029/2005JB003905. URL https://onlinelibrary.wiley.com/doi/abs/10.1029/2005JB003905.

M. Yoshida and M. Santosh. Supercontinents, mantle dynamics and plate tectonics: A perspective based on conceptual vs. numerical models. *Earth-Science Reviews*, 105(1):1–24, Mar. 2011. ISSN 0012-8252. doi: 10.1016/j.earscirev.2010.12.002. URL https://www.sciencedirect.com/science/article/pii/S0012825210001753.

J.-P. Zahn. Tidal dissipation in binary systems. *EAS Publications Series*, 29:67–90, 2008. ISSN 1633-4760, 1638-1963. doi: 10.1051/eas:0829002. URL http://arxiv.org/abs/0807.4870. arXiv: 0807.4870.

K. J. Zahnle and D. C. Catling. The Cosmic Shoreline: The Evidence that Escape Determines which Planets Have Atmospheres, and what this May Mean for Proxima Centauri B. *The Astrophysical Journal*, 843(2):122, July 2017. ISSN

0004-637X. doi: 10.3847/1538-4357/aa7846. URL https://doi.org/10.3847/1538-4357/aa7846.

L. Zeng and D. Sasselov. The effect of temperature evolution on the interior structure of H_2O-rich planets. *The Astrophysical Journal*, 784(2):96, Mar. 2014. ISSN 0004-637X. doi: 10.1088/0004-637X/784/2/96. URL https://doi.org/10.1088/0004-637x/784/2/96.

A. Zerr, A. Diegeler, and R. Boehler. Solidus of Earth's deep mantle. *Science (New York, N.Y.)*, 281(5374):243–246, July 1998. ISSN 1095-9203. doi: 10.1126/science.281.5374.243. URL https://www.science.org/doi/abs/10.1126/science.281.5374.243.

S. Zhang and C. O'Neill. The early geodynamic evolution of Mars-type planets. *Icarus*, 265:187–208, Feb. 2016. ISSN 0019-1035. doi: 10.1016/j.icarus.2015.10.019. URL https://www.sciencedirect.com/science/article/pii/S0019103515004856.

S. Zhong and M. T. Zuber. Degree-1 mantle convection and the crustal dichotomy on Mars. *Earth and Planetary Science Letters*, 189(1):75–84, June 2001. ISSN 0012-821X. doi: 10.1016/S0012-821X(01)00345-4. URL https://www.sciencedirect.com/science/article/pii/S0012821X01003454.

S. Zhong, E. M. Parmentier, and M. T. Zuber. A dynamic origin for the global asymmetry of lunar mare basalts. *Earth and Planetary Science Letters*, 177(3):131–140, Apr. 2000. ISSN 0012-821X. doi: 10.1016/S0012-821X(00)00041-8. URL https://www.sciencedirect.com/science/article/pii/S0012821X00000418.

S. Zhong, N. Zhang, Z.-X. Li, and J. H. Roberts. Supercontinent cycles, true polar wander, and very long-wavelength mantle convection. *Earth and Planetary Science Letters*, 261(3):551–564, Sept. 2007. ISSN 0012-821X. doi: 10.1016/j.epsl.2007.07.049. URL https://www.sciencedirect.com/science/article/pii/S0012821X07004761.

J.-L. Zhou, S. J. Aarseth, D. N. C. Lin, and M. Nagasawa. Origin and Ubiquity of Short-Period Earth-like Planets: Evidence for the Sequential Accretion Theory of

Planet Formation. *The Astrophysical Journal*, 631(1):L85–L88, Sept. 2005. ISSN 0004-637X. doi: 10.1086/497094. URL https://doi.org/10.1086/497094.

W. Zhu and S. Dong. Exoplanet statistics and theoretical implications. *Annu. Rev. Astron. Astrophys.*, 59(1):291–336, Sept. 2021. ISSN 0066-4146. doi: 10.1146/annurev-astro-112420-020055. URL https://doi.org/10.1146/annurev-astro-112420-020055.

W. Zhu, C. Petrovich, Y. Wu, S. Dong, and J. Xie. About 30% of Sun-like Stars Have Kepler-like Planetary Systems: A Study of their Intrinsic Architecture. *The Astrophysical Journal*, 860(2):101, June 2018. ISSN 1538-4357. doi: 10.3847/1538-4357/aac6d5. URL http://arxiv.org/abs/1802.09526. arXiv:1802.09526 [astro-ph].

S. Zieba, M. Zilinskas, L. Kreidberg, T. G. Nguyen, Y. Miguel, N. B. Cowan, R. Pierrehumbert, L. Carone, L. Dang, M. Hammond, T. Louden, R. Lupu, L. Malavolta, and K. B. Stevenson. K2 and Spitzer phase curves of the rocky ultra-short-period planet K2-141 b hint at a tenuous rock vapor atmosphere. *arXiv:2203.00370 [astro-ph]*, Mar. 2022. URL http://arxiv.org/abs/2203.00370. arXiv: 2203.00370.